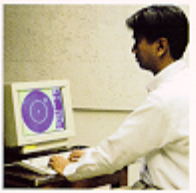

INDEPENDENT RESEARCH 1996 ANNUAL REPORT

Naval Command, Control and
Ocean Surveillance Center
RDT&E Division
San Diego, CA 92152–5001

NRaD

Technical Document 2933
October 1996

Independent Research 1996 Annual Report

Naval Command, Control and
Ocean Surveillance Center
RDT&E Division

San Diego, CA
92152–5001

CONTENTS

INTRODUCTION

INTRODUCTION

New and innovative ideas proposed by the scientists and engineers of the Naval Command, Control and Ocean Surveillance Center (NCCOSC) are supported and encouraged through the Independent Research (IR) program, which is sponsored by the Office of Naval Research (ONR). The IR program is implemented by NCCOSC's Research, Development, Test and Evaluation (RDT&E) Division (NRaD) under the direction of the Deputy Executive Director for Science, Technology, and Engineering. This program supports initial research in several areas of interest to the Navy, including command and control, communications, ocean surveillance, and navigation.

The FY 96 IR program was administered by Dr. Alan Gordon, Code D14. The program began with the March 1995 call for proposals in four IR Thrust Areas. The Thrust Areas were Command and Control, Communications, Surveillance, and Other Leadership Areas. Scientists and engineers responded with 68 proposals. The proposals were screened for scientific merit and Navy relevance, and assigned to the appropriate Thrust Area. Proposals were evaluated by panels of experts constituted for each of the Thrust Areas. The panels included Dr. Gordon, line management for the proposal principal investigator, NRaD technical experts, faculty members from local universities, and visiting professors on the ONR–ASEE (American Society for Engineering Education) Summer Faculty Research Program. Based on administrative and peer review, 31 projects were selected. Total funding of $2,763K was available for the FY 96 Independent Research Program.

This report contains tables that provide information on active and multisponsored projects and lists of publications and patents. Although the Independent Exploratory Development (IED) program was terminated at the end of FY 93, this report includes information on patents that resulted from the IED program after the FY 94 IR report. The bulk of this report contains short descriptions of FY 96 IR projects that highlight their objectives and accomplishments. In addition, three IR projects have been selected for more in-depth treatment.

For their exemplary results, the following three projects are featured in this report.

"Optical Fiber Devices Based on Index of Refraction Changes in Highly Overcoupled Fused-Fiber Couplers" by R. J. Orazi. The author describes an investigation directed to improving the ability to manufacture optical-fiber wavelength division multiplexers used in fiber-optic communication systems.

"Tidal Exchange at the Bay–Ocean Boundary" by D. B. Chadwick. Environmental impact assessment was investigated by a method that combined the use of shipboard acoustic Doppler current measurements with a unique bay–ocean tracer technique to provide visualization of pollutant exchange.

"Detection Algorithms Derived from Gaussian Mixture and Hidden Markov Noise Models with Applications to Radar and Sonar" by D. W. J. Stein. Ocean surveillance related phenomena were studied in a program that demonstrated that Gaussian mixture probability densities, and, more generally, hidden Markov models, may be used to model ocean acoustic noise dominated by a few moving sources, and to model radar back scatter from the sea surface.

	Independent Research					Independent Exploratory Development				
Fiscal Year	92	93	94	95	96	92	93	94	95	96
Funding ($K)	1,745	2,278	2,312	2,463	2,763	888	834	—	—	—
Number of projects	21	27	28	29	31	13	12	—	—	—
Professional work-years	13	15	14	15.3	15.6	7	7	—	—	—
Refereed journals, books, and dissertations (published/accepted)	21	26	13	26	19	1	2	—	—	—
Refereed journals, books, and dissertations (submitted)	N/A	N/A	10	9	9	N/A	N/A	—	—	—
NRaD publications	11	5	5	3	4	10	3	1	—	—
Presentations to professional meetings (invited)	23	12	6	27	12	7	—	—	—	—
Presentations to professional meetings (contributed)	16	54	19	33	26	8	6	—	—	—
Patents issued	5	4	7	5	6	8	6	3	2	—
Claims allowed, pending issue	—	—	2	2	—	3	4	—	—	3
Patent applications filed	11	14	6	6	11	10	7	5	4	2
Invention disclosures authorized	6	4	—	5	6	3	2	1	1	1
Invention disclosures submitted			7	7	7			1	—	—
Percent of completed projects transitioned	54	36	25	54	24	56	10	—	—	—

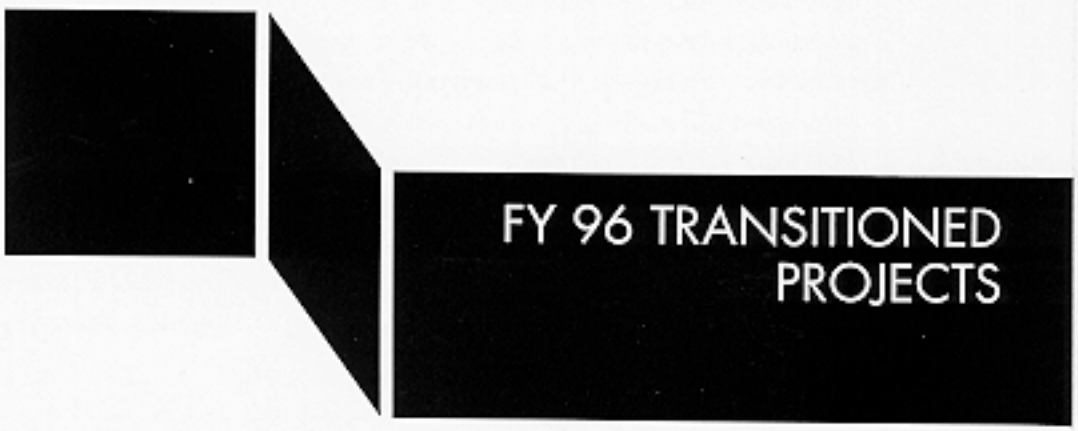
FY 96 TRANSITIONED
PROJECTS

FY 96 TRANSITIONED PROJECTS

Dynamics and Exchange Processes at the Bay–Ocean Boundary

This project investigated the importance of tidal pumping in controlling the exchange of water between bays and oceans. Exchange at the bay–ocean boundary was studied through observations at the mouth of San Diego Bay. Novel methods of observation were developed by combining the use of shipboard acoustic Doppler current measurements with a unique bay-water tracer technique to provide visualization of the exchange as well as exchange budgets. The work is important because the Navy needs to know how its activities impact the environment and must comply with federal, state, and local water-quality regulations. Work initiated under the IR project is continuing under the Naval Station San Diego Assessment Project with funding from Commander in Chief, U.S. Pacific Fleet (CINCPACFLEET). The program manager is Theresa Morley, (619) 556–6438.

Optical Fiber Devices Based on Index of Refraction Changes in Highly Overcoupled Fused-Fiber Couplers

The focus of this project was to understand the physical processes that affect the performance of optical-fiber wavelength division multiplexer (WDM) devices. WDMs are used to increase the data capacity of optical fibers by combining multiple signal channels based on different wavelengths of light. As a result of the investigation, an improved process for fine tuning the wavelength response of narrow-channel WDMs was developed and incorporated into an ongoing ONR-sponsored 6.2 program in Undersea Distributed Surveillance Technology. The ONR program included funding of $180K in FY 96 and $100K in FY 97 for WDM development. The program manager is Dr. Donald Davison, ONR 321, (703) 696–3160.

Environmentally Adaptive Radar Waveforms

The objective of this project was to model the physics of low-altitude radio frequency (RF) electromagnetic propagation and surface clutter in range-dependent littoral environments, and to develop waveforms and signal processing to allow for improved sensor and combat system performance via adaptation to synoptic conditions. Applications and further development of propagation environment modeling technology developed under the IR project are continuing under the following programs: (1) Navy Advanced Technology Demonstration (ATD), RF Mission Planner (RFMP) developed by the Naval Information Warfare Activity of the Naval Security Group, program manager Ernest Anastasi, (301) 617–3734; and (2) ATD Interactive Multi-Sensor Analysis Training (IMAT) system developed by the Naval Personnel Research and Development Center under ONR 6.2 sponsorship, Ms. S. Wetzel–Smith, (619) 553–7639, program manager.

Use of the “Laser pH Jump” to Initiate Ground-State Reaction for Robotics

This project investigated the use of laser-induced changes in pH to produce volume changes in a polymer for application as an “artificial muscle.” A potential Navy application is light-activated actuators deployed underwater and energized by fiber-optic cables. Civilian applications include robotic surgical devices. The IR project confirmed that molecules with adequately large response can be synthesized. The project is continuing in FY 97 under Defense Advanced Research Projects Agency (DARPA) sponsorship. The DARPA program manager is Steve Wax, (703) 696–2281.

SELECTED INDEPENDENT RESEARCH PROJECTS

Optical Fiber Devices Based on Index of Refraction Changes in Highly Overcoupled Fused-Fiber Couplers

Richard J. Orazi

This project modeled the effect of changing the index of refraction of the glass within the coupling region of a fused-fiber wavelength division multiplexer (WDM) that had been pulled through many coupling cycles. A simple expression describing the expected wavelength shift based on the number of power cycles observed during manufacture of the coupler was derived and found to be in good agreement with the shifts expected from fitting actual wavelength response curves for narrow-channel, fused-fiber WDMs. The wavelength responses of WDMs with channel spacings between 8 and 24 nm were altered by exposure to high-intensity ultraviolet light. Wavelength shifts were shown to be the result of changes in the effective index of refraction of the glass in the fused region of the couplers, with effective index of refraction changes in the illuminated area estimated to be between 10^{-3} and 10^{-2}.

INTRODUCTION

Wavelength division multiplexing, the process of placing multiple signals, each carried by a different wavelength of light, onto a single optical fiber, has proven to be an essential tool in the development of modern fiber-optic links. Wavelength division multiplexing may be used to greatly increase the bandwidth of an existing transmission system or to allow for wavelength-based routing in high-speed switching networks. Narrow-channel, fused-fiber wavelength division multiplexers (WDMs) have been shown to be useful components for such systems [1], and fused-fiber, polarization-independent, narrow- channel (PINC) wavelength division multiplexers (WDMs) have been developed that have excellent operating characteristics [2 and 3]. The fact that the fused-fiber manufacturing technique can be scaled to allow for high-volume production, and thus potentially low cost, bodes well for the use of these devices in WDM fiber links that use 2 to 4 wavelengths in either the 1.3- or 1.55-μm wavelength bands.

During the manufacturing process for these devices, randomly polarized light is input into one of two fibers that are fused together and tapered, and the output power of each fiber is monitored as the coupler is elongated. As the fused fibers are tapered, light begins to couple over from one fiber into the second fiber, and if the process is continued, the optical power is observed to cycle sinusoidally between the two output ports. In addition, form birefringence in the coupled region results in a sinusoidal envelope modulating this power transfer that appears when the coupler has been drawn to sufficient lengths. A PINC WDM is created when the output power is observed to be simultaneously at an extremum in the coupled power and a maximum in the polarization envelope. A typical plot of the output of one port of a fused-fiber coupler as it is being manufactured is shown in figure 1. In order to better understand the properties of these devices, it is useful to examine the dependence of the wavelength response of a narrow-channel, fused-fiber WDM upon the index of refraction of the coupling region.

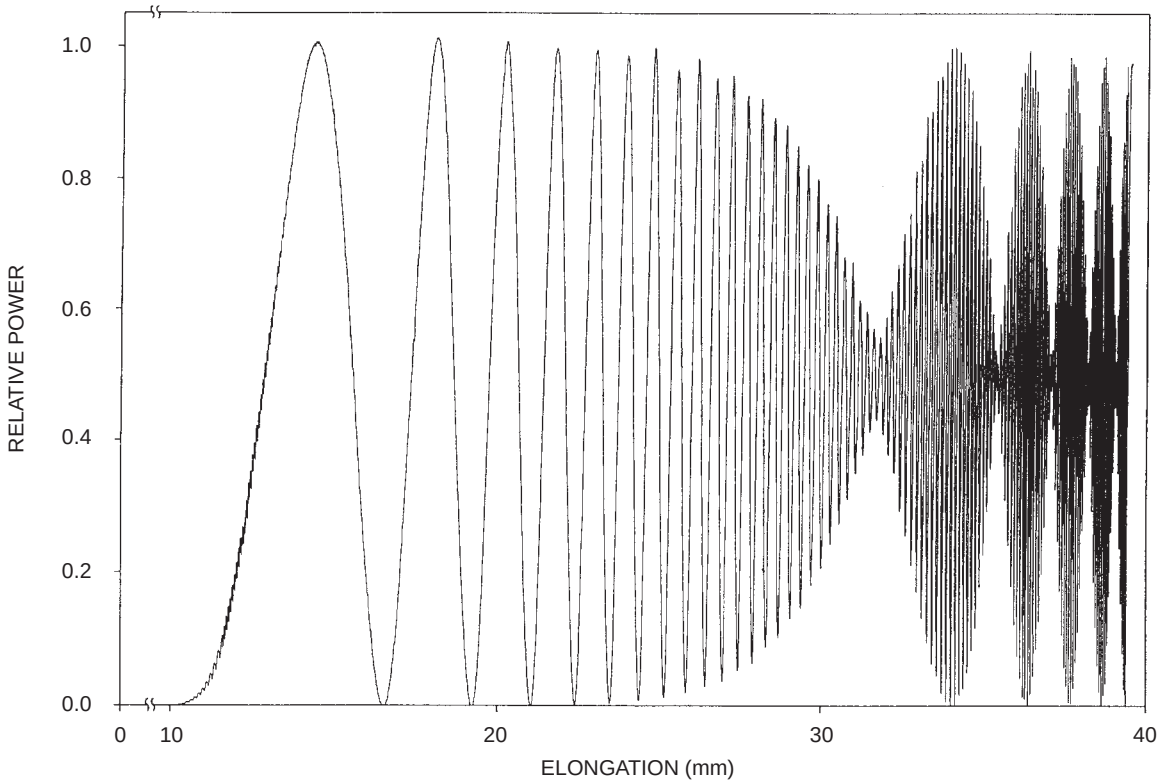

Figure 1. Coupled power as a function of pulled length in a fused-fiber coupler.

One of the factors behind the interest in studying the effects of altering the index of refraction in a fused-fiber WDM is the difficulty in establishing the degree of control in the fabrication process necessary to make such devices at specified wavelengths. As the device is being manufactured, the coupled power will begin to switch very rapidly between the two output fibers when the coupler is tapered to the longer lengths necessary to achieve narrow channel spacings. This can make it difficult to stop the tapering process at the precise moment when the coupler has achieved the desired wavelength response. In addition, the channel wavelengths of the WDM may undergo a slight shift during the packaging process due to additional stress that may be applied to the fused region during the bonding of the fused coupler to the necessary supporting substrate. For these reasons it would be useful to develop a process by which the wavelength response of such fused-fiber WDMs could be fine-tuned after the tapering and initial packaging steps have been completed. Such fine tuning has been demonstrated on bulk electro-optic devices by the application of high-intensity ultraviolet (UV) light to a section of the waveguide in order to trim the optical path length [4]. This report describes the changes in the wavelength properties of PINC WDMs in terms of the number of coupling cycles (N) and the number of maxima in the polarization envelope (M) that the coupler has undergone during its manufacture. This report also demonstrates that a UV trimming technique, similar to that described above, may be applied to the fine-tuning of fused-fiber devices. In addition, the prospect of creating temporary changes in the index of refraction of a PINC WDM to create a compact all-optical wavelength router is explored.

COUPLER ANALYSIS

Reference [5] analyzed the coupling properties of fused-fiber couplers in the presence of unpolarized or randomly polarized light, and showed the primary power coupling and the modulating envelope were due to terms involving the sum and difference of the coupling coefficients for the two orthogonal polarizations. If the fibers are well-fused, as is typically the case for couplers manufactured with our apparatus, it was shown that the coupler can be reasonably well-modeled by assuming a rectangular cross section for the coupling region. The coupled power wavelength response of such a device, to lowest order in λ/a, can be written as

$$P_c = \frac{1}{2} P_o \left\{ 1 - \cos\left(\alpha_+ \ \lambda\right) \cos\left(\alpha_- \ \lambda^2\right) \right\}, \tag{1}$$

where $\alpha_+ = 3\ \pi\ L/(16a^2\ n)$; $\alpha_- = 3\ L\ (n^2 - 1)^{1/2}/(32\ a^3\ n^3)$; a and 2a are the dimensions of the coupler cross section; L is the length of the coupling region; and n is the index of refraction of the glass (the coupler here is assumed to be surrounded by air).

To produce a WDM, where $\Delta\lambda_{WDM}$ is the wavelength difference between minima and maxima in the coupled power response curve, we find $\Delta\lambda_{WDM} = \pi/\alpha_+$, and this leads to an inverse relationship between the length L and $\Delta\lambda_{WDM}$. If a given WDM is produced with a minimum at a wavelength λ_1, it will have been pulled through N coupling cycles, such that $\alpha_+ \ \lambda_1 = 2\ N\ \pi$. Using this expression for the wavelength, one can examine the change in wavelength that will occur if the index is allowed to change. Doing this, and using the relationship between L and $\Delta\lambda_{WDM}$, one can derive the expression

$$\frac{\Delta\lambda_{S1}}{\Delta\lambda_{WDM}} = 2N\frac{\Delta n}{n}, \tag{2}$$

where $\Delta\lambda_{S1}$ is the shift in the location of the minimum in coupled power due to the index change Δn. Thus, the wavelength change, when viewed as a percentage of the overall WDM channel spacing, is equal to the percentage change in the index of refraction times twice the number of power transfer cycles the coupler has undergone.

A similar expression can be derived for the amount of shift in the location of the maximum of the polarization envelope, and the result is

$$\frac{\Delta\lambda_{S2}}{\Delta\lambda_{ENV}} = M\frac{\left[2n^2 - 3\right]\Delta n}{\left[n^2 - 1\right] n}, \tag{3}$$

where $\Delta\lambda_{S2}$ is the shift in the polarization envelope; $\Delta\lambda_{ENV}$ is the width of the envelope as represented by the distance from one maximum point to another; and M is the number of polarization envelope maxima that the coupler has been pulled through. Assuming the coupler has been manufactured so that the wavelengths of operation are simultaneously at an extremum in the coupled power and at a maximum in the polarization envelope, it can be shown that

$$\frac{\Delta\lambda_{ENV}}{\Delta\lambda_{WDM}} = \frac{\alpha_+}{2\lambda\alpha_-} = \frac{N}{M} . \quad (4)$$

Using equation (4), and choosing $n \approx 1.46$, equation (3) can be rewritten as

$$\frac{\Delta\lambda_{S2}}{\Delta\lambda_{WDM}} \approx 1.1\ N\ \frac{\Delta n}{n} . \quad (5)$$

Thus, the shift in the envelope is in the same direction as the WDM shift, but only about half as large.

It can be seen from equation (2) that to get a meaningful shift in the peak response of a fused coupler, index shifts on the order of 10^{-4} or greater are necessary. It has been demonstrated that the index of refraction of glass fibers is sensitive to UV light in the 240-nm wavelength region, with moderate shifts ($10^{-5} – 10^{-4}$) in the index believed to be the result of UV-induced defects associated with the core dopants [6], and larger index shifts ($10^{-3} – 10^{-2}$) resulting from structural changes in the glass core due to localized fusing as a result of very high intensity UV irradiation [7]. In fused-fiber couplers made with Ge-doped cores, it has been observed that the core dopant diffused outward into the cladding [8], and so for highly overcoupled devices, it is likely that Ge is present throughout the coupling region. Thus, narrow-channel fused-fiber couplers, with N values of 20 to 100 or greater, where the constituent glass fibers have undergone high-temperature processing, can be expected to exhibit a significant shift in their wavelength response when illuminated with high-intensity UV light near 240 nm.

EXPERIMENTAL RESULTS AND ANALYSIS

As a check on the expressions derived above, a PINC WDM was manufactured and temperature cycled to measure the shift in the wavelength peaks. For glass fibers, $dn/dT \sim 1.2 \times 10^{-5}/^oC$ [9], with the coefficient of thermal expansion being more than an order of magnitude smaller, so the primary cause for a shift in the wavelength response of the coupler will be due to the temperature dependence of the index of refraction. Figure 2 shows the measured temperature dependence of the location of one of the wavelength channels in a PINC WDM with an 8.5-nm channel spacing, which had N = 93.5 and M = 5. The curve is believed to deviate from linearity at higher temperatures due to packaging effects. Fitting a line to the linear portion, a slope of $d\lambda/dT \sim 1.3 \times 10^{-2} nm/^oC$ is found. To compare this to theory, it is necessary to take the derivative of equation (2) with respect to temperature. Doing this, and using known values of N, $\Delta\lambda_{WDM}$, n, and dn/dT, the result $d\lambda/dT = 1.3 \times 10^{-2} nm/^oC$ is obtained, which agrees with the experimental data.

To further check on the self-consistency of the derived equations when applied to actual WDM couplers, a pair of PINC WDMs, with nominal channel spacings of 22 nm and 8 nm, was manufactured and the wavelength response was measured. The data were then fit to equation (1) using a least squares fit with the parameters a and L; and α_+ and α_- were calculated from these fitted parameters. The wavelength response and fitted data for the 22-nm coupler is shown in figure 3. Table 1 lists the relevant data for each coupler. In these results, $\Delta\lambda_{WDN}$ and $\Delta\lambda_{ENV}$ were calculated from the values obtained for α_+ and α_-. Equation (4) is indeed verified by the data, with discrepancies only on the

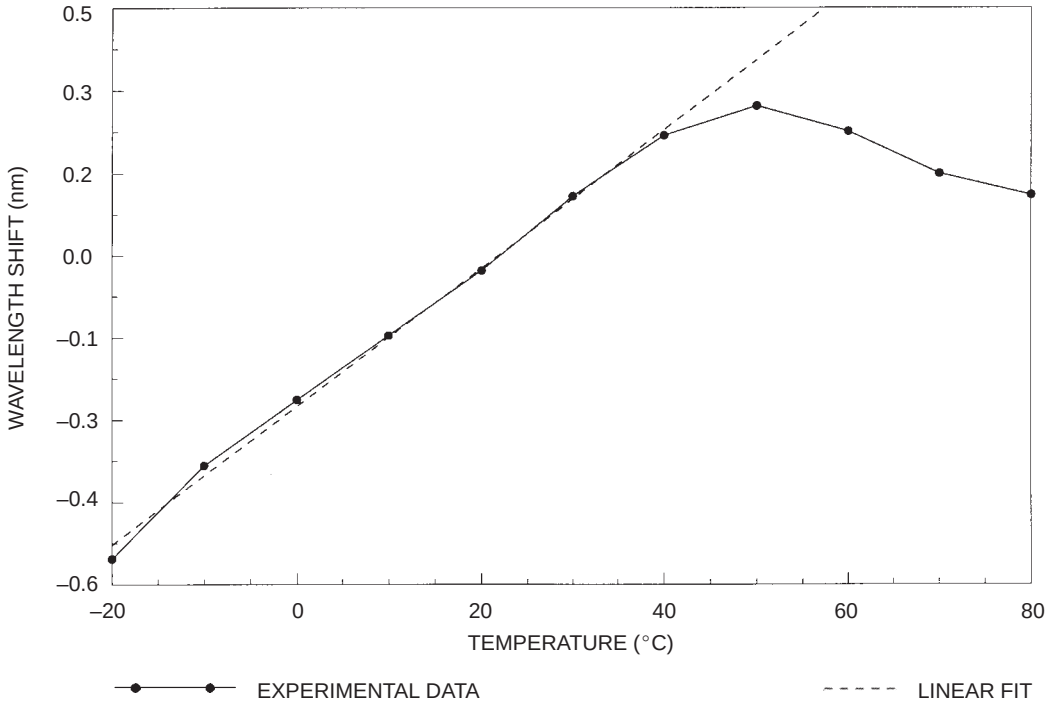

Figure 2. Temperature dependence of the peak channel wavelength of an 8.5-nm PINC WDM.

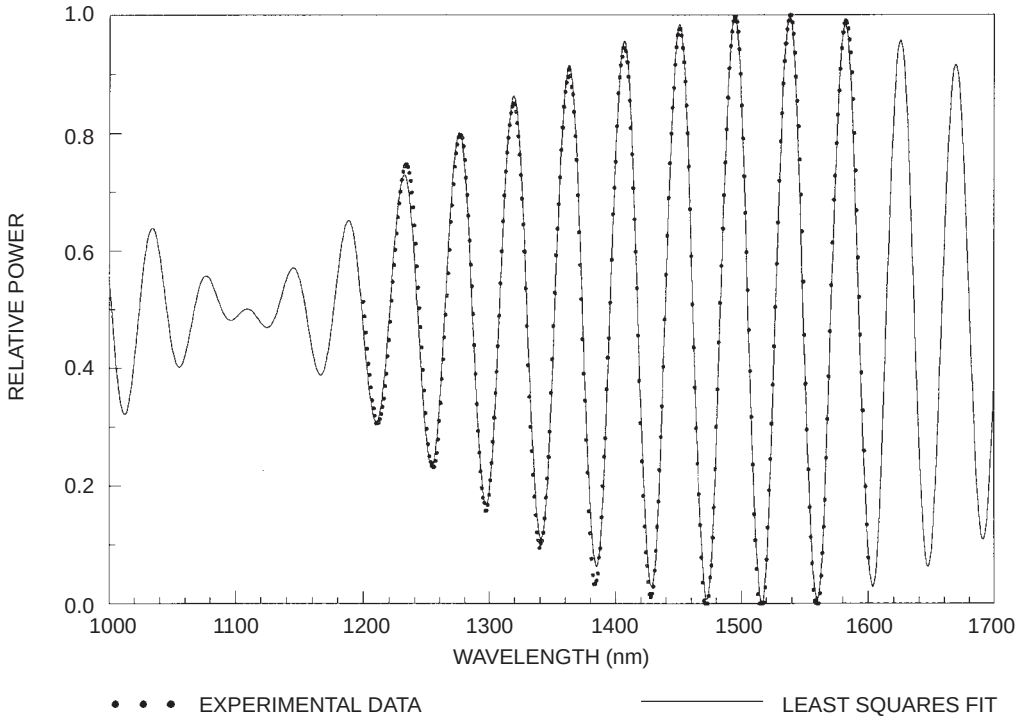

Figure 3. Wavelength response curves for PINC WDM coupler: 22-nm channel spacing.

Table 1. Observed and calculated parameters for two PINC WDMs.

Coupler	N	M	N/M	α_+ (nm^{-1})	α_- (nm^{-2})	$\Delta\lambda_{WDM}$ (nm)	$\Delta\lambda_{ENV}$ (nm)	$\Delta\lambda_{ENV}/\Delta\lambda_{WDM}$
1	36	1	36	1.4296×10^{-1}	1.3574×10^{-6}	21.98	742.8	33.8
2	101.5	5	20.3	3.7491×10^{-1}	5.1250×10^{-6}	8.38	196.7	23.5

order of 10%. To check on the validity of the other derived expressions, the wavelength shifts and index changes calculated using these results can be compared to those expected if the parameters of the fitted data, using equation (1) as the functional form for the coupled power, were changed by a corresponding amount. Table 2 gives a comparison of the wavelength shifts obtained by various methods for the two couplers studied. As a basis for comparison, a wavelength shift equal to 1/2 the WDM channel spacing was assumed. The equation used to calculate each value is given in parentheses. If no equation number is listed, the value was calculated using the fitted data and the functional dependence given by equation (1). The shifts $\Delta\lambda_{S2}$ were determined using the values for $\Delta n/n$ calculated from the fitted data. Table 2 shows relatively good agreement between the various methods of calculating index and wavelength shifts.

Table 2. Comparisons of expected wavelength shifts and index changes derived by various methods.

Coupler	$\Delta\lambda_{S1}/\Delta\lambda_{WDM}$	$\Delta n/n$	$\Delta n/n$ (2)	$\Delta\lambda_{S2}$	$\Delta\lambda_{S2}$ (3)	$\Delta\lambda_{S2}$ (5)
1	0.5	7.05×10^{-3}	6.94×10^{-3}	6.25 nm	5.96 nm	6.35 nm
2	0.5	2.69×10^{-3}	2.46×10^{-3}	2.38 nm	3.01 nm	2.61 nm

To investigate the possibility of using UV light to alter the wavelength response of fused-fiber WDMs, a series of PINC WDM couplers was manufactured and pre-packaged, with the fibers attached to a fused silica substrate, but not enclosed in the standard protective housing. Experiments were conducted using an excimer laser operating at 248 nm with a KrF gain medium and a pulse width of 23 ns. Pulse repetition rates of 1 or 2 Hz were used with pulse energies up to 600 mJ. The laser intensity profile was homogenized, shaped, and directed normal to the coupler surface, with UV beam dimensions of 1.2 cm $\times$ 0.24 cm. Fluence was controlled using variations in pulse energy and dielectrically coated beam-splitting attenuators. WDMs were manufactured from Corning dispersion-shifted fiber, with nominal channel spacings of 24 nm ($N \sim 36$), 15 nm ($N \sim 55$), and 8 nm ($N \sim 100$). Couplers of each type were then submitted to UV processing at various energy fluences. The wavelength response of the couplers was measured on an optical spectrum analyzer both before and after UV illumination. During processing, light from a tunable 1550-nm laser source was input to the couplers, and the signal from both output ports was measured. The wavelength was initially set to the 50% coupling point to provide maximum sensitivity to any wavelength shift. The shift was measured by observing the change in the coupling ratio of the device as a function of the number of UV pulses. The measured wavelength response curves were used to calculate the wavelength shift. UV illumination was generally continued until the resultant index change was observed to saturate.

Energy fluences used in these experiments were limited by available beam splitters; measurements were made at fluences of 242 mJ/cm^2, 570 mJ/cm^2, and 1340 mJ/cm^2. No wavelength shifts were observed for fluences of 13 mJ/cm^2 or below. As a general rule, it was observed that UV processing

did not significantly change the insertion loss of the devices. However, at the highest fluence levels measured, several couplers broke, and others experienced an increase in excess loss up to 0.8 dB. This additional loss was observed to decrease if illumination was continued beyond the saturation point. After UV processing, the near-end crosstalk of six couplers was measured. On five of these, the backreflection was measured to be <–66 dB down, limited by our measurement system. The sixth was measured to be –54 dB down, which is still within typical fused-coupler specifications.

The curves in figure 4 are representative of the wavelength shifts observed after UV processing of PINC WDM couplers. The channel wavelengths of this 15-nm WDM were observed to shift by approximately 1.9 nm after 400 pulses of UV light at a fluence of 242 mJ/cm^2. The change in peak isolation observed is not a result of any degradation as a result of the UV illumination, but is due to the presence of the polarization envelope that modulates the wavelength response of relatively long fused-fiber devices (and thus ultimately determines the peak isolation), and the fact that this modulation envelope undergoes a shift that is different from the shift of the fundamental wavelength response curve, as seen in equation (5).

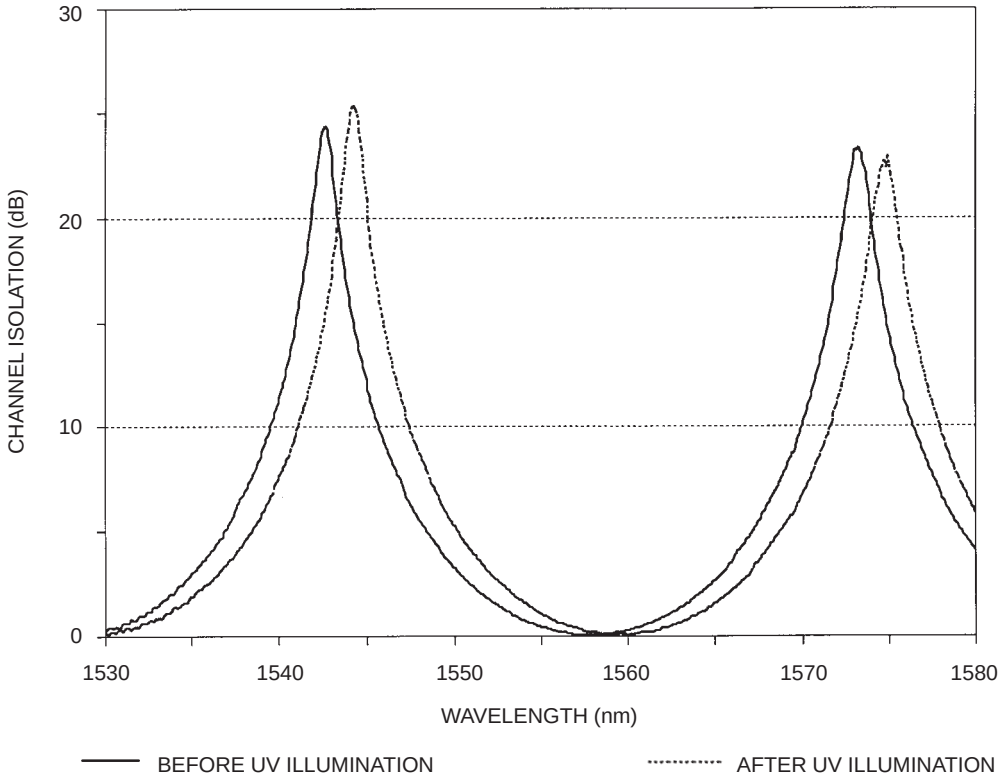

Figure 4. Wavelength response of one arm of a PINC WDM with 15-nm channel separation.

Figures 5 and 6 show the results of the UV illumination experiments; the relative index shifts ($\Delta n/n$) indicated were calculated from the observed wavelength shifts using equation (2) and assuming that 1/2 of the coupling region was illuminated by the UV beam. Figure 5 highlights the different shifts obtained when illuminating 15-nm channel spacing WDMs with various energy fluences. As

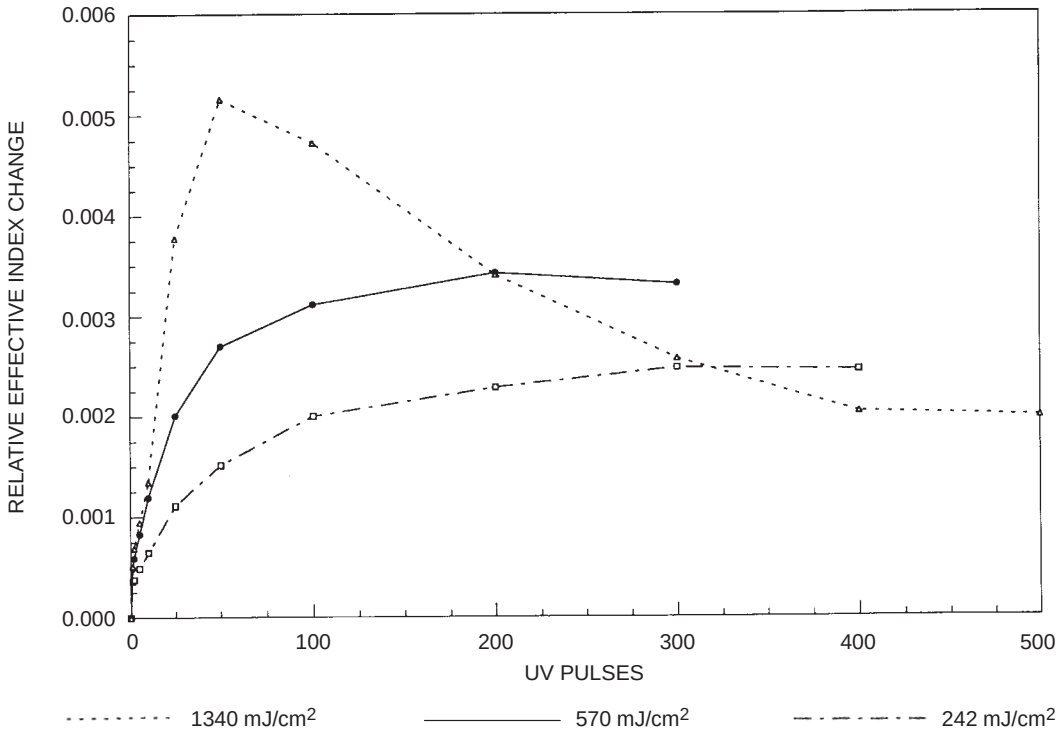

Figure 5. Effective index change vs. UV pulses for various pulse energies: 55-cycle couplers.

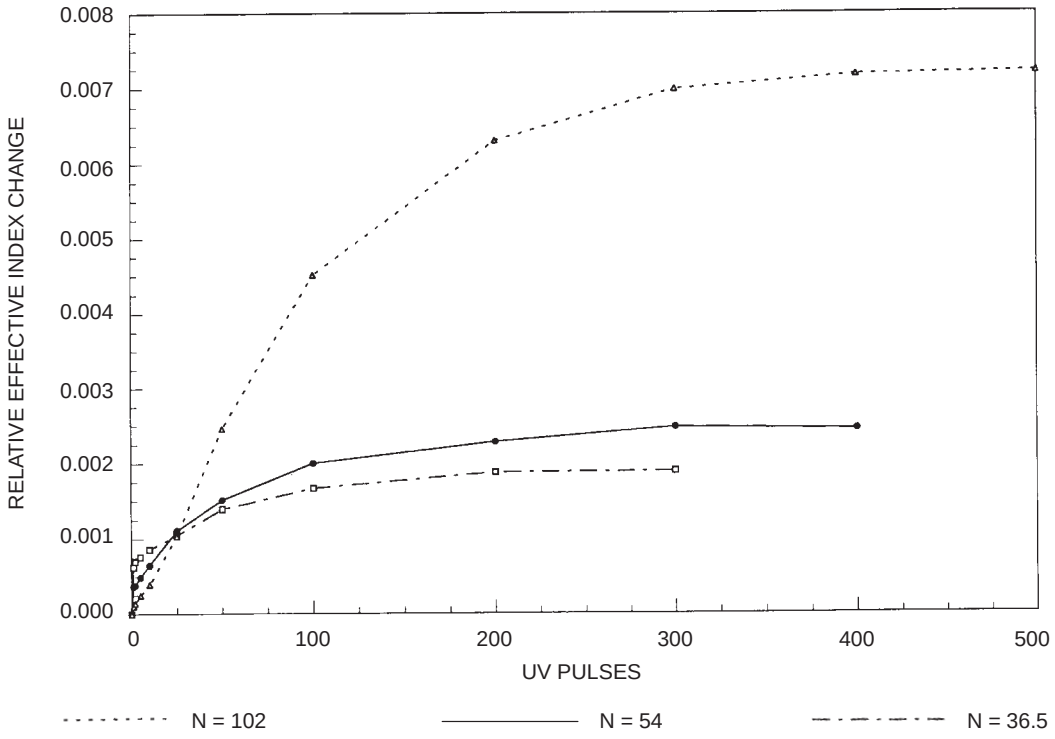

Figure 6. Effective index change vs. UV pulses for couplers with various coupled power cycles N: UV fluence of 242 mJ/cm^2.

expected, higher fluences lead to larger shifts, although saturation is reached more quickly. The top trace in figure 5 indicates that the damage causing the index shift eventually begins to be annealed by overexposure to the UV beam, reversing the index change. Figure 6 shows a similar set of curves, this time with a constant fluence of 242 mJ/cm^2, for the three varieties of WDMs studied. The difference in effective index shifts is believed to be due to the difference in the diameter of the coupling region for the three types of couplers. In [7] it was observed that the damage causing the index shift was localized to the side of the core facing the UV beam. This was due to the high UV absorption in the Ge-containing region. Thus, the UV beam may not penetrate through the entire fused region of the coupler, and those couplers with smaller diameters will have a larger percentage of the coupling region exposed, resulting in a higher effective index change.

OPTICAL SWITCHING IN PINC WDMS

The UV processing discussed above leads to permanent changes in the wavelength response of the fused-fiber WDMs. In theory, if one could find a way to create a temporary change in the index of refraction of the coupling region in a narrow-channel WDM, it would be possible to create an all-fiber switch or wavelength router from these devices. To create such a switch, one would want $\Delta\lambda_{S1}/\Delta\lambda_{WDM}$ to be 1. If WDMs are made that have been pulled through a fairly large number of coupling cycles (N), then equation (2) indicates that switching could occur with a modest change in the index of refraction.

The method investigated here for creating a temporary change in the index of refraction in the coupling region of a fused-fiber WDM involves the use of an active fiber that has been doped with the rare-earth element erbium. Such fibers have been shown to exhibit gain in the 1550-nm region when optically pumped with the appropriate wavelength of light, and have found widespread use as the basis for all-fiber amplifiers and laser sources. Light in the 1550-nm wavelength region traveling in a section of fiber doped with erbium will initially experience a loss since it is absorbed by the erbium. However, once the pump light is turned on, the absorption of the doped fiber will decrease. This change in absorption will result in a change in the index of refraction of the glass fibers, as specified in the Kramers–Kronig relations. Figure 7 shows how this property could be used to create an all-optical wavelength router. The speed of such a switch is limited by the excited state lifetime of the erbium dopant, which is about 10 ms. However, should such a switch prove feasible using erbium, other rare earth dopants with absorption near the intended signal wavelengths, and having much shorter exited state lifetimes, could be investigated.

To investigate the feasibility of these fiber switches, a 1-inch length of 300-ppm erbium-doped fiber was fusion-spliced between two sections of standard dispersion-shifted optical fiber. Although the difference in core dimensions for these two types of fiber is fairly large, a combined splice loss of less than 0.5 dB could be achieved. A pair of these spliced fibers was then used to create a narrow-channel, fused-fiber WDM. Low (<0.2 dB) excess loss PINC WDMs, with channel spacing of 15 nm (N = 55) could be fabricated with this fiber. However, when optically pumped with 980-nm light, no change in the wavelength response of the WDM was observed. This was attributed to the relatively low starting erbium concentration, and the fact that diffusion of the erbium out of the core and into the cladding glass may have lowered the final concentration by as much as two orders of magnitude. To better determine the possibility of obtaining optical switching in such a device, the highest doped

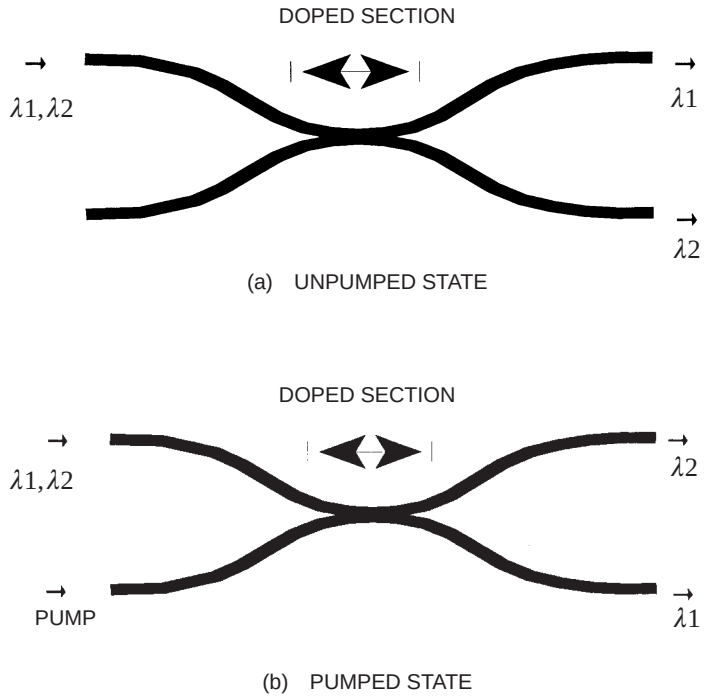

Figure 7. All-optical wavelength router/switch ($\Delta\lambda = \Delta_{WDM}$).

commercially available erbium fiber (~4800 ppm) was obtained, and the change in absorption between the pumped (totally bleached) and unpumped states was measured for a short section of this fiber. The result is shown in figure 8, indicating a peak absorption change of about 0.12 cm^{-1}. A Kramers–Kronig analysis of this data leads to an expected peak index change of about 10^{-6}. Although a cladding-doped erbium fiber could be fabricated to eliminate the erbium diffusion problem, the maximum erbium concentration can be increased by less than a factor of 100, giving a maximum theoretical peak index change of less than 10^{-4}. Equation (2) shows that such a device would need to be pulled through a total of $N \sim 5000$ coupling cycles in order to exhibit switching, which is too large a number for the reliable production of PINC WDMs. In addition, if such a device could be fabricated, it would prove to have a high environmental sensitivity, since less than a 10°C temperature change would lead to a Δn large enough to cause switching in the device.

CONCLUSIONS

Equations relating the shift in the wavelength response, due to changing the index of refraction in a highly fused narrow-channel, fused-fiber WDM, to the number of power cycles the coupler has been pulled through have been derived. It has been shown that the polarization envelope observed in the wavelength response curves of such couplers will exhibit a wavelength shift roughly half as large as the shift in the WDM channel location. The derived channel wavelength shift is found to be in excellent agreement with experimental data based on the known temperature dependence of the index of refraction of silica glass fibers. These relations indicate the possibility of adjusting the location of the WDM wavelength channels by creating permanent changes in the index of refraction in the coupling

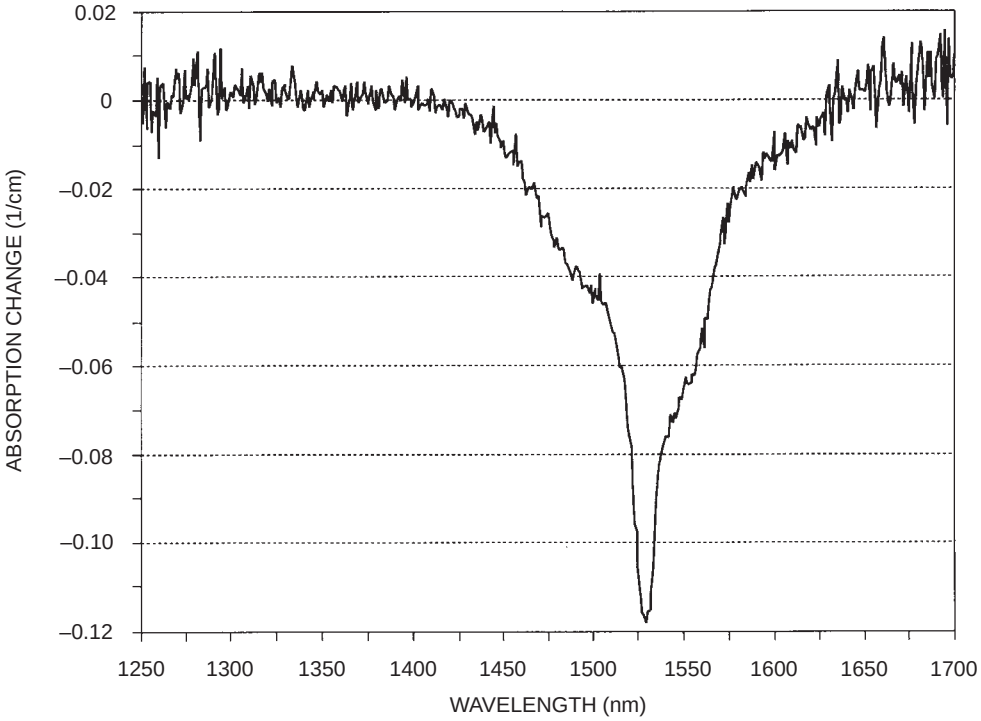

Figure 8. Absorption change vs. wavelength for a highly doped erbium filter.

region of the device. Fine tuning of fused-fiber devices capable of multiplexing multiple wavelengths in the 1550-nm band has also been demonstrated. By illuminating the central region of the coupler- with pulsed 248-nm light, shifts as high as 75% of the channel spacing, with no significant increase in the excess loss or backreflection, have been observed. After the initial pulse, a tuning resolution of less than 0.05 nm has been demonstrated. This technique has proved to be a useful method for adjusting the peak channels of narrow-channel fused-fiber devices before the final packaging step, which should allow higher yields and thus lower manufacturing costs for these devices. Finally, one potential method of creating an all-optical switch has been examined, involving absorption changes in erbium-doped fibers, which lead to index of refraction changes in the fibers. It has been determined that the index changes that can be expected are too small to produce a practical device.

REFERENCES

1. Orazi, R. J. and M. N. McLandrich. 1994. “Bidirectional Transmission at 1.55 Microns Using Fused Fiber Narrow Channel Wavelength Division Multiplexors and Erbium-Doped Fiber Amplifiers,” *IEEE Photonics Technology Letters*, vol. 6, no. 4, pp. 571–574.

2. McLandrich, M. N., R. J. Orazi, and H. R. Marlin. 1991. “Polarization Independent Narrow Channel Wavelength Division Multiplexors for 1.55 Microns,” *Journal of Lightware Technology*, vol. 9, no. 4, pp. 442–447.

3. Orazi, R. J., T. T. Vu, M. N. McLandrich, C. A. Hewett, and P. M. Poirier. 1996. “Cascaded Narrow Channel Fused-Fiber Wavelength Division Multiplexors,” *Electronics Letters*, vol. 32, no. 4, pp. 368–370.

4. Kashyap, R., G. D. Maxwell, and B. J. Ainslie. 1993. “Laser-Trimmed Four-Port Bandpass Filter Fabricated in Single-Mode Photosensitive Ge-Doped Planar Waveguide,” *IEEE Photonics Technology Letters*, vol. 5, no. 2, pp. 191–194.

5. Payne, F. P., C. D. Hussey, and M. S. Yataki. 1985. “Polarization Analysis of Strongly Fused and Weakly Fused Tapered Couplers,” *Electronics Letters*, vol. 21, pp. 561–563.

6. Dong, L., J. L. Archambault, L. Reekie, P. St. J. Russell, and D. N. Payne. 1995. “Photoinduced Absorption Change in Germanosilicate Preforms: Evidence for the Color-Center Model of Photosensitivity,” *Applied Optics*, vol. 34, no. 18, pp. 3436–3440.

7. Archambault, J. L., L. Reekie, and P. St. J. Russell. 1993. “100% Reflectivity Bragg Reflectors Produced in Optical Fibres by Single Excimer Laser Pulses,” *Electronics Letters*, vol. 29, no. 5, pp. 453–455.

8. McLandrich, M. N. 1988. “Core Dopant Profiles in Weakly Fused Single-Mode Fibres,” *Electronics Letters*, vol. 24, no. 1, pp. 8–10.

9. Carr, J. J., S. L. Saikkonen, and D. H. Williams. 1990. “Refractive Index Measurements on Single-Mode Fiber as Functions of Product Parameters, Tensile Stress, and Temperature,” *Fiber and Integrated Optics*, vol. 9, pp. 393–396.

Tidal Exchange at the Bay–Ocean Boundary

D. Bart Chadwick and John L. Largier

The Navy must provide an uncompromised level of defense capability without undue stress on the shoreline and marine environment. This issue is especially acute in coastal estuaries and embayments such as San Diego Bay where the impact of large numbers of Navy ships, submarines, support craft, and shoreside facilities must be balanced against a background of ecological, recreational, and aesthetic conservation. Since zero discharge is not technically possible, the question arises, at what level can wastes be assimilated by the coastal ocean, and from a scientific perspective, what are the fundamental processes that determine the fate of these substances? An important step toward the answer is to understand the mechanisms, interactions, and scales of motion that control circulation and mixing in bays and estuaries. For bays and inlets with narrow entrances, the tidal exchange to the ocean is often characterized by an ebb–flood asymmetry in which the ebb flow is ejected from the bay as a jet, while the return flow during the flood is drawn in approximately as a radial sink, a process often termed "tidal pumping." In this study, the importance of tidal pumping in controlling the exchange of water at the bay–ocean boundary was examined based on observations at the mouth of San Diego Bay. The observations are novel in combining the use of shipboard acoustic Doppler current measurements with a unique bay-water tracer technique to provide visualization of the exchange as well as exchange budgets. Visualization of the tidal evolution of flow and tracers suggests that, in accordance with the classical tidal pumping model, the horizontal dynamics at the mouth of San Diego Bay are governed by an asymmetry between the jet-like nature of the ebb–flow, and the sink-like nature of the flood flow. A one-dimensional trajectory model based on the observations indicates that the combined influence of the residual circulation and the offshore gradients in the amplitude and phase gradients of the velocity provide the mechanism by which water from the bay is preferentially ejected to the ocean. This pumping of the offshore flow is shown to produce a strong correlation between the sectional-average velocity and bay-water concentration, explaining the significant net tidal exchange between the bay and ocean.

INTRODUCTION

The exchange at the boundary between a bay and the ocean serves to regulate the flushing of contaminants and exerts significant control over the residence time, salt, and heat balance of the bay as a whole. In addition, spatial and temporal variations in bay–ocean flow may also provide favorable mechanisms for the transport of aquatic larvae. For bays and inlets with narrow entrances, the importance of this boundary in controlling conditions within a bay, and several of the key aspects of the exchange process were first suggested by Stommel and Farmer (1952). They pointed out that the tidal exchange between a bay and the ocean is often characterized by an ebb–flood asymmetry in which the ebb flow is ejected from the bay as a jet, while the return flow during the flood is drawn in approximately as a radial sink, a process often termed "tidal pumping" (Fischer et al., 1979). Stommel and Farmer proposed, for instance, that the overall salt balance within an inlet might be controlled by this mechanism, since the exchange volume on a given tide would be limited to the region of overlap between the jet and the sink (figure 1).

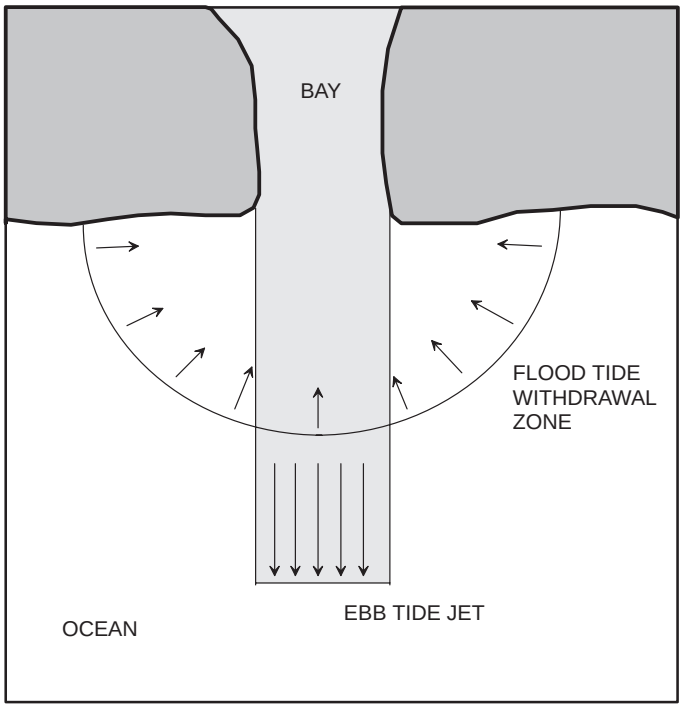

Figure 1. The tidal pumping model of Stommel and Farmer (1952), with the ebb flow as a rectangular jet, the flood flow as a semi-circular sink, and the exchange determined by the overlap of the jet and sink.

In this study, we evaluate the importance of this bay–ocean exchange mechanism based on field observations of the exchange between San Diego Bay and the Pacific Ocean during the period 1993–1996. It is shown that, in accordance with the classical tidal pumping model, the horizontal dynamics at the mouth of San Diego Bay are governed by an asymmetry between the jet-like nature of the ebb–flow, and the sink-like nature of the flood flow. This asymmetry is shown to result in a strong M2 amplitude gradient similar to that modeled by Awaji et al. (1980). Observations also support the presence of a significant phase lag in the offshore flow resulting primarily from the time required for development and decay of the ebb jet. A one-dimensional trajectory model based on the observed gradients is used to illustrate the mechanism by which particles from the bay are ejected to the ocean. This pumping of the offshore flow is shown to produce a strong correlation between the sectional-average velocity and bay-water concentration, explaining the significant net tidal exchange between the bay and ocean.

BACKGROUND

The distinct inlet dynamics of the ebb and flood tide flow fields have received considerable attention in previous theoretical studies. For the case of the outflow jet, most of this work has built on the relatively well-developed theory of steady, turbulent, plane jets (e.g., Tennekes and Lumley, 1972; Joshi, 1982; Metha and Joshi, 1988). In this case, the width of the jet can be expected to grow linearly with distance offshore (x), while the velocity decays in proportion to $x^{-1/2}$. Using a laboratory pumping system to alternately fill and drain a channel connected to a large adjoining basin, Wilkenson (1978) found that the structure of the outflow into the basin, when normalized to a periodic

length scale, collapsed to a family of profiles that grew through the tidal cycle but were independent of the entrance conditions, as long as the aspect ratio (width:periodic length) was small. Following Wilkenson, and using the velocity scale estimated from the tidal prism, the periodic length scale of the outflow jet may be determined based on the momentum flux $m_o = u_o^2 b_o$ as

$$l_{jet} \approx \left[4\pi^2 \left(\frac{A_b}{A_m} \right)^2 \eta_o{}^2 b_o \right]^{1/3} , \tag{1}$$

where η_o is the tidal amplitude, A_m is the cross-sectional area of the mouth, A_b is the surface area of the bay, and b_o is the entrance width.

In contrast, inflow studies suggest that the return flow more closely resembles an irrational potential sink, as long as the bottom slope is gentle (Ozsoy, 1977; Wilkenson, 1978). In this case, water is drawn uniformly from the offshore region, and the potential lines are semicircular arcs with the velocity decreasing away from the mouth in proportion to x^{-1}. Friction, bottom slope, and longshore flow may also influence the form of the withdrawal zone for the sink flow. For example, Wolanski and Imberger (1987) showed that the combined effects of a deepening shelf and a longshore flow result in the selective withdrawal of water from the region offshore and up-current of the entrance. For many tidal bays, the scale of the withdrawal zone may be estimated by assuming a standing wave tide within the bay. The volume of the offshore withdrawal zone is then dictated by the volume of the tidal prism $V_p = \eta_o A_b$. The radial scale of the withdrawal zone is thus given by

$$r_{sink} = \sqrt{\frac{2\eta_o A_b}{\pi h f}} , \tag{2}$$

where h is the average water depth of the withdrawal zone, and f is the fraction of a complete circular sink occupied by the withdrawal zone.

We expect then that tidal pumping should be effective when the periodic length scale of the jet significantly exceeds the radial scale of the withdrawal zone. Combining equations 1 and 2, defining the tidal excursion $l_x \sim \eta_o A_b/A_m$, and assuming $b_o h \sim A_m$, the ratio of these two scales is given by

$$\frac{l_{jet}}{l_{sink}} = \left(2\pi^5 f^3 \left(\frac{A_b}{A_m} \right) \left(\frac{\eta_o}{b_o} \right) \right)^{1/6} = \left(2\pi^5 f^3 \left(\frac{l_x}{b_o} \right) \right)^{1/6} . \tag{3}$$

From this we see that a simple criterion for tidal pumping is the requirement that the tidal excursion at the mouth significantly exceed the width of the mouth.

THE STUDY SITE

San Diego Bay is relatively long and narrow, 25 km in length and 1 to 3 km wide, forming a crescent shape between the City of San Diego on the north, and Coronado Island/Silver Strand on the south (figure 2). The bay is separated into two distinct topographic regions: the outer bay, which is generally narrow and deep, and the inner bay, which is wide and shallow. Exchange with the ocean is limited to a single channel at the mouth. This north–south channel is about 1.2 km wide, bounded by Point Loma on the west and Zuniga Jetty on the east, with depths between 5 to 15 m.

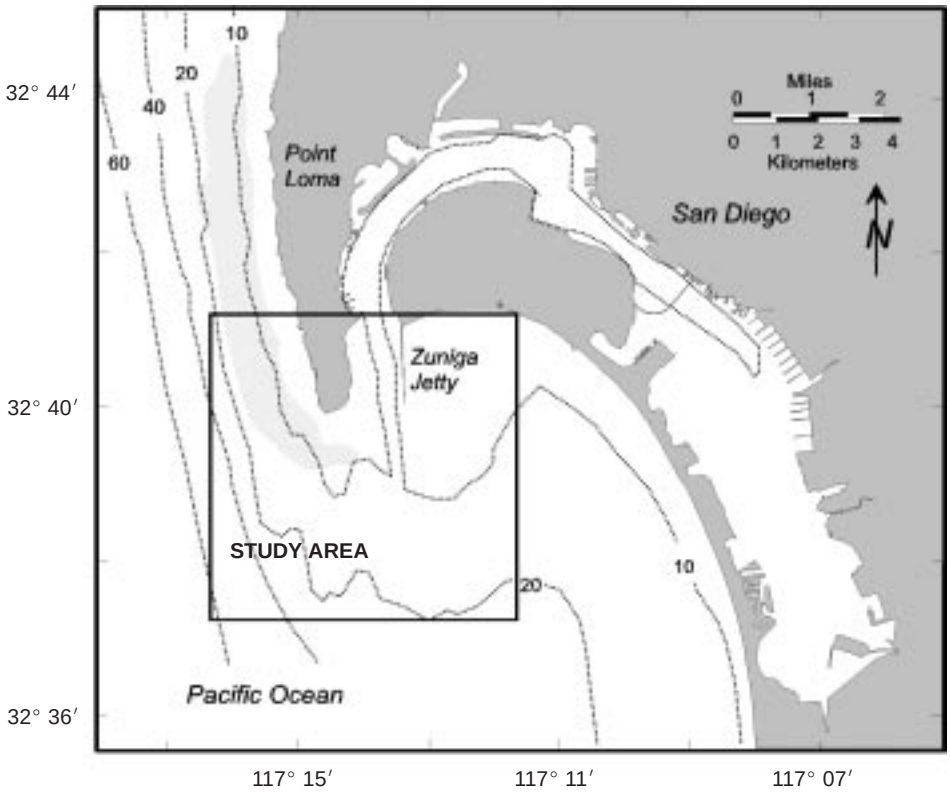

Figure 2. Map of San Diego Bay showing study area near the mouth. Dotted lines indicate bottom contours in meters, and the light shaded area indicates approximate location of kelp canopy.

Tides and currents within the bay are dominated by a mixed diurnal–semidiurnal tidal forcing, with a dominant semidiurnal component (Peeling, 1974). The tidal range from mean lower low water (MLLW) to mean higher high water (MHHW) is about 1.7 m with extreme tidal ranges close to 3 m. Tidal phase within the bay suggests the tides behave approximately as a standing wave with typical phase lags between the inner and outer bay of about 10 minutes and a slight increase in tidal amplitude in the inner bay compared to the outer bay (Cheng et al., in prep). The overall tidal prism for the bay is about $5.5 \cdot 10^7$ m^3 and decreases monotonically from the mouth toward the head of the bay. Correspondingly, the tidal excursion is largest near the mouth with a typical value of about 4.3 km. Comparing the tidal excursion to the width of the bay, we find that near the mouth $l_x/b_o \sim 4$, suggesting that tidal pumping at the mouth should be significant with $l_{jet}/l_{sink} \sim 3.2$.

THE FIELD PROGRAM

The field program consisted of a variety of measurement techniques aimed at resolving the circulation, transport, and exchange in the mouth region. Three spatial techniques were employed over semidiurnal tides including horizontal mapping, axial sections, and cross sections. In addition, longer term temporal data were collected from moored instruments along the axis of the outflow. Results presented here will focus on the mapping and cross-sectional surveys. All surveys were carried out aboard the Navy environmental survey boat, RV ECOS. During each survey, currents were measured using an RD Instruments 1.2 MHz, narrow-band, acoustic Doppler current profiler (ADCP) mounted downward looking in a transducer well aboard the RV ECOS. Positions during the surveys were determined using a differential-mode Global Positioning System (DGPS) system with precision of about 2 to 5 m (Trimble 4000–RL2). Hydrographic and contaminant data were obtained from an integrated suite of conductivity, temperature, and depth (CTD) and water quality sensors including temperature, salinity, pH, dissolved oxygen, ultraviolet fluorescence (UVF) and chlorophyll–a (Chl–a) (Chadwick et al., 1991). The CTD sensors were “tow-yoed” during the cross-sectional surveys, and run in flow-through mode during the mapping (due to problems with kelp fouling). The fluorometers were always run in flow-through mode. The water intake during the mapping was drawn from the hull at a depth of about 1 m. Water pumped from the towed CTD or hull was passed through a bubble trap and into the UVF and Chl-a fluorometers. The UVF measurements have been shown to provide a sensitive bulk estimate of total polycyclic aromatic hydrocarbons (TPAH) in water, a contaminant often associated with fuel spills, runoff, and creosote pilings (Katz and Chadwick, 1991; Katz et al., 1995). The UVF fluorometer used in these studies was identical to that used in Katz and Chadwick (1991) and is described in detail in that paper.

Mapping survey results presented here were collected during the full semidiurnal tidal period on September 9, 1995 (95MAP). Each survey consisted of a series of transects that criss-crossed the exchange region as shown in figure 3. The transects were generally repeated as often as possible, usually requiring 1 to 2 hours to complete each cycle. The tidal range for 95MAP was 1.7 m. To develop the maps of surface circulation, the velocity data were first vertically averaged over the upper 4 m, and then spatially averaged onto a uniform transect at 50-m intervals using a nearest neighbor technique. The UVF concentrations measured at 1-m depth were averaged onto the same spatial transect as the velocity data. A set of eight maps was then produced for velocity and UVF, corresponding to the transects performed during 95MAP. Cross-sectional survey results presented here will focus on the measurements collected at the mouth during 1995 (95MOUTH–2). During the survey, a transect across the mouth of the bay was repeated at 15- to 30-minute intervals throughout an ~12.4 hour, semidiurnal, symmetrical tidal cycle. The CTD/UVF system was profiled while underway to obtain a continuous series of 12 profiles across the mouth for each transect. The location of the transect and tow-yo profiles for the mouth cross-sections are shown in figure 3. To produce the final cross-sectional data plots, velocity, temperature, and UVF data were interpolated spatially onto a 10-m horizontal by 0.25-m vertical grid using a standard two-dimensional (2-D) Kreiging routine (Olea, 1974).

HORIZONTAL STRUCTURE OF THE BAY–OCEAN EXCHANGE

From survey 95MAP, a tidal sequence of maps was constructed for flow and fluorescence. The survey period represents a period of strong tidal forcing and thus stratification can be considered to be negligible in relation to the evolution of the exchange. The horizontal mapping data provide insight into the differences in the ebb and flood flow and tracer fields that regulate the exchange between the bay and the ocean. The tidal cycle evolution of the horizontal flow and UVF structure are described below. Gradients in the harmonic and residual constituents of the flow are also examined in relation to their influence on the bay–ocean exchange.

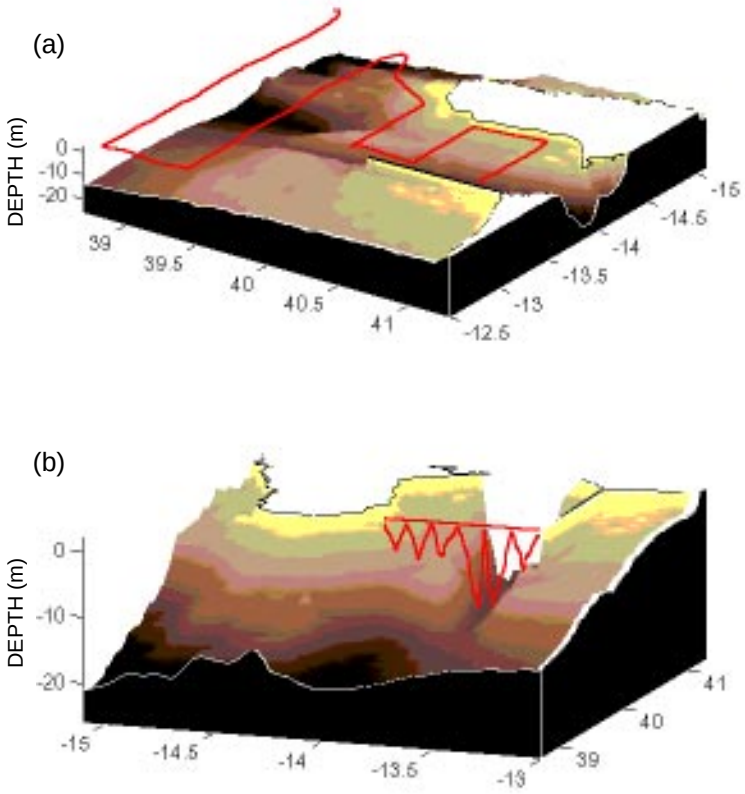

Figure 3. Location of (a) mapping and (b) cross-sectional transects. Heavy red line at surface shows the position of the boat during a typical transect, and the zigzag patterns show the position of towed sensors. Only surface water measurements were made during the mapping surveys.

The Ebb Tide

Maps for the surface circulation overlaid on fluorescence during the ebb are shown in figures 4a to 4d. At slack high water, the flow is weak with typical velocities of 5 to 10 $cm \cdot s^{-1}$ (figure 4a). The low fluorescence levels of water within the bay during this period is characteristic of the ocean water that entered the bay during the previous flood tide. Elevated residual UVF levels from the previous ebb tide are observed outside the mouth with maximum concentrations reaching about 15 to 20 $\mu g \cdot l^{-1}$. The developing stages of the ebb flow are characterized by strong southward flow within the entrance channel with velocities up to about 60 $cm \cdot s^{-1}$, with moderate south and

southeastward flow in the offshore region where typical velocities reach 20 to 30 cm·s^{-1} (figures 4b and 4c). The developed ebb flow shows a clear jet-like structure with centerline velocities near the entrance of about 60 to 70 cm·s^{-1} decreasing to 40 to 50 cm·s^{-1} at the outer transect. Highest UVF concentrations are observed emanating from within the bay, especially along the Zuniga Jetty where concentrations reach 30 to 40 µg·l^{-1}. Offshore, the width of the jet grows, and the jet turns eastward apparently due to the influence of the ambient longshore flow. During the mid to late ebb, high UVF water is observed to be concentrated in the southward flowing jet with lateral mixing occurring primarily in the strongly sheared eastward boundary, and to a lesser extent in the westward shear layer (figure 4d).

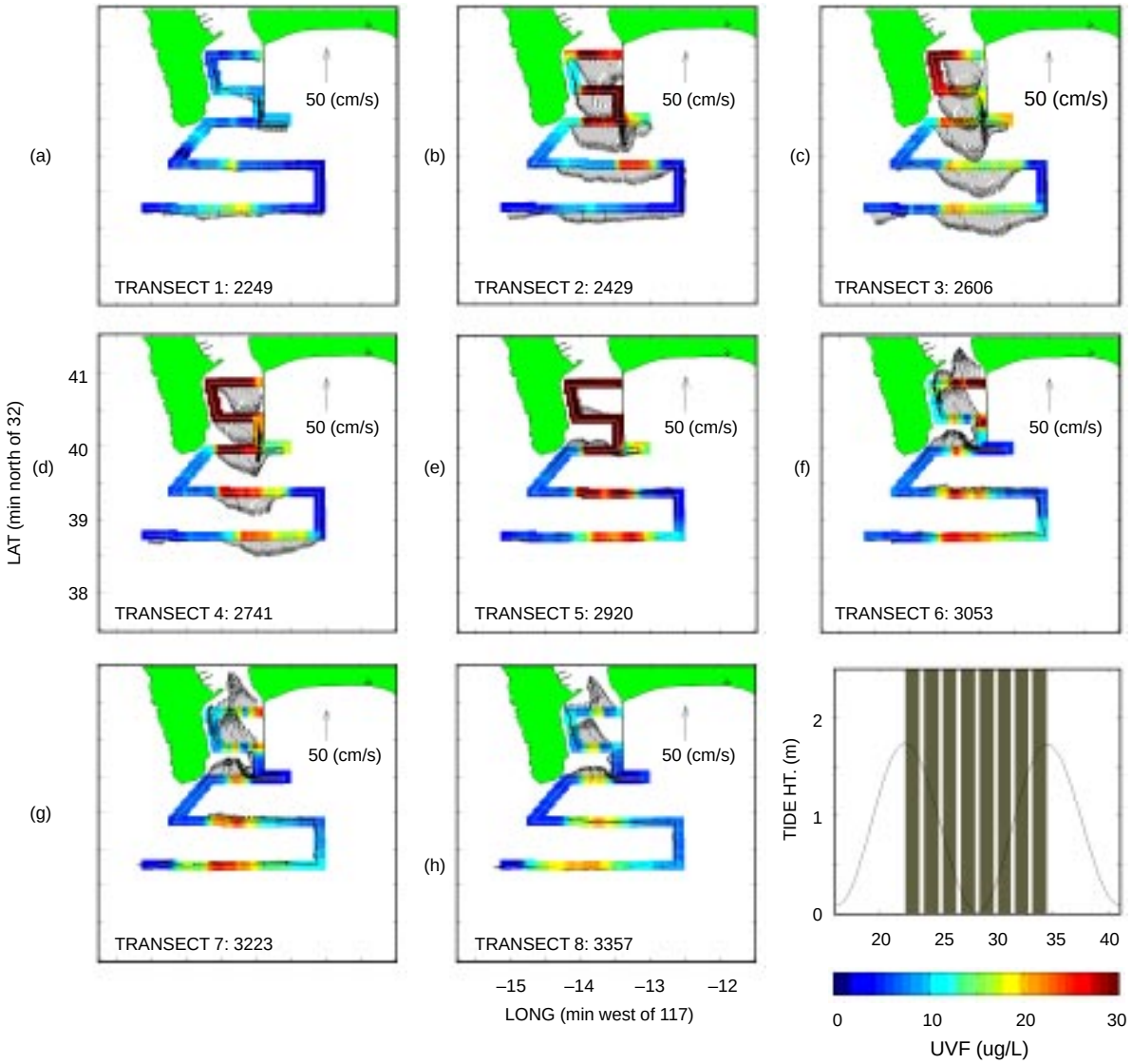

Figure 4. Horizontal structure of the tidal flow field and UVF concentrations from the mapping survey 95MAP.

The Flood Tide

Maps for the surface circulation overlaid on fluorescence during the flood tide are shown in figures 4e to 4h. As the flow reverses from ebb to flood, the momentum of the outflowing jet continues to carry water offshore in the region south of the entrance (figure 4e). High UVF water ejected from the bay during the ebb is observed to be drawn farther offshore in this ebb pulse. The flow reverses to flood first along the eastern and western shorelines and carries low UVF ocean water to the bay along these entrance boundaries. The ebb pulse of high UVF water is "pinched off" into a narrow neck by this low UVF water converging on the mouth. As the flood flow develops, the velocities within the entrance increase to 50 to 60 $cm \cdot s^{-1}$, while the offshore flow remains relatively weak in comparison to velocities observed during the ebb flow (figures 4f to 4g). The offshore flow appears to be drawn in predominantly from the south and east, while the inflow from the west is weaker. Within the region of strong convergence at the mouth, residual high-UVF bay water continues to be drawn in along a narrow region on the center axis of the entrance channel, while the concentration distribution offshore weakens and spreads. By the end of the flood, the region within the mouth is dominated by low UVF ocean water with a narrow band of residual bay water along the center axis (figure 4h). Offshore, the currents drop to typically $<5\ cm \cdot s^{-1}$, and a broad patch of residual bay water is observed in the region directly south of the mouth with concentrations reaching about $20\ \mu g \cdot 1^{-1}$.

Tidal Harmonics and Residuals of the Horizontal Exchange

The modeling studies of Awaji et al. (1980) suggest that characteristics of the tidal pumping process can be obtained from spatial variations of the tidal harmonics and tidally averaged residual circulation near the mouth. To test the validity of this modeling result, constituents of the flow were obtained by harmonically interpolating the spatially indexed components of the velocity at each index position assuming velocity variations of the form

$$u(t) = u_o + A_2 \cos\left(\omega_2 t + \phi_2\right) + A_4 \cos\left(\omega_4 t + \phi_4\right) + A_6 \cos\left(\omega_6 t + \phi_6\right) \quad , \qquad (4)$$

where u_o is the tidal residual, and A_i and ϕ_i are the amplitude and phase of the ith tidal constituent following the approach of Geyer and Signell (1990). From this, the magnitude and phase of the M2, M4, M6, and residual constituents for the north and east components of the velocity were obtained. The circulation was dominated by the M2 and residual constituents of the flow, which are shown in figures 5 and 6, respectively.

The maps in figures 5 and 6 confirm the existence of strong spatial gradients in the M2 and residual constituents of the flow associated with the strong ebb–flood asymmetry described above. The amplitude of the N–S component of the M2 velocity shows that strongest tidal flows are found within the bay entrance (60 to 70 $cm \cdot s^{-1}$) and in the jet region directly south of the mouth (20 to 50 $cm \cdot s^{-1}$). The M2 velocities to the east and west of the jet region are significantly weaker with typical amplitudes of 10 $cm \cdot s^{-1}$. In addition, the phase of the N–S component of the M2 velocity shows a phase lag in the region offshore from the mouth of up to 2 hours relative to the velocity at the entrance. The spatial distribution of the phase is similar to the amplitude with largest phase lags directly offshore from the mouth. The residual circulation also illustrates the effects of the ebb–flood asymmetry, with southward residual flows in the region offshore from the mouth reaching 10 to

15 cm-s^{-1}. Near the entrance, the residual velocities become weaker, with northward flow along the Point Loma shore and southward flow along the jetty. A large eddy structure is also observed in the offshore region to the east of the mouth. the effectiveness of these velocity and phase gradients in the tidal pump is evaluated below.

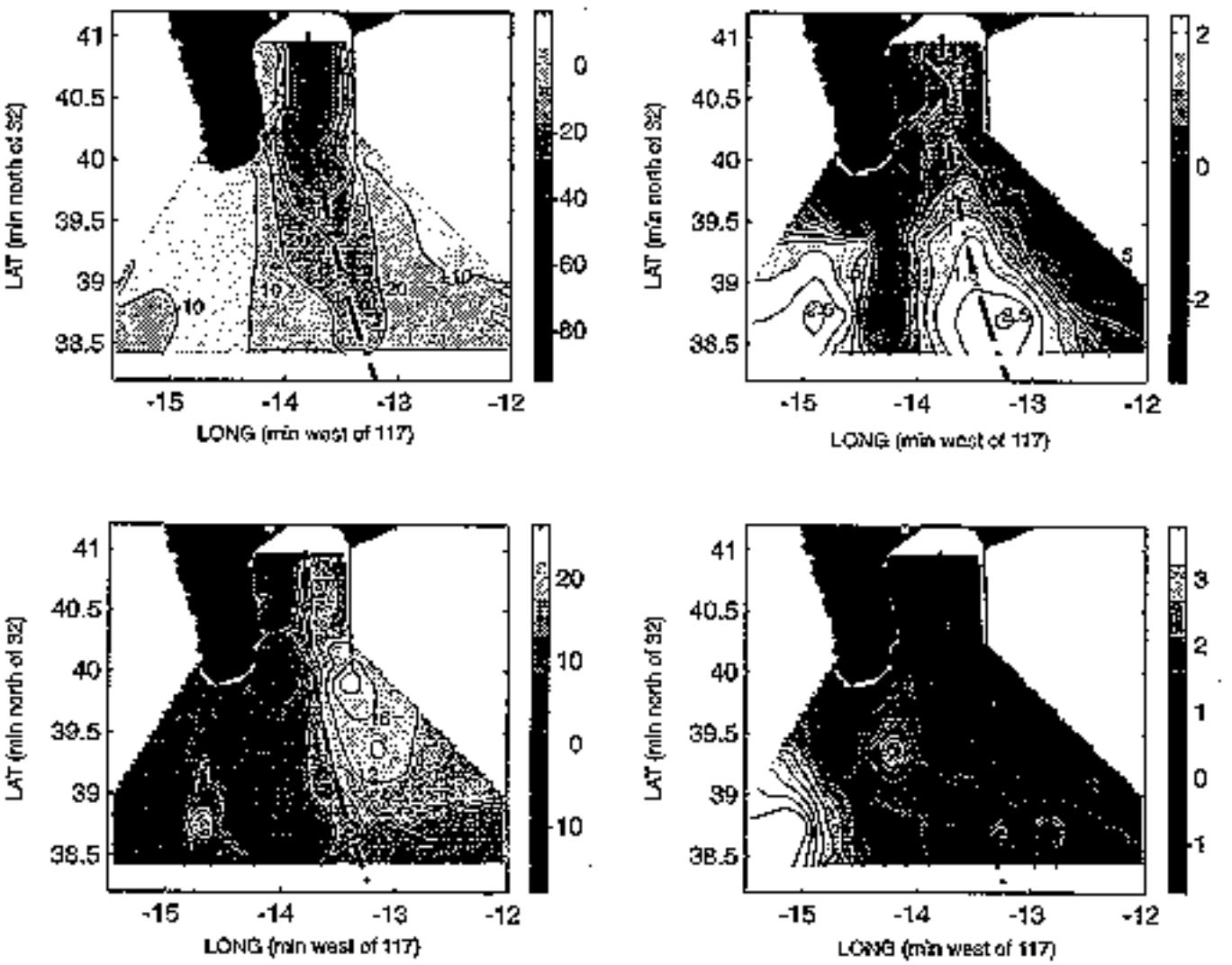

Figure 5. M2 tidal characteristics of the horizontal flow including (a) N–S amplitude, (b) N–S phase, (c) E–W amplitude, and (d) E–W phase. Velocities are in cm·s^{-1} and phase lag (+) is in hours from high water.

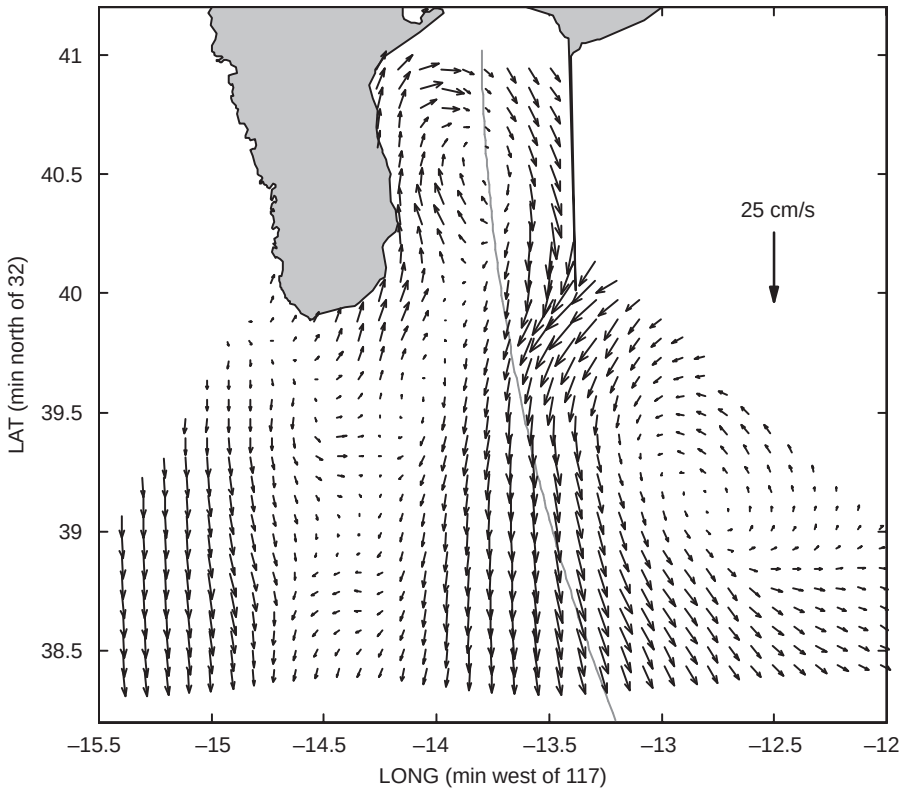

Figure 6. Horizontal structure of the tidally averaged residual flow.

One-Dimensional Trajectory Model for the Tidal Pump

Following Awaji et al. (1980), the effect of the spatial gradients described above can be considered from a Lagrangian perspective. For example, a particle released at the mouth during the ebb tide would be advected southward into a region where the amplitude of the velocity is weaker, and the phase is shifted later. The result will be that the particle will be unlikely to return to the mouth because the shifted phase will tend to continue to carry the particle offshore, while the weaker flow offshore will be less effective at returning the particle to the mouth once the flow does reverse. To evaluate the relative effect of the residual circulation, and the gradients in the tidal phase and amplitude, we constructed a one–dimensional model for the trajectory of fluid parcels along the centerline of the outflow. Based on the results above, only the residual circulation and the M2 tidal constituents were considered. Theory suggests that for a steady, plane jet the centerline amplitude of the outflow velocity should vary as $\sim x^{-1/2}$ (Fischer et al., 1979), while for a sink-type inflow, the velocity distribution is radially symmetric and decreases as $\sim x^{-1}$ (Ozsoy, 1978). Within the entrance channel, the amplitude of the velocity should be roughly independent of x. This suggests that the centerline gradient in the M2 amplitude, and the tidal residual component of the centerline flow result from the difference in how these two flows vary as a function of distance offshore from the mouth (x). Using these models for the centerline variation in tidal amplitude, a simple time-dependent, one-dimensional model of the velocity can be constructed as

$$u_{cl}(x,t) = u_{res} + u_{M2} \sin\left(\frac{2}{T} t + \right) \qquad x > 0$$
$$= u_o \sin\left(\frac{2}{T} t\right) \qquad x \geq 0 \quad , \tag{5}$$

where

$$u_{jet}(x) \approx u_o \left(1 + \frac{x}{x_o}\right)^{\eta} \quad , \tag{6}$$

$$u_{sink}(x) \approx u_o \left(1 + \frac{x}{x_o}\right)^{\pi} \quad , \tag{7}$$

$$u_{M2}(x) \approx \frac{1}{2}\left(u_{jet} + u_{sink}\right) \quad , \tag{8}$$

$$u_{res}(x) \approx u_{jet} - u_{M2} \quad , \tag{9}$$

$\phi(x)$ is the M2 phase along the centerline; u_o is the amplitude of the M2 tide at the mouth; and x_o is a length scale generally taken to be O(b), the width of the entrance.

The results from the mapping survey along the axis shown in figure 5 were fit to this model by setting $u_o = 70$ cm·s^{-1}, and adjusting x_o, α, and β to achieve the best fit between the predicted and measured centerline values for u_{jet} and u_{sink}. The best fit to the data was found using $x_o \approx 950$ m, which is in reasonable agreement with $b \approx 1000 - 1200$ m, $\alpha \approx -0.49$, and $\beta \approx -0.99$, in surprisingly close agreement to the theoretical values for a plane jet. The modeled values of u_{jet}, u_{sink}, u_{M2}, and u_{res}, and the measured values of u_{M2} and u_{res} are compared in figure 7 where it can be seen that this simple model provides a reasonable representation of these constituents of the centerline flow.

It seems likely that the phase lag is primarily due to the time scale for development and decay of the ebb jet in the offshore region that is not strongly influenced by the flood tide. This time scale can be bounded by two propagation velocities: the velocity associated with the propagation of the pressure gradient generated by the change in tidal elevation at the mouth, or the advective velocity of the ebb pulse that acquires momentum within the narrow channel of the bay entrance. The phase lag associated with these two time scales can be estimated as

$$_{pg} \sim \frac{x}{\sqrt{gh}} \quad , \tag{10}$$

$$_{ad} \sim \frac{x}{\hat{u}} \quad , \tag{11}$$

where ϕ_{pg} is the phase lag associated with the propagation of the pressure gradient, and ϕ_{ad} is the phase lag associated with advection of the ebb jet, and $\hat{u}$ is an average advective velocity in the offshore region of the jet. These two lines are plotted in comparison to the measured phase lag along the centerline axis in figure 7 taking $\hat{u} \approx 40$ cm·s^{-1}. From this estimate, it appears that the phase lag is related most closely to the advective time scale of the jet. At greater distance offshore, it seems likely that the validity of this simple relationship will break down because the phase will be regulated by the ambient flow rather than the tidal flow from the bay.

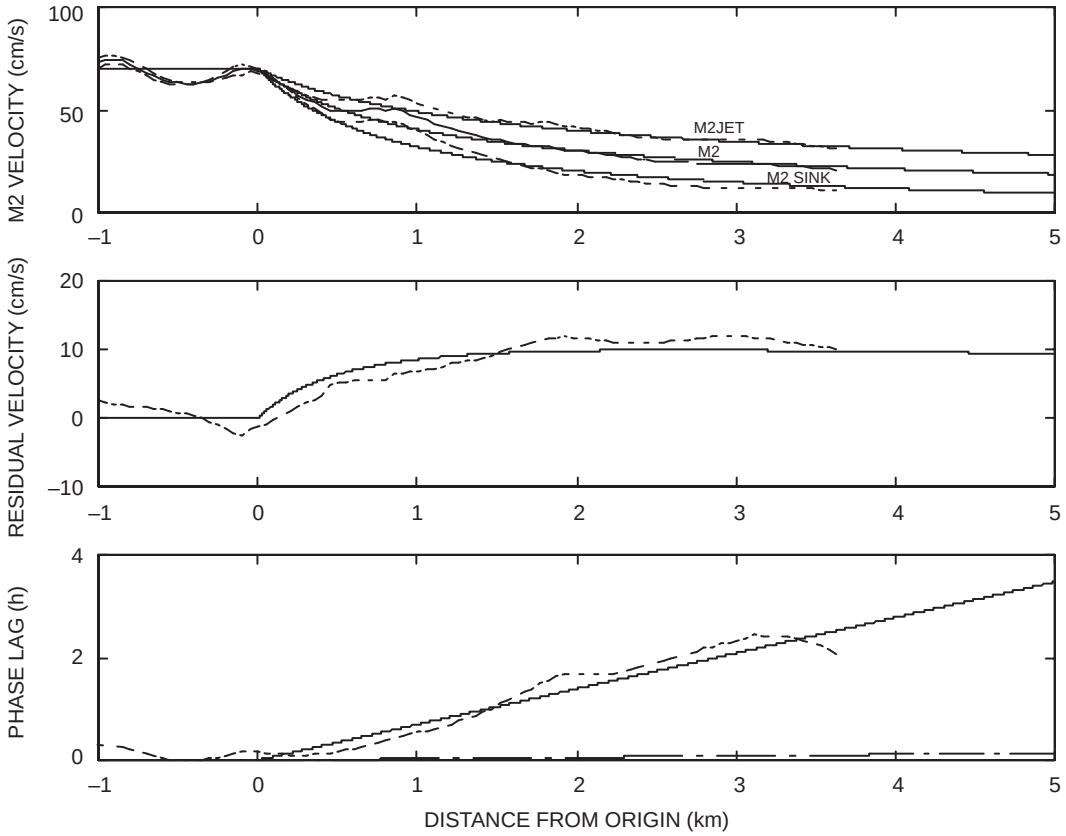

Figure 7. Fitted and measured centerline characteristics of the flow including (a) jet, sink, and M2 velocities; (b) residual velocity; and (c) phase lag.

These simple models of the centerline flow characteristics were then used to compare the net tidal trajectory of bay water parcels released at the mouth under the influence of the M2 and residual flows with and without phase lags. Trajectories were calculated using a finite difference representation of the equation

$$x_i = x_{oi} + \int_0^T u_i(x,t)dt \quad , \tag{12}$$

where x_i is the net tidal trajectory due to a given component of the flow u_i, and x_{oi} is the starting position of the parcel. From this we can predict independent trajectories due to the residual circulation, and the M2 flow, including the separate contributions from the gradients in amplitude and phase (figure 8). Of particular interest is the comparison of the combined effect of the residual circulation and M2 amplitude gradient, both of which we attribute to the tidal asymmetry with the effect of the M2 phase gradient. We attribute this primarily to time lag in flow reversal due to the momentum pulse of the ebb jet. Thus, we see that the displacement associated with the tidal residual flow is about 3.3 km, while the displacement associated with the M2 flow alone is about 5.3 km. The two effects combine in a nonlinear fashion (i.e., $d_{M2} + d_{res} \neq d_{M2+res}$) to produce an offshore displacement of about 5.4 km. The effect of the phase shift is to reduce the offshore displacement during much of the ebb flow, and increase the displacement during the flood as the water offshore continues

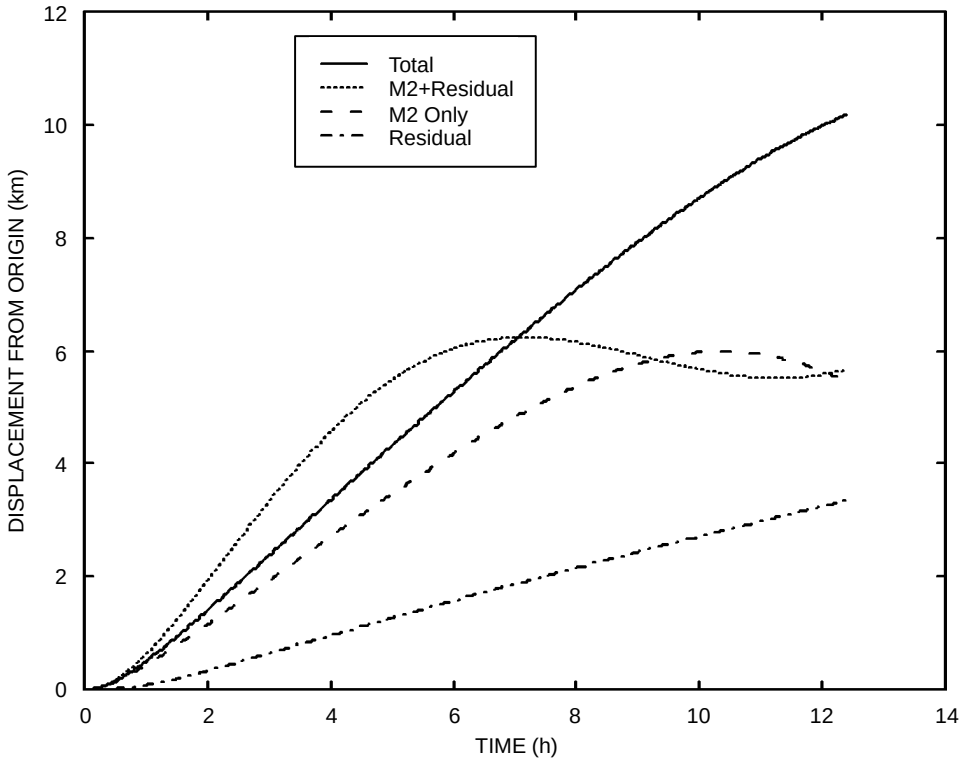

Figure 8. Predicted one-dimensional trajectories of particles released at the mouth of the bay at slack high water.

to move away from the bay for some time. The overall displacement, including the residual flow and the M2 velocity and phase, is about 10 km.

CROSS-SECTIONAL FLUXES AND THE TIDAL EXCHANGE BUDGET

While the mapping transects and axial sections above provide a means of visualizing the exchange between the bay and ocean, cross sections performed at the mouth of the bay provide a specific means of quantifying the net tidal exchange of bay and ocean water. The cross-sectional tidal evolution of velocity and UVF used to construct the exchange budget are shown in figures 9 and 10. Many of the exchange characteristics observed in the mapping transects and axials are reflected in the cross sections.

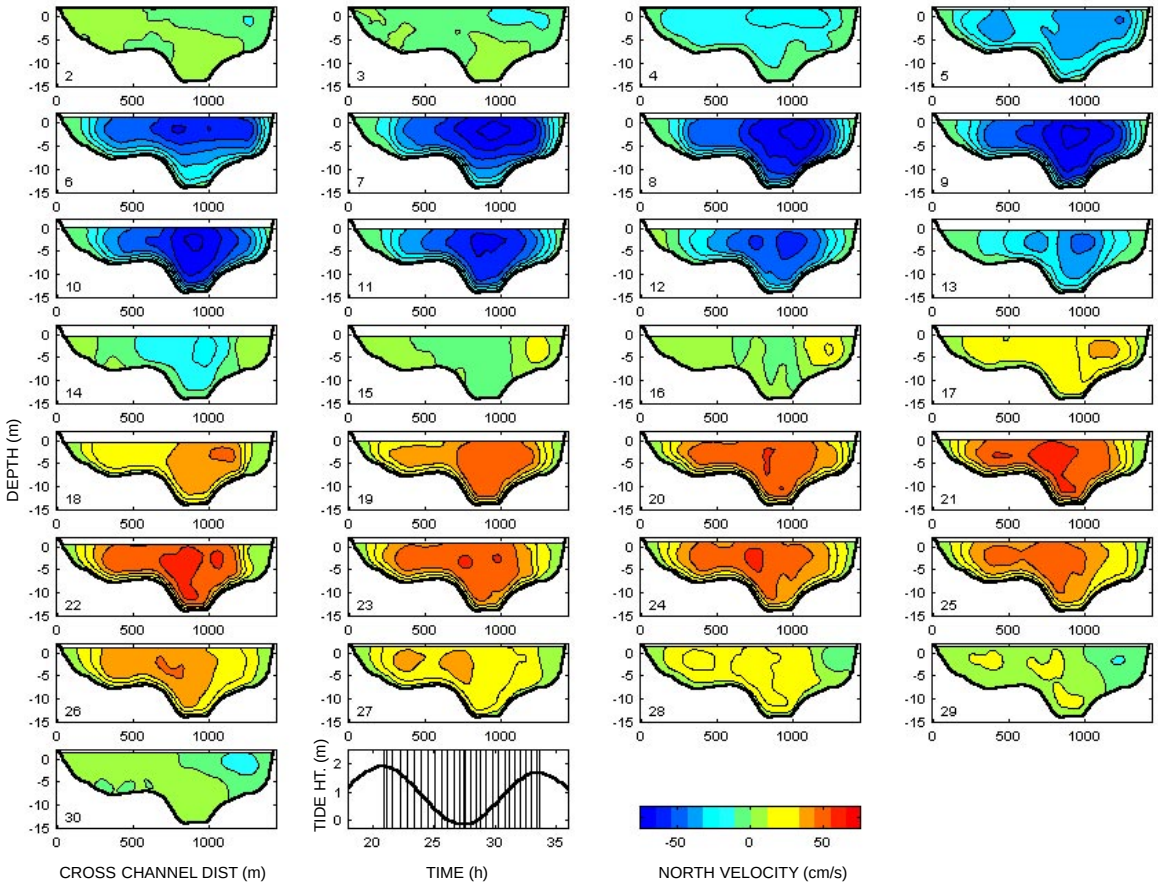

Figure 9. Cross-sectional time series of flow at the mouth section during 95MOUTH-2.

Cross-Sectional Structure of the Exchange

The cross-sectional flow structure is characterized by strong vertical shear during the ebb tide. Highest velocities are observed in the channel near the surface reaching about 80 $cm \cdot s^{-1}$. The UVF concentrations are initially quite low and increase as the ebb tide progresses. Highest concentrations are observed near mid-channel extending throughout the water column. During the transition from ebb to flood, low UVF ocean water converges into the mouth of the bay along both boundaries of the channel, while high UVF bay water is restricted to the central part of the channel. This trend continues into the early stages of the flood tide as high UVF bay water is drawn back into the bay via a narrower and narrower region of the channel. The vertical-flow structure during the flood tide is more uniform with velocities of up to about 60 $cm \cdot s^{-1}$ throughout much of the section. During the mid-to-later stages of the flood, UVF levels drop significantly, and the distribution becomes vertically stratified with the highest levels near the surface along the western boundary.

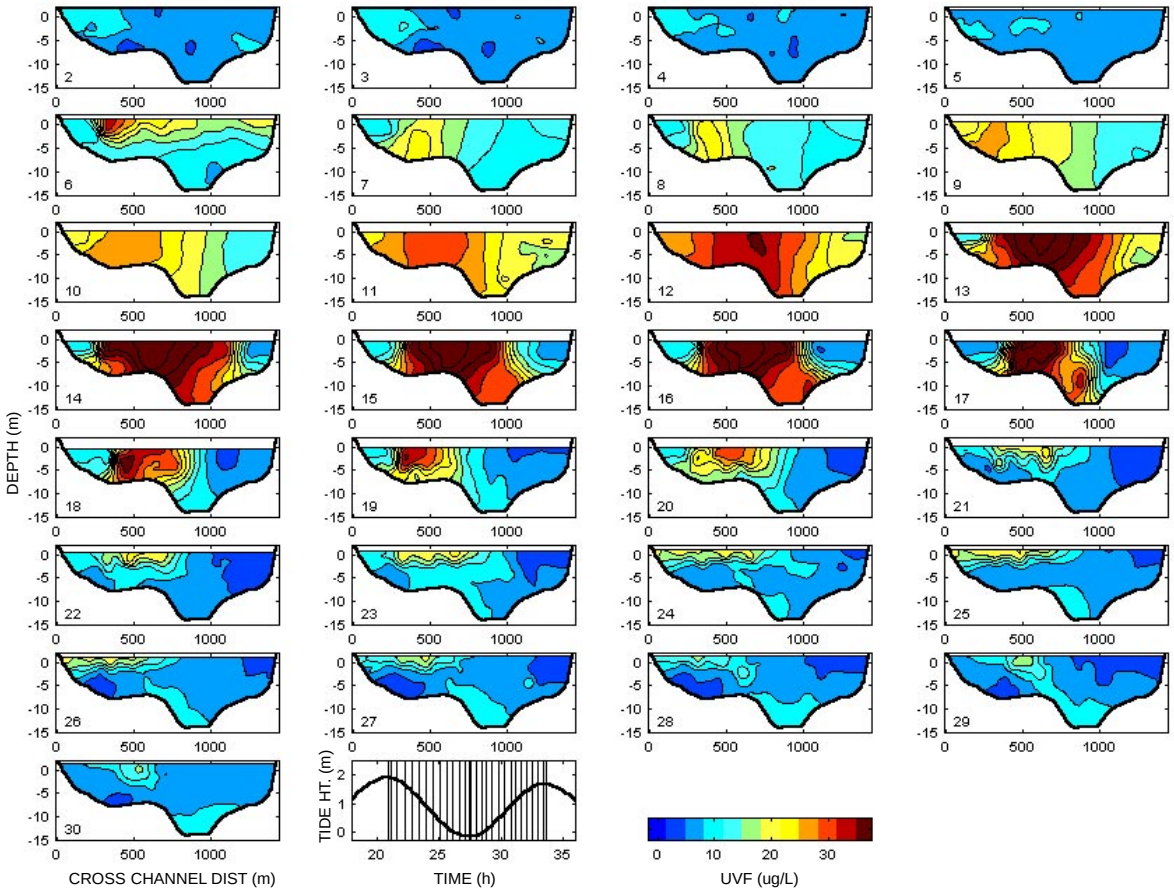

Figure 10. Cross-sectional time series of UVF at the mouth section during 95MOUTH-2.

Tidal Evolution of the Exchange

Using the velocity and UVF data from the cross sections, the tidal evolution of the exchange was evaluated based on the classical decomposition approach originally proposed by Dyer (1974). In this analysis, the primary terms considered included (1) the flux due to temporal correlations in the sectional averages of velocity and UVF, (2) the flux due to spatial correlations in the time averaged velocity and UVF, and (3) the turbulent flux due to short-term time and spatial correlations. Following Fischer et al. (1979), the net flux can be estimated from

$$\dot{M} \approx A\left[u_a c_a + (u_c c_c) + \overline{u_s c_s} + \left(\overline{u'c'}\right)\right] \quad , \qquad (13)$$

where A is the cross-sectional area, u_a and c_a are the tide cycle averages of the sectionally averaged velocity and concentration, u_c and c_c are the cross-sectional averages with the u_a and c_a removed, u_s and c_s are the tidal cycle averages with u_a and c_a removed, and u' and c' are remainders or fluctuating terms. Physically, the first term is generally associated with tidal trapping and pumping, the second with the residual circulation, and the third with oscillatory shear flow. In estuaries with strong gravitational circulation, it is common to further decompose the spatial residuals into vertical and transverse contributions. However, in this case, it will be shown that the residual contribution is small and will be kept to a single term. Although river flow is negligible in San Diego Bay, the classical term

associated with net flux due to a steady river inflow, Au_ac_a, may still contribute if the tide is not purely symmetrical. There are several other terms that result from the decomposition and that are generally neglected (Fischer et al., 1979).

The transport of UVF from the bay, and the contribution to the transport by the three primary terms described above are summarized in table 1. The analysis shows that the transport from the bay to the ocean is dominated by the correlation between sectionally averaged flow and concentration, which contributes about 72 percent of the total transport. Another 25 percent of the transport comes from the product of the net tidal flow and concentration, a term which would be zero if the tide were purely symmetric. The contribution from the residual term is small and bayward, representing only about 3 percent of the transport. The shear term also contributes slightly with about 6 percent of the transport to the ocean. Together, the sum of the four transport terms is nearly identical to the measured transport (M), suggesting that neglected terms are probably small. Thus, aside from the steady transport term due to the tidal asymmetry, the transport from the bay to the ocean appears to be dominated by correlations in the cross-sectional average properties.

Table 1. Contributions to transport from various coupling terms for the 95MOUTH–2 survey.

Transport Term	UVF Transport ($kg \cdot day^{-1}$)	% of Total	Diffusivity ($m^2 \cdot s^{-1}$)
M	1350	–	348
Au_ac_a	340	25	87
$A(u_cc_c)$	970	72	250
Au_sc_s	–40	–3	–11
$Au'c'$	80	6	20
Sum	1342	99	

The tidal evolution of the cross-sectional average terms u_c, c_c, and the transport due to their correlation $A(u_cc_c)$ is shown in figure 11. Cross-sectionally averaged velocities reach 40 to 50 $cm \cdot s^{-1}$, and they display a dominant semidiurnal variation. Within the bay, we might expect that this flow would simply result in the advection back and forth of the concentration gradient, with no significant net tidal transport. However, near the mouth, we see that UVF time series evolves in three phases with (1) a gradual increase in concentrations during the ebb, (2) a rapid decrease during the early flood, and (3) a period of nonvarying, low concentrations during the mid to late flood. This asymmetry in the time variation of UVF concentration results in a strong correlation with the time variation in flow, leading to a net seaward (negative) flux of UVF.

To clarify this, we assume the concentration gradient (c_x) within the bay to be roughly linear, and thus during the first phase, the variation in c due to the tidal advection of bay water past our measurement section should follow $c_t = uc_x$, where c_x is a constant. Integrating and using the tidal prism to estimate u, we have

$$c_e(t) = c_{oe} + \left(\frac{A_b}{A_m}\right)\eta_o c_x \cos\left(\frac{2\pi t}{T}\right) \quad , \tag{14}$$

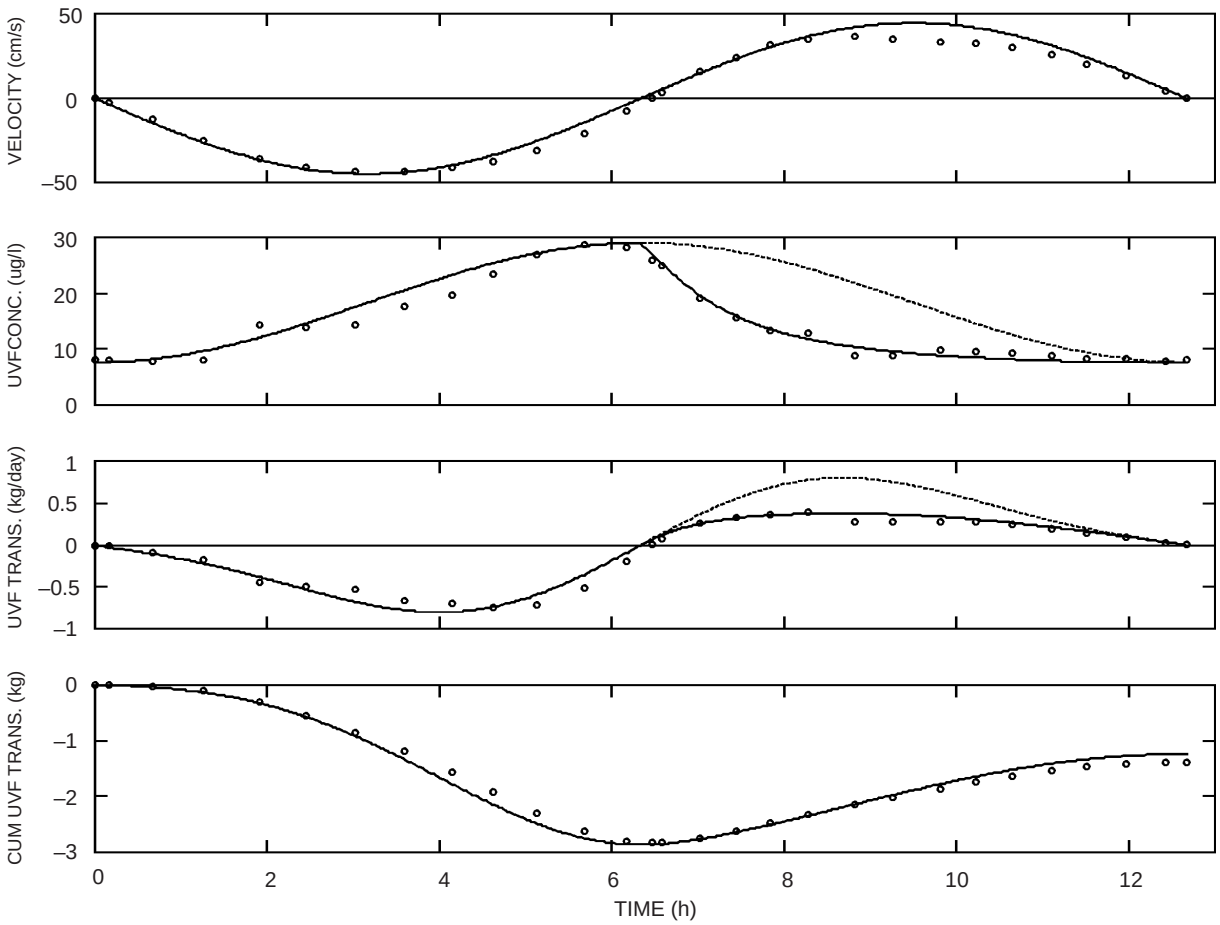

Figure 11. Time series of cross-sectional averages of (a) velocity, (b) UVF, (c) UVF transport, and (d) cumulative UVF transport. Open circles are measured data; solid lines are modeled results from equation 14 for the ebb tide and equation 15 for the flood tide. The dashed line represents the expected concentration and transport in the absence of tidal pumping.

where c_{oe} is the concentration during the ebb, A_b is the surface area of the bay, A_m is the surface area of the mouth, and η_o is the tidal amplitude. This line is also shown in figure 11b where a reasonable fit is obtained to the actual ebb-tide concentration data using $c_x = 3.3\ \mu g \cdot l^{-1} \cdot km^{-1}$, in good agreement with the observed gradient (Chadwick et al., 1996). Physically then, the similarity between the measured and predicted concentrations during the ebb indicate that the outward transport is dominated by the advection of the longitudinal concentration gradient in UVF. Observed variations from this trend can be attributed to deviations in the concentration gradient that may result from trapping regions within the bay, for instance in the lee of Ballast Point.

The concentration deficit observed during the flood tide can be explained by the strong convergence of low UVF ocean water into the mouth from regions not influenced by the outflow. This could be associated with either the horizontal or vertical pumping processes described in the previous sections. Returning to the simple jet–sink model of Stommel and Farmer (1952), we suppose that the ebb jet can be described as a simple rectangular jet. The concentration in the jet is presumed to decrease offshore in accordance with the observed concentration gradient, c_x. The inflow during the

flood draws water from the semicircular withdrawal zone offshore, which includes some portion of the outflow. Then, during the flood, consider that the water is drawn in from expanding semicircular regions offshore out to the limit of the flood withdrawal zone. The concentration should vary as

$$c_f\,(t) \approx f_b c_b = f_o c_o \approx c_o = f_b\left(c_b - c_o\right) \quad , \tag{15}$$

where f_b and c_b are the fraction of bay water and concentration of the bay water, and f_o and c_o are the fraction of ocean water and concentration of ocean water at a given semicircular offshore region.

Assuming the withdrawal zone is determined by the tidal prism, a standing wave tide within the bay, and a linear concentration gradient in the offshore jet at the end of the ebb, the following relationships can be established

$$f_b(r) \approx \frac{b}{w\pi r}\sin^{-1}\left(\frac{b}{2r}\right) \quad ,$$

$$c_b\,(r) \approx c_{oe} = c_x\left(2\eta_o\left(\frac{A_b}{A_m}\right) - r\right)\ (x \approx r \text{ along the centerline}) \quad , \tag{16}$$

$$r(t) \approx r_o = \sqrt{\frac{\eta_o A_b}{\pi w h}\left(1 = \cos\left(\frac{2\pi t}{T}\right)\right)} \quad ,$$

where c_o is the concentration of the ocean water, $c_{oe} = c_f(T)$ is the concentration at the beginning of the ebb tide, w is the fraction of a complete circle occupied by the withdrawal zone, r is the radial distance offshore, and r_o is an initial radius to account for the non-zero breadth of the sink. The equations above were solved by using the known values of b ≈ 1200 m, $A_b \approx 4.15\cdot10^7$ m^2, $A_m \approx 1.35\cdot10^4$ m^2, Δ_o / 1.05 m, c_o / 5 λg·1^{-1}, h / 12 m, r_o / b/2, and then adjusting w to achieve the best fit to the measured data since the actual extent of the withdrawal zone is not known. Good agreement to the measured data was obtained using a value of w / 0.42, and the result is shown plotted as a solid line during the flood tide phase in figure 11b.

The correlation between the cross-sectional average velocity and concentration results in transport of UVF from the bay to the ocean. This can be seen in figures 11c and d, which show the UVF transport and cumulative UVF transport, respectively. The UVF transport is simply the product of the velocity and concentration, while the cumulative transport is the integral of that product between time = 0 and time = t. While the velocity is substantially symmetrical with the tide, the low concentrations during the flood tide result in a significantly lower inward transport during the flood than the observed outward transport during the ebb. Thus, while up to about 2.9 kg·UVF is exported to the ocean during the ebb, only about 1.6 kg·UVF is returned to the bay during the flood, resulting in a net transport of about 1.3 kg·UVF·tide^{-1} to the ocean (figure 11d).

SUMMARY AND CONCLUSIONS

Taken together, the observations described here provide a unique view of tidal exchange at the bay–ocean boundary for a prototype system. Visualization of the tidal evolution of flow and tracers suggests that, in accordance with the classical tidal-pumping model, the horizontal dynamics at the mouth of San Diego Bay are governed by an asymmetry between the jet-like nature of the ebb flow, and the sink-like nature of the flood flow. This asymmetry results in a strong M2 amplitude gradient similar to that modeled by Awaji et al. (1980). Observations also support the presence of a significant phase lag in the offshore flow, resulting primarily from the time required for development and decay of the ebb jet. A one-dimensional trajectory model based on the observations indicates that the combined influence of the residual circulation and the offshore gradients in the M2 amplitude and phase gradients provide the mechanism by which particles from the bay are ejected to the ocean. This pumping of the offshore flow produces a strong correlation between the sectional-average velocity and bay-water concentration, resulting in a significant net tidal exchange between the bay and ocean.

REFERENCES

Awaji T., N. Imasato, and H. Kunishi. 1980. "Tidal Exchange through a Strait: A Numerical Experiment Using a Simple Model Basin," *Journal of Physical Oceanography*, vol. 10, pp. 1499–1508.

Chadwick, D. B, C. N. Katz, and J. L. Largier. 1995. "Contaminant Transport Measurements in San Diego Bay," *Proceedings of Oceans '95*, San Diego, CA, vol. 3, pp. 1691–1699.

Chadwick, D. B., J. L. Largier, and R. T. Cheng. 1996. "The Role of Thermal Stratification in Tidal Exchange at the Mouth of San Diego Bay," in *Buoyancy Effects on Coastal Dynamics*, edited by D. G. Aubrey, American Geophysical Union, Washington, DC, pp. 155–174.

Cheng, R. T., P. F. Wang, K. Richter, E. Gross, D. Sutton, and J. Gartner. (in prep). *Modeling Tidal Hydrodynamics of San Diego Bay, California*.

Dyer, K. R. 1974. "The Salt Balance in Stratified Estuaries," *Estuarine and Coastal Marine Science*, vol. 2, pp. 275–281.

Fischer, H. B., E. J. List, R. C. Y. Key, J. Imberger, N. H. Brooks. 1979. *Mixing in Inland and Coastal Waters*, Academic Press, San Diego, CA.

Geyer, W. R. and R. P. Signell. 1990. "Measurements of Tidal Flow around a Head-Land with a Shipboard Acoustic Doppler Current Profiler," *Journal of Geophysical Research*, vol. 95, pp. 3189–3197.

Joshi, P. B. 1982. "Hydromechanics of Tidal Inlets," *Journal of Port, Waterway, Harbor, and Ocean Division*, American Society of Civil Engineers (ASCE), vol. 108 (WW3) pp. 239–253.

Katz, C. N., and D. B. Chadwick. 1991." Real-Time Fluorescence Measurements Intercalibrated with GCMS," *Proceedings of Oceans '91*, Honolulu, HI, vol. 1, pp. 351–358.

Katz, C. N., D. B. Chadwick, and L. Skinner. 1995. "Input of Polynuclear Aromatic Hydrocarbons to San Diego Bay from Creosote Pier Pilings," *Proceedings of Oceans '95*, San Diego, CA, vol. 3, pp. 1722–1729.

Metha, A. J. and P. B. Joshi. 1988. “Tidal Inlet Hydraulics,” *Journal of Hydraulic Engineering*, vol. 114, no. 11, pp. 1321–1337.

Olea, R. A. 1974. “Optimal Contour Mapping Using Universal Kriging,” *Journal of Geophysical Research*, vol. 79, no. 5, pp. 695–702.

Ozsoy, E. 1977. “Flow and Mass Transport in the Vicinity of Tidal Inlets,” University of Florida, Gainesville, Coastal and Oceanographic Engineering Department, Report #UFL/COEL/TR–036.

Peeling, T. 1974. “A Proximate Biological Survey of San Diego Bay, California,” NURDC TR 389, Naval Undersea Research and Development Center, San Diego, CA.

Stommel, H. and H. G. Farmer. 1952. “On the Nature of Estuarine Circulation,” Woods Hole Oceanographic Institution, Reference Nos. 52–61, 52–63, 52–88.

Tenekes, H. and J. L. Lumley. 1972. *A First Course in Turbulence*, The MIT Press, Cambridge, MA.

Wilkenson, D. L. 1978. “Periodic Flows from Tidal Inlets,” *Proceedings of the Coastal Engineering Conference*, ASCE vol. 16, no. 2, pp. 1336–1346.

Wolanski, E. and J. Imberger. 1987. “Friction-Controlled Selective Withdrawal Near Inlets,” *Estuarine, Coastal and Shelf Science*, vol. 24, pp. 327–333.

Detection Algorithms Derived from Gaussian Mixture and Hidden Markov Noise Models with Applications to Radar and Sonar

D. W. J. Stein

Acoustic and electromagnetic noise at the output of sonar and radar receivers, respectively, may be non-Gaussian. Detection theory suggests that, in these circumstances, detection algorithms derived from more appropriate models may have improved performance vis-a-vis detection algorithms derived from the assumption of Gaussian noise. Gaussian mixture probability densities (GMPDs) may be used to model data that are more heavily tailed than normal, such as various types of impulsive noise. In particular we show that GMPDs and, more generally, hidden Markov models (HMMs) may be used to model ocean acoustic noise that is dominated by a few moving sources and radar back scatter from the sea surface. Locally optimal detection statistics are then derived for random signals (signals having zero mean, due perhaps to a random phase) in noise whose probability density has continuous second-order partial derivatives. This result is applied to Gaussian mixture and hidden Markov noise. Likelihood ratio detection statistics are also derived for signals in hidden Markov noise. A robust implementation of the Gaussian mixture detector, which mitigates the effects on detection performance of discrepancies between the parameter values used to process a given time series and the best fitting parameter values of the noise component of the test data, is presented. Receiver operating characteristics (ROCs) for the Gaussian mixture and power detectors are calculated to demonstrate the theoretical performance improvement of the mixture detector in mixture noise. The detection performance of the constant false alarm rate (CFAR), hidden Markov and Gaussian mixture detectors are then compared on a small sample of radar data. Empirical ROC curves of the robust implementation of the Gaussian mixture detector and the best of several CFAR detectors are obtained for a large set of high-resolution radar data. These curves indicate that the average performance improvement of the mixture detector over the CFAR processor was up to 9 dB, depending upon the false alarm probability.

INTRODUCTION

Non-Gaussian noise is often observed in the output of electromagnetic and acoustic receivers. However, the Central Limit Theorem states that the probability distribution of the sum of a number of identically distributed sources approaches a normal distribution as the number of terms approaches infinity.[1] Thus non-Gaussian noise may be observed if the noise is dominated by a few non-Gaussian sources, or the noise is produced by a changing number of Gaussian or non-Gaussian sources, even if the expected number of sources is large.[2] The class *A* [12 – 14] and the *K* [7,33,34] distributions are frequently used to model non-Gaussian noise for surveillance and communication applications.[3] These distributions may be derived from the assumption that the noise is produced by a fluctuating number of sources. The class *A* distribution may be derived by assuming that the noise is the sum of

[1]More general formulations of the Central Limit Theorem are presented in [5].
[2]The magnitude and magnitude squared of a complex Gaussian random variable have Rayleigh and exponential distributions, respectively, and depending upon the context, the term “non-Gaussian” could refer to non-Rayleigh or non-exponential distributions.
[3]The Weibull [4] and lognormal [3] distributions have also been widely used to model radar sea clutter.

the responses from a number of identical Gaussian sources and that the number of sources has a Poisson distribution [1]. The *K* distribution arises as a limiting distribution in case the number of sources has a negative binomial distribution with an expected value that approaches infinity [21,7], and the sources have identical, not necessarily Gaussian, distributions.

The class *A* and *K* distributions are Gaussian mixture distributions, and they can be derived from a compound representation of the noise process. The random variable *X* is represented as a compound random variable by $X = AU$ where *A* and *U* are random variables, and $A > 0$. If, furthermore, *U* is a d-dimensional (real or complex) normal random vector with mean μ and covariance matrix Σ, then given $A = a$, *X* has the normal distribution $N(a\mu, a^2\Sigma)$. Therefore, the unconditional distribution of *X* is

$$p_X(x) = \int_0^\infty N(a\mu, a^2\Sigma)(x) d\mu_A, \tag{1}$$

where μ_A is the distribution of *A*. If *A* is discrete, i.e., $p(A = a_i) = p_i,\ i \leq 1 \leq m$, where *m* is the number (possibly infinite) of states or possible values of *A*, then *X* has a discrete Gaussian mixture distribution

$$p_X(x) = \sum_{i=0}^{m} p_i N(a_i\mu, a_i^2\Sigma)(x). \tag{2}$$

If $\mu = 0,\ d = 1,$ (assumptions maintained throughout the remainder of this paper) and *A* has a gamma or Poisson distribution, then $|X|$ has a *K* [33] or class-*A* distribution [1], respectively. The finite state Gaussian mixture model, i.e., with *m* finite, may therefore be used to approximate either class *A* or *K* distributions [1,32,28] and also noise, which is the sum of *K*-distributed and normal components [28,29].

There are various techniques to detect signals in non-Gaussian noise. If the noise-only and signal-plus-noise densities are known, then a likelihood ratio test, using the Neyman–Pearson criterion, provides the greatest probability of detection for a given false alarm rate [18]. If these densities are not known, then other approaches may be used. The minimax approach [8] defines classes of noise or signal-plus-noise density functions and then uses the detector, which minimizes the maximum expected error over the classes. For example, while the matched filter is equivalent to a likelihood ratio for known signals in stationary independent Gaussian noise, the correlator-limiter is the minimax detector for a known signal in stationary independent noise with a distribution belonging to the class of ϵ-contaminated mixture distributions with a nominal Gaussian distribution. Nonparametric techniques are designed to work for more general classes of probability densities than is the minimax approach. For example, if the noise density is in the class of densities with median value zero and the signal-plus-noise density is not in this class, then the sign test provides a nonparametric means of detecting the signal [18]. If the signal-to-noise ratio is small, and if the noise density can be approximated by a member of a parametric family of densities for which the parameters can be estimated, or the noise density can be estimated nonparametrically, then locally optimal detection algorithms, which are based on Taylor approximations of the likelihood ratio, may be employed [11,15–18].

We show that Gaussian mixture densities can be used to model ocean acoustic data dominated by a few moving sources and radar sea clutter. More generally, hidden Markov models (HMMs) that include correlation in successive values of *A* are applied to radar sea clutter data. Amplitude only and phase coherent detection algorithms based on these models are derived. Implementations that mitigate the effect of parameter error are presented, and the performance of the algorithms are evaluated theoretically and by applying them to radar data.

OCEAN ACOUSTIC DATA

Ocean acoustic noise dominated by wind, waves, and/or distant shipping has been shown to have normal distributions whereas data dominated by local shipping or sea life may be non-Gaussian [2, 9, 10, 19, 23, 24, 25]. This study, [25], evaluated the characteristics of local shipping noise. The envelope of a sinusoid and Gaussian noise has a Ricean distribution [31], and this model is often used for the narrowband components of local shipping. The Ricean distribution predicts less variation about the mean than is predicted by the Rayleigh distribution [31, figure 1]. Several ocean acoustic data sets containing narrowband interference were identified and statistical characteristics of time series of the Fourier coefficients at the relevant frequencies were analyzed [25].

Plots of the cumulative distributions showed that narrowband interference could also be more heavily tailed than the normal distribution. For example, figure 1 compares the empirical distribution of the magnitude squared of such data with the one-, two-, and three-state exponential distributions. The significance level of the chi-squared goodness of fit scores for the one-, two- and three-state models were 0.0, 0.0, and 0.005, respectively. Thus, this data set was substantially better described by the three-state Gaussian mixture model than by the Gaussian model. Thus, ocean acoustic data containing narrowband interference may have greater fluctuations than are predicted by the normal and Ricean distributions.

This observed level of fluctuations was shown in [25] to be a propagation effect. Assume a sinusoidal source of frequency, ω_0. If k_n is the horizontal wave number of the n^{th} mode, v is the speed of the source, θ is the angle less than or equal to $\frac{\pi}{2}$ between the perpendicular from the receiver to the source track and the line from the receiver to the source; $v_n^G = [\partial k_n / \partial \omega(\omega_0)]^{-1}$ is the n^{th} mode group velocity, then the Doppler-shifted horizontal wave numbers are $\tilde{k}_n = k_n(1 - (v/v_n^G) \sin(\theta(t)))$ [6]. As different modes are shifted by different amounts, they beat against each other. Consequently, under conditions delineated in [25], the distribution of the amplitude is more heavily tailed than Rayleigh distributed data.

RADAR SEA CLUTTER

The applicability of exponential mixture distributions to low-pulse-rate, high-resolution sea clutter is demonstrated empirically in [28]. A 500-Mbyte data set consisting of nearly 500,000 1-second time series of 64 pulse-per-second radar sea clutter data was fit to exponential and two- and three-state exponential mixture densities: m = 1, 2, 3. The parameters of the exponential mixture densities were estimated for each time series by using the expectation maximization (EM) algorithm and the goodness of fit was evaluated using the significance level of the chi-squared-goodness of fit test. Figure 2 shows that the significance levels of the tests for the exponential and the best of the one-, two-, or

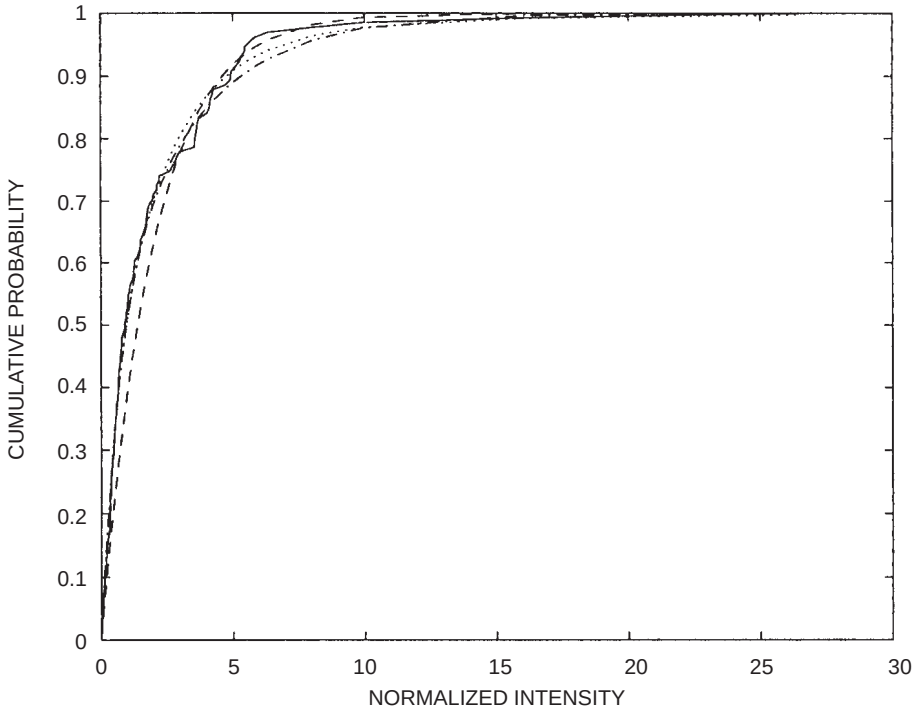

Figure 1. The cumulative distribution of the normalized intensity of narrow-band acoustic interference (—) is compared with the exponential (– –), the two (= ≈ ≠), and the three (·····) state exponential mixture distributions.

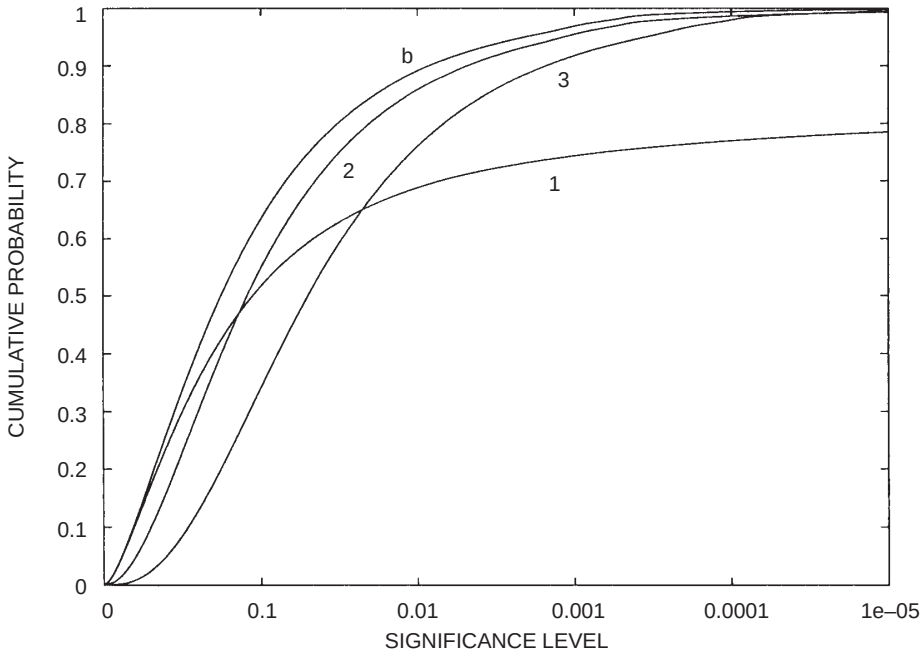

Figure 2. Cumulative distributions of the significance level of the chi-squared goodness of fit statistic calculated for the best-fitting exponential (1), two-state exponential (2), three-state exponential (3), and the best fitting of these three models (b) applied to high-resolution radar data.

three-state exponential mixture densities are above 0.0001 for approximately 75 percent and virtually all of the time series, respectively.

HIDDEN MARKOV MODELS

Time series models, as opposed to univariate probability distributions, that incorporate correlation in the components, *A* and *U*, of the compound representation, may better describe the sea clutter. Ward et. al. [34] show that a compound model in which *A* is correlated and *U* is uncorrelated is applicable to the sea clutter in the output of frequency agile radars. Assuming discrete sampling, the simplest correlation model for *A* is derived from the Markov hypothesis, i.e., that the current value of *A* depends on the immediately prior sample of *A* and is independent of earlier samples. $X = AU$ is then the output of a hidden Markov model [20,30]. The parameters of this hidden Markov model are the state transition matrix, the variance of the normal density for each state, and the initial probability distribution on the set of states. These parameters may also be estimated by using the EM algorithm [35].

The relative merit of the HMM and Gaussian mixture models may be assessed by comparing the average log-likelihood of these models. The univariate distribution of the output of an HMM does not reflect the correlation of the underlying Markov process. Therefore, univariate goodness-of-fit tests may not be used to compare the validity of the HMM and Gaussian mixture approaches to modeling data. If $\vec{x}$ is a data vector of length *n*, then the average log-likelihood of $\vec{x}$ is $(\frac{1}{n}) \log(p(\vec{x}|\hat{\theta}))$, where $\hat{\theta}$ is a maximum likelihood estimate of the parameters of the model. Figure 3 compares the average log-likelihood of the exponential, the uncorrelated exponential mixture model using two or three states, and the hidden Markov model applied to 1024 1-second duration time series of the intensity of high-resolution radar data collected at 600 samples-per-second. The solid curve is the cumulative distribution of the difference between the average log-likelihood of the best-fitting two- or three-state exponential mixture model and the exponential model; the dashed curve is the cumulative distribution of the difference between the average log-likelihood of the best-fitting two- or three-state hidden Markov model and the exponential model; and the dash–dot curve is the cumulative distribution of the difference between the average log-likelihood of the best-fitting two- or three-state hidden Markov model and the exponential mixture model having the same number of states. For example, the average log-likelihood of the hidden Markov and the exponential mixture models exceed the average log-likelihood of the exponential model by more than 0.1 for approximately 71 percent and 50 percent of the time series evaluated, respectively, and the average log-likelihood of the hidden Markov model exceeds that of the exponential mixture model by more than 0.1 for approximately 26 percent of the time series.

LOCALLY OPTIMAL DETECTION ALGORITHMS

The locally optimal Bayes detection (LOBD) statistic is equivalent (differs by a monotone transformation) to the first nonvanishing term of the Taylor approximation, at zero signal strength, of the likelihood ratio [11,18]. The LOBD statistic for a discrete zero-mean stochastic signal in correlated noise was derived in [26] under the assumptions that the signal and noise are independent, the probability density of the noise has continuous second-order partial derivatives, and there exists a

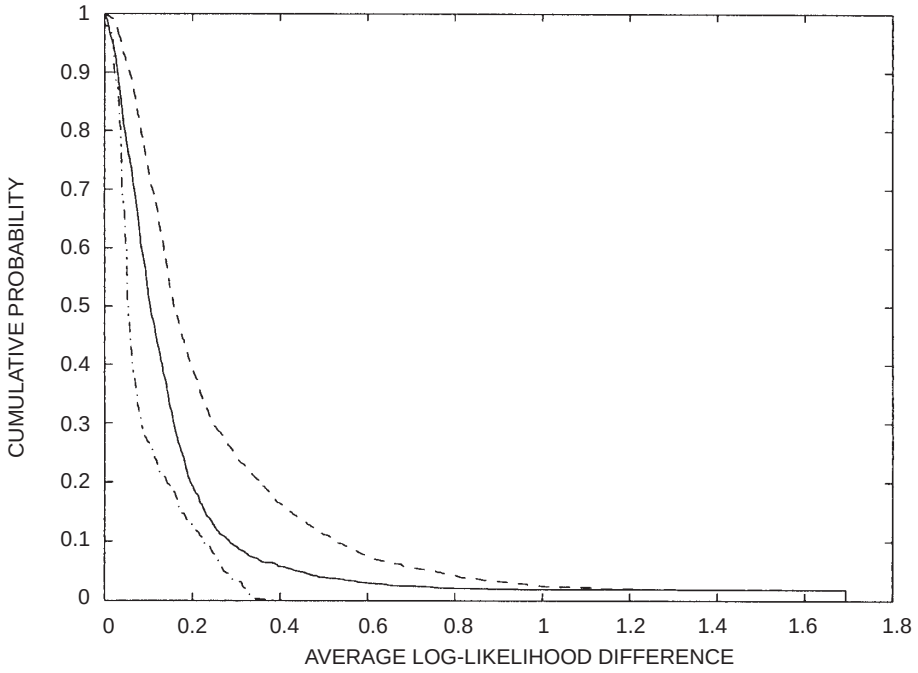

Figure 3. Complementary cumulative distributions of the difference in the average log-likelihoods of the exponential and uncorrelated mixture model (—), the exponential and the hidden Markov models (––), and the uncorrelated mixture and the hidden Markov models (– ·) applied to high-resolution radar data.

likelihood ratio. Let $x = (x_1, \ldots, x_n)$ be the vector of real-valued observations; let $p_{\mathcal{N}}$ be the probability density of the noise, and let $y = (y_1, \ldots, y_n)$ be the unit variance signal. Then the LOBD statistic is

$$LO(x) = \frac{1}{2p_{\mathcal{N}}(\vec{x})} \sum_{i,j=1}^{n} \frac{\partial^2 p_{\mathcal{N}}}{\partial x_i \partial x_j}(\vec{x}) \mathbf{E}(y_i y_j). \tag{3}$$

In [30], equation (3) is applied to HMM noise. Let $O = (o_1, \cdot, o_n)$ be the complex valued observation vector. The LOBD detector is shown to be

$$\begin{aligned} \mathcal{H}_{\mathcal{P}} &= \sum_{\ell=1}^{n} \sum_{j=1}^{m} \left(\frac{-2}{\nu_{s_j}} + \frac{|o_j|^2}{\nu_{s_j}^2}\right) p(s_\ell = j | O, \lambda) \\ &= \sum_{\ell=1}^{n} \sum_{j=1}^{m} \left[\left(\frac{-2}{\nu_{s_j}} + \frac{|o_j|^2}{\nu_{s_j}^2}\right) \frac{\alpha'_\ell(j)\beta'_\ell(j)}{\sum_{i=1}^{n} \alpha'_\ell(i)\beta'_\ell(i)}\right], \end{aligned} \tag{4}$$

where $\alpha'_\ell(j)$ and $\beta'_\ell(j)$ are the scaled forward and backward coefficients, respectively, of the hidden Markov model [20,30].

Locally optimal detectors tend to cancel signals that have sufficient amplitude to significantly affect the computation of the weighting function $p(s_\ell = j|O, \lambda)$. To mitigate this effect, the intensity, ν, of each range bin is calculated, a median noise intensity, ν_{med}, is then estimated for each range bin, and the residual, $\nu_{res} = \max(0, \nu - \rho\nu_{med})$ where $\rho > 0$ is a tuneable parameter, is added to the noise variances for purposes of calculating the conditional probabilities of the states given the data and the model parameters.

The modified LOBD detector is also applied to Gaussian mixture noise [26] and results in

$$\mathcal{M}_{\mathcal{P}}(O) = \frac{1}{2}\sum_{i=1}^{n}\sum_{k=1}^{m}\left(\frac{-2}{\nu_k} + \frac{\|o_i\|^2}{\nu_k}\right)p(k|o_i, H_0, \nu_{res}),$$

where

$$p(k|o_i, H_0, \nu_{res}) = \frac{\frac{p_k}{2\pi(\nu_k+\nu_{res})}\exp\left(-\frac{\|o_i\|^2}{2(\nu_k+\nu_{res})}\right)}{\sum_{j=1}^{m}\frac{p_k}{2\pi(\nu_j+\nu_{res})}\exp\left(-\frac{\|o_i\|^2}{2(\nu_j+\nu_{res})}\right)}. \tag{5}$$

These detection statistics are compared below with the locally optimal detector of random signals in complex Gaussian noise having zero mean and variance 2ν, which is also the likelihood ratio for the detection of Gaussian signals in Gaussian noise [18]. This statistic is equivalent to

$$\mathcal{G}_{\mathcal{P}}(O) = \sum_{\ell=1}^{n}\left(\frac{-2}{\nu} + \frac{|o_j|^2}{\nu^2}\right).$$

$\mathcal{H}_{\mathcal{P}}$ and $\mathcal{M}_{\mathcal{P}}$ are weighted sums of $\mathcal{G}_{\mathcal{P}}$s, and they reduce to $\mathcal{G}_{\mathcal{P}}$ in the case of Gaussian noise.

LIKELIHOOD RATIO DETECTORS

In [30] the likelihood ratio in HMM noise, and thus also in GM noise, is shown to be a weighted sum of conditional likelihoods. Let p_0 and p_1 be the distributions of the observation space under the noise-only and signal-plus-noise hypotheses; let O be the vector of observations; and let $\mathcal{S}$ be the set of paths of states of the Markov process. The likelihood ratio is

$$\frac{p_1(O)}{p_0(O)} = \sum_{s\in\mathcal{S}}\frac{p_1(O|s)}{p_0(O|s)}p_0(s|O). \tag{6}$$

In [30], equation (6) was applied to the case of a signal known up to a phase factor, i.e., if $Z^0 = (z_1^0, \cdots, z_n^0)$ is a known signal, then the observed signal is $Z^1 = e^{i\theta}Z^0$ where θ is unknown and assumed to have a uniform distribution on $(0, 2\pi)$. This formulation is applicable to the coherent detection of radar signals. The generalized likelihood ratio in this case is:

$$\mathcal{H}_{\mathcal{C}}(O) = \sum_{s \in \mathcal{S}} \Big[p(s) \exp(-\frac{1}{2} \sum_{j=1}^{n} \frac{|z_j^0|^2}{\nu_{s_j}}) I_0(| < Z^0, O/s > |) \Big], \tag{7}$$

where $O/s = (o_1/\nu_{s_1}, \ldots, o_n/\nu_{s_n})$, $< \cdot, \cdot >$ is the usual inner product of complex vectors, and I_0 is the modified Bessel function of order 0. In case all of the ν_j are equal, the model reduces to a Gaussian noise model, and if Z^0 is a sinusoid, equation [7] is equivalent to the Doppler processor.

The HMM-based likelihood ratio detectors, equations [6] and [7], involve the sum over all possible state sequences. In practice, one can only sum over a few such paths. The log-list Viterbi algorithm [22] was used to find the $(k + 1)^{th}$ best path given that it had already found the k^{th} best path, until a stopping criteria based on relative likelihood of the paths and a maximal number of paths was satisfied.

THRESHOLDS

The detection statistics must be compared to thresholds that correspond to a desired false alarm probability. To compute these thresholds one must know the distribution of the detection statistic in the noise-only case. A technique for computing the moments of the distribution of $\mathcal{M}_{\mathcal{P}}$ is presented in [26]. There it is also shown that if $m > 10$, the distribution of $\mathcal{M}_{\mathcal{P}}$ is approximately normal, and in the noise-only case, has zero mean. In [28], the standard deviation is calculated from the parameters and used to normalize $\mathcal{M}_{\mathcal{P}}$ so that the outputs from range bins having different parameters may be compared to a fixed normal distribution. Theoretical moments are not yet available for HMM detectors. However, the HMM model with identical parameters may be applied over blocks of data, e.g., HMM parameters are estimated for blocks of 32 range bins in the computations underlying figure 9 below, so that parameter dependent statistics, e.g., the moments of $\mathcal{H}_{\mathcal{P}}$ and $\mathcal{H}_{\mathcal{C}}$, may be estimated from the data.

ROBUST IMPLEMENTATIONS

The Gaussian mixture detector is applied in [28] to 1-second time series of successive radar pulses from fixed range bins. For these data, the parameter ν_1 is quite stable across range bins, but the other parameters of the two-state mixture density, p_1 and ν_2, fluctuate sufficiently over short distances so that estimates of these parameters from range bins near the test bin could not be used to compute $\mathcal{M}_{\mathcal{P}}$ with the test data. Parameter values from range bins near the test bin were used to define sets bounding the parameters of the test data. The signal loss attributable to parameter error was computed, and these computations were used to define order statistics of the uncertainty set that mitigate the signal loss due to parameter error. This order statistic parameter selector was compared with a minimax parameter selector. On test data, the two approaches performed similarly [28]. The multidimensional optimization performed by the minimax detector is very computationally intensive, and this approach was not practical for evaluating the algorithm on large data sets.

PERFORMANCE ANALYSIS

The performances in Gaussian mixture noise of the locally optimal Gaussian mixture detector and the power detector were compared theoretically in [26]. The distributions of $\mathcal{G}_{\mathcal{P}}$ in the case of noise-only and signal-plus-noise were computed for Gaussian signals and Gaussian mixture noise. ROCs

for this detector were computed from these distributions. The first two moments of $\mathcal{M}_{\mathcal{P}}$ were computed, and the distributions in the cases of noise-only and signal-plus-noise were approximated by the corresponding normal distributions. Signal gain is defined as $sg\ (\mathrm{dB}) = 10\log_{10}(\nu_g/\nu_s)$, where, for a fixed false alarm probability, ν_g is the signal level that $\mathcal{G}_{\mathcal{P}}$ requires to achieve the same probability of detection as $\mathcal{M}_{\mathcal{P}}$ achieves for a signal level, ν_s. Figure 4 shows that the theoretical signal gain (dB) of the two-state mixture detector over the power detector in case *n* = 65, ν_s = 0.182, probability of false alarm (PFA) = 0.001, and p_1 and ν_2/ν_1 are variable such that $p_1\nu_1 + p_2\nu_2 = 1$. As seen from the figure, theoretical signal gain ranges from 15 to 38 dB.

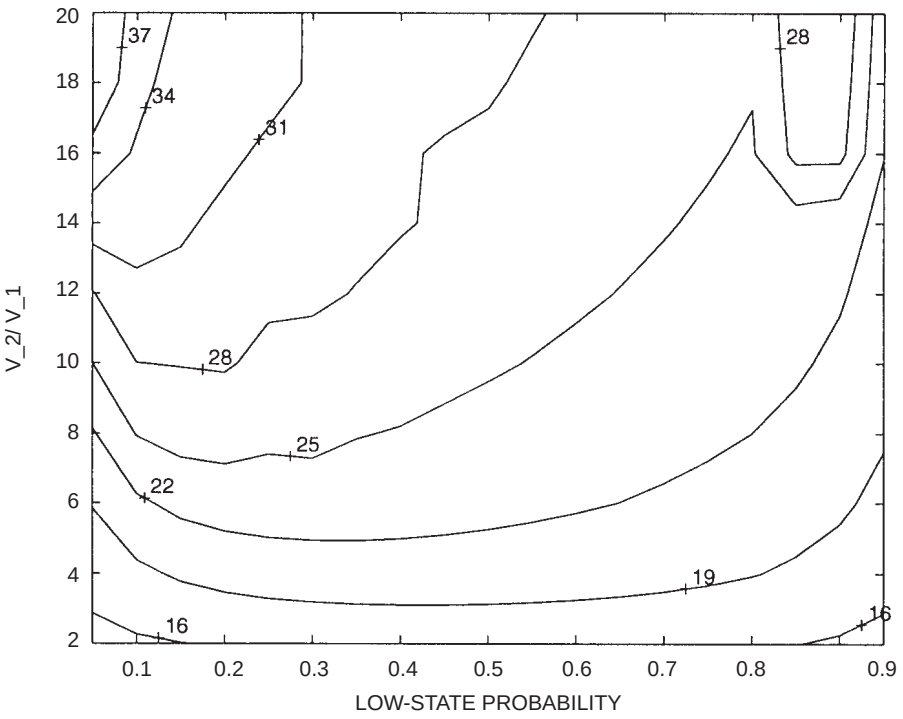

Figure 4. The signal gain (dB) of $\mathcal{M}_{\mathcal{P}}$ over $\mathcal{G}_{\mathcal{P}}$.

The performance of the above algorithms were further evaluated in [27,28,30] by using radar data. The first set of comparisons uses clutter data from 512 range bins collected at a rate of 5 pulses per second over 5 seconds to which a target was added. The intensity, or norm squared of the input data is shown in figure 5. The target starts in range bin 100 and moves at constant velocity over three bins during the 5 seconds the data are collected. The signal-to-noise ratio, using the noise intensity averaged over the 512 by 25 matrix of clutter data, is 6 dB.

Figures 6 through 9 compare the output of several processors. Figure 6 is the sum along range bins of the intensities, and is thus equivalent to the output of a fixed-threshold power detector. Note that the average intensity of the bins containing the signal is below that of the high average intensity clutter bins. CFAR processors are denoted by CFAR_x_y_z where *x* denotes the number of guard bands on either side of the test cell, *y* denotes the number of reference cells used on either side of the test cell, and *z* denotes the percentile of the noise power from the set of reference cells that is taken as the estimate of noise power for the test cell. CFAR processors using various values of *x*, *y*, and *z* were evaluated on a large data set, and the best values were *x* = 1, *y* = 2, and *z* = 100; the result from

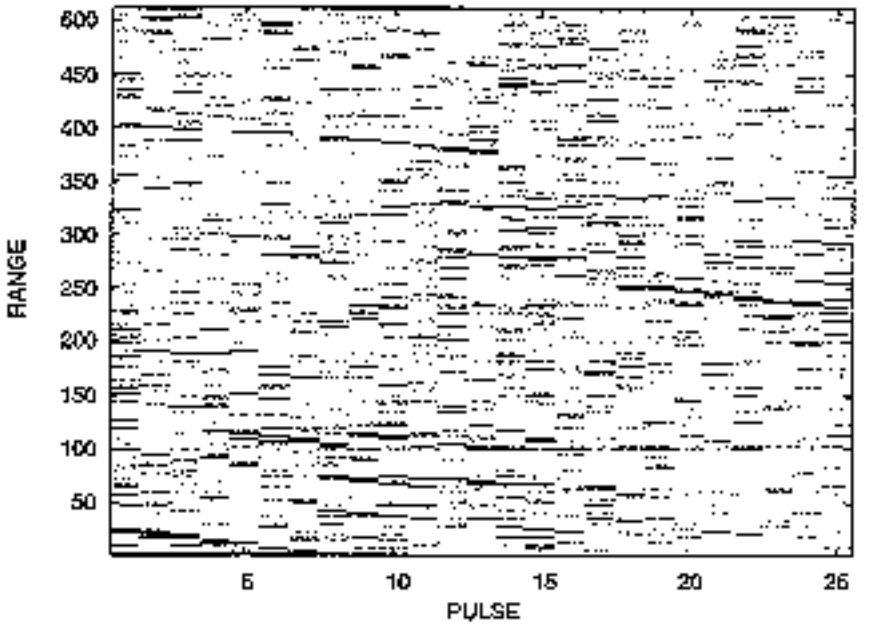

Figure 5. The intensity of the signal-plus-noise data input to the detectors evaluated in figures 6 through 9.

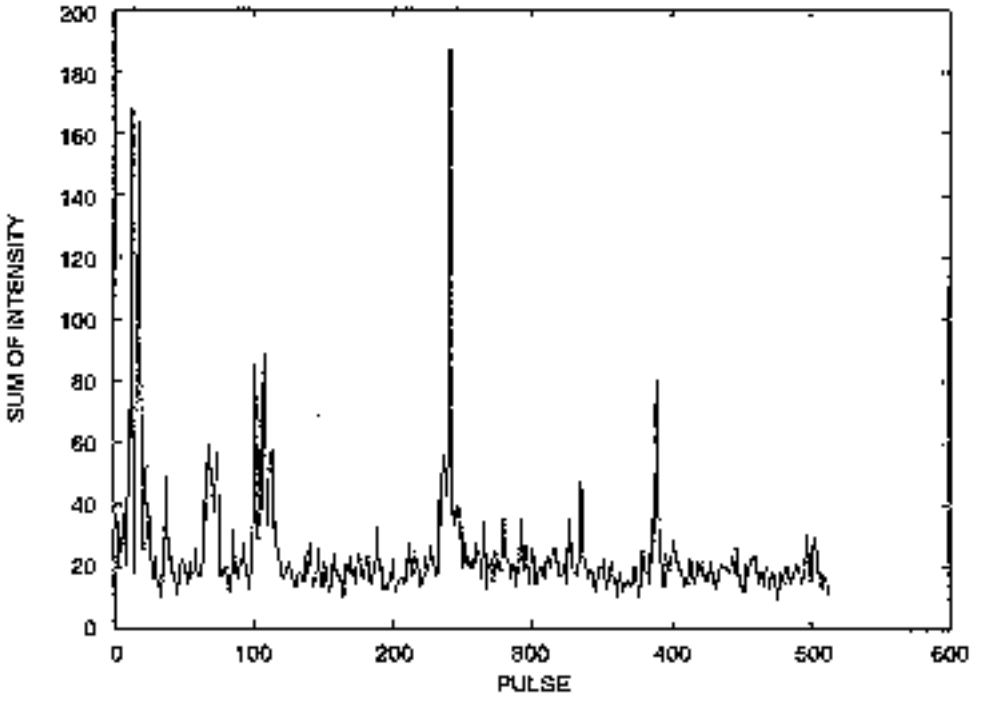

Figure 6. The fixed threshold detector on the data shown in figure 5.

applying CFAR_1_2_100 to the input in figure 5 is shown in figure 7. Figures 8 and 9 are the normalized output of the order statistic mixture detector, and the HMM detector, respectively, applied to the input in figure 5. The fixed threshold and CFAR detectors did not detect the signal without incurring a large number of false alarms, while $\mathcal{M}_{\mathcal{P}}$ and $\mathcal{H}_{\mathcal{P}}$ detected the signal without false alarms provided the thresholds were between approximately 3.5 and 5.9 or 3.9 and 9.1 standard deviations above the mean, respectively.

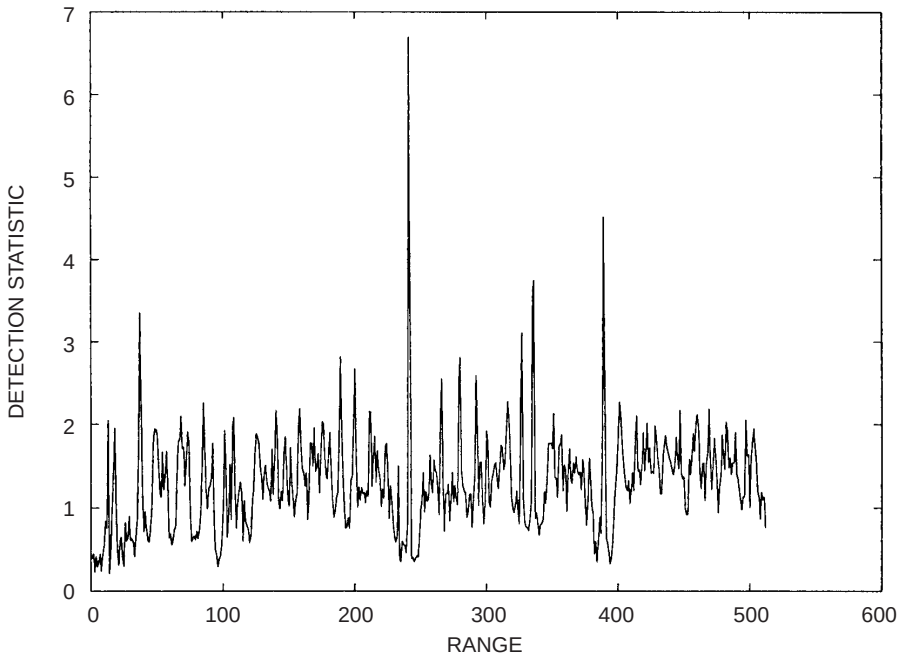

Figure 7. A CFAR processor applied to the data in figure 5.

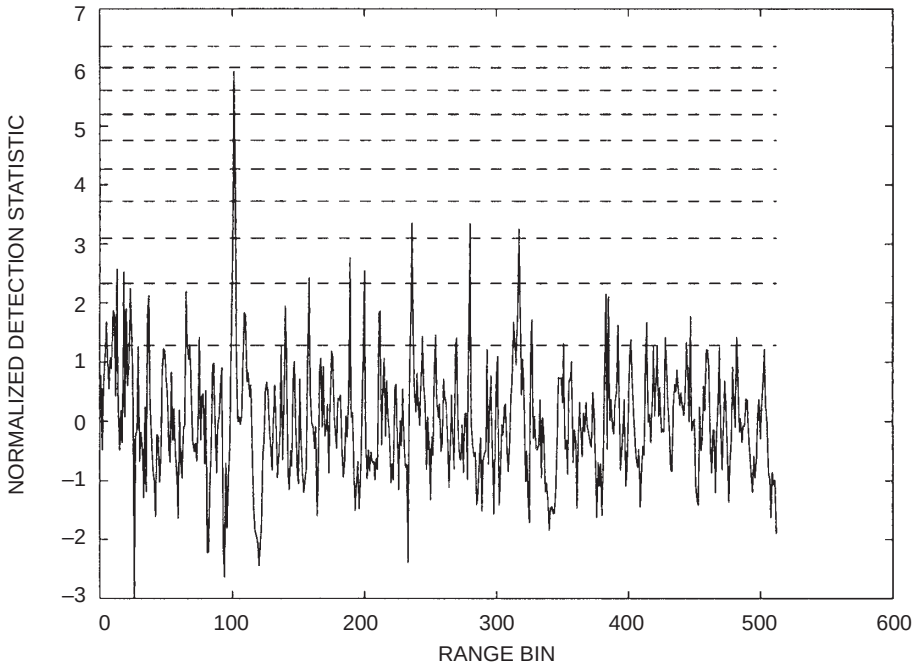

Figure 8. The OSMD applied to the data in figure 5.

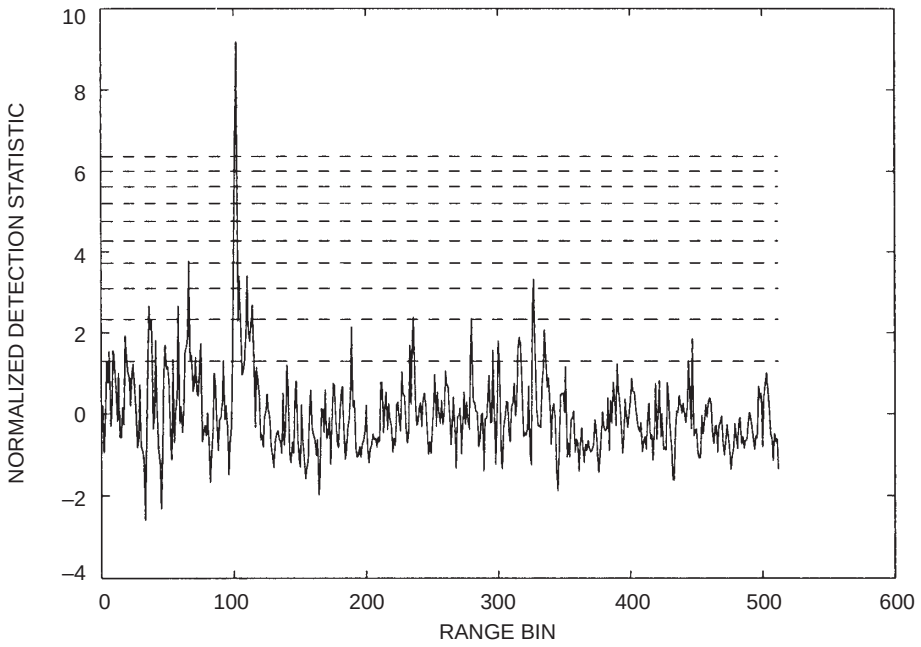

Figure 9. The HMM detector applied to the data in figure 5.

ROC curves were then developed for the CFAR and order statistic mixture dector (OSMD) processors. The noise data consisted of the 15-minute, 500-Mbyte data set described above. The signal-plus-noise data were obtained by adding, to over 20,000 randomly selected range bins, signals at SNRs of –3, 0, 3, 6, 9, and 12 dB. The noise levels were averaged over 4-second blocks of data. Figures 10 and 11 contain the ROCs of CFAR_1_2_100 and the OSMD, respectively. Comparing figures 10 and 11 indicates that the average performance improvement of the OSMD over CFAR_1_2_100, which was the best of the CFAR algorithms considered, varied, depending on PFA, and was nearly 9 dB at the lowest PFAs, approximately 10^{-5}, accessible with the 500,000 time series available for this study.

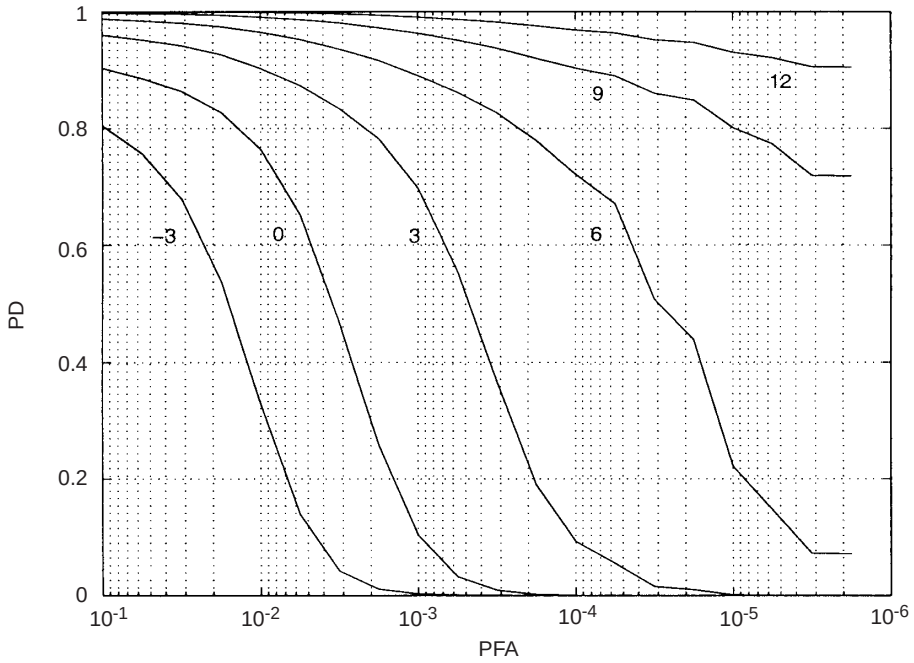

Figure 10. Empirical ROC curves for CFAR_1_2_100 using signal levels so that the average SNR over 4-second blocks of data were –3, 0, 3, 6, 9, and 12 dB applied to the high-resolution radar data modeled in figure 2.

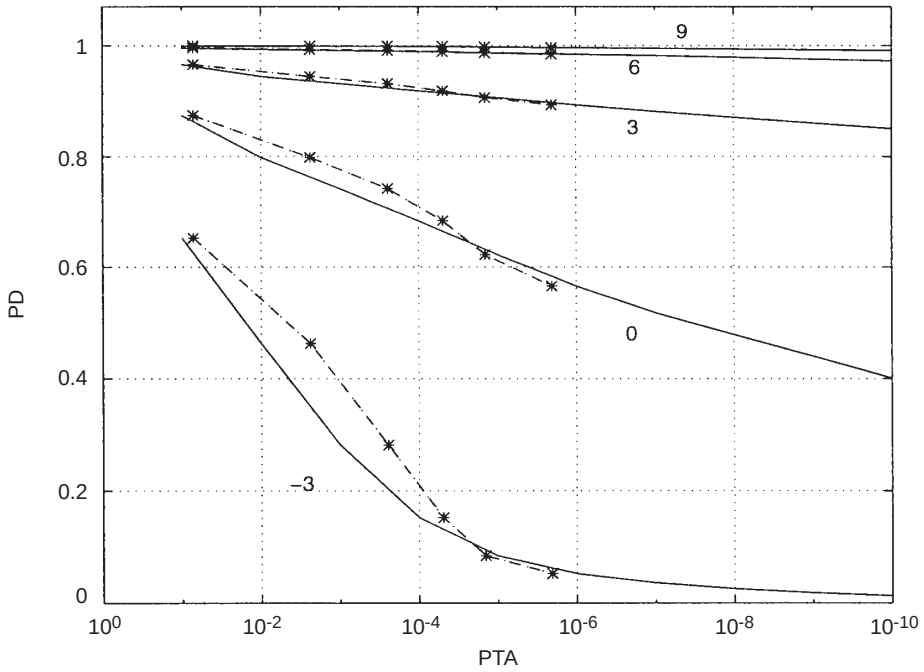

Figure 11. Empirical ROC curves for the OSMD, applied to the high-resolution radar data modeled in figure 2, using signal levels so that the average SNR over 4-second blocks of data were –3, 0, 3, 6, and 9 dB. The false alarm probability as a function of the threshold was calculated empirically and theoretically to produce the curves (***) and (—), respectively.

CONCLUSIONS

The family of Gaussian mixture probability distributions provides an approach to modeling the univariate distributions of certain types of heavily tailed non-Gaussian noise that occurs in radar and sonar surveillance systems. Approximately 70 percent of the time series in a large set of radar sea clutter were well-modeled by Gaussian densities, and nearly all of the remaining time series were well fit by two- or three-state Gaussian mixture distributions. Sea clutter has various types of correlation, and the hidden Markov models used in this study facilitate the expression of the correlation in the amplitude component of the compound probability model. Amplitude only and phase coherent detection algorithms have been derived from these noise models. Using a fixed SNR, probability of false alarm, and sample size, theoretical computations of the relative performance of the Gaussian mixture and power detectors suggest that gains of 15 to 38 dB, depending upon the mixture parameters, may be feasible. Several CFAR processors and $\mathcal{M}_{\mathcal{P}}$ were compared on a large data set, and for these data $\mathcal{M}_{\mathcal{P}}$ outperformed the best of the CFAR processors by 6 to 9 dB depending upon the PFA. The relative performance of $\mathcal{M}_{\mathcal{P}}$ and a CFAR processor on a given set of data depends upon the prevalence of high-intensity events, and the ratio of the high-intensity events to the intensity of the background. In preliminary studies, the HMM amplitude detector appears to be more promising than the Gaussian mixture detector. More extensive studies of the amplitude only and coherent HMM detectors should be conducted, and more general HMM models that incorporate correlation in the *U* component of the compound model and correlation in range as well as time should be developed as a basis for further work on signal detection in correlated non-Gaussian noise.

REFERENCES

1. Berry, L. A. 1981. “Understanding Middleton’s Canonical Formula for Class A Noise,” *IEEE Transactions on Electromagnetic Compatibility*, vol. EMC-23, (Nov), pp. 337–344.

2. Bouvet, M. and S. C. Schwartz. 1988. “Underwater Noises: Statistical Modeling, Detection, and Normalization,” *Journal of the Acoustic Society of America*, vol. 83, no. 3 (Mar), pp. 1023–1031.

3. Conte, E. and M. Longo. 1987. “On a Coherent Model for Log Normal Clutter,” vol. 134, pt. F, no. 2 (Apr), pp. 198–199.

4. Fay, F. A., J. Clarke, and R. S. Peters. 1977. “Weibull Distribution Applies to Sea Clutter,” *IEE Conference Publication 155 (Radar 77)*, pp. 101–104.

5. Feller, W. 1966. *An Introduction to Probability Theory and its Applications Vol. II*. John Wiley & Sons, Inc., New York, pp. 252–259.

6. Hawker, K. E. 1979. “A Normal Mode Theory of Acoustic Doppler Effects in the Oceanic Waveguide,” *Journal of the Acoustic Society of America*, vol. 65, pp. 675–681.

7. Jakeman, E. and R. J. A. Tough. 1988. “Non-Gaussian Models for the Statistics of Scattered Waves,” *Adv. in Physics*, vol. 37, no. 5.

8. Kassam, S. A. and H. V. Poor. 1985. “Robust Techniques for Signal Processing: A Survey,” *Proceedings of the IEEE*, vol. 73, no. 3 (Mar), pp. 433–481.

9. Machell, F. W. and C. S. Penrod. 1984. “Probability Density Functions of Ocean Acoustic Noise Processes,” *Statistical Signal Processing*, E. J. Wegman and J. G. Smith (eds.), Marcel Dekker, pp. 211–221.

10. Machell, F. W., C. S. Penrod, and G. E. Ellis. 1989. “Statistical Characteristics of Ocean Noise Processes,” *Topics in Non-Gaussian Signal Processing*, E. J. Wegman, S. C. Schwartz, and J. B. Thomas (eds.), Springer–Verlag, New York, pp. 29-57.

11. Middleton, D. 1966. “Canonically Optimum Threshold Detection,” *IEEE Transactions on Information Theory*, vol. IT-12, (Apr), pp. 230–243.

12. Middleton, D. 1967. “A Statistical Theory of Reverberation and Similar First-Order Scattered Fields,” *IEEE Transactions on Information Theory*, vol. IT-13, (Jul), pp. 372–392.

13. Middleton, D. 1967. “Statistical Physical Models of Electromagnetic Interference,” *IEEE Transactions on Electromagnetic Compatibility*, vol. EMC-19, (Aug), pp. 106–127.

14. Middleton, D. 1983. “Canonical and Quasi-Canonical Probability Models of Class A Interference,” *IEEE Transactions on Electromagnetic Compatibility*, vol. EMC-25, (May), pp. 76–106 (May).

15. Middleton, D. and A. Spaulding. 1983. “Optimum Reception in Non-Gaussian Electromagnetic Interference Environments: II Optimum and Suboptimum Threshold Signal Detection in Class A and B Noise,” National Telecommunications and Information Agency, Report 83-120, (May).

16. Middleton, D. 1984. “Threshold Detection in Non-Gaussian Interference Environments: Exposition and Interpretation of New Results for EMC Applications,” *IEEE Transactions on Electromagnetic Compatibility*, vol. EMC-26, (Feb), pp. 19–28.

17. Middleton, D. and A. D. Spaulding. 1993. “Elements of Weak Signal Detection in Non-Gaussian EMI Environments,” *Advances in Statistical Signal Processing Vol. 2*, J. B. Thomas and H. V. Poor (eds.), JAI Press, Greenwich, CT, pp. 137–215.

18. Poor, H. V. 1988. *An Introduction to Signal Detection and Estimation*, Springer–Verlag, New York.

19. Powell, D. R. and G. R. Wilson. 1989. “Class A Modeling of Ocean Acoustic Noise Sources,” *Topics in Non-Gaussian Signal Processing*, E. J. Wegman, S. C. Schwartz, and J. B. Thomas (eds.), Springer–Verlag, New York, pp. 17–28.

20. Rabiner, L. R. and B–H Juang. 1993. *Fundamentals of Speech Recognition*, Prentice Hall, Englewood Cliffs, NJ, chap. 6.

21. Sangston, K. J. and K. R. Gerlach. 1994. “Coherent Detection of Radar Targets in a Non-Gaussian Background,” *IEEE Transactions on Aerospace and Electronic Systems*, vol. AES-30, (Apr), pp. 330–340.

22. Seshadri, N. and C. W. Sundberg. 1994. “List Viterbi Decoding Algorithms with Applications,” *IEEE Transactions on Communications*, vol. 42, no. 2/3/4 (Feb/Mar/Apr), pp. 313–323.

23. Sotirin, B. J. and W. S. Hodgkiss. 1990. “Fine-Scale Measurements of the Vertical Ambient Noise Field,” *Journal of the Acoustic Society of America*, vol. 87, pp. 2052–2064.

24. Stein, D. W. J., J. W. Bond, and J. R. Zeidler. 1993. “Adaptive Locally Optimal Detection of Narrowband Signals in the Presence of Narrowband Interference,” Naval Command, Control and Ocean Surveillance Center RDT&E Division, TR 1566 (Feb), San Diego, CA.

25. Stein, D. W. J. 1995. “Statistical Characteristics of Moving Acoustic Sources in Ocean Waveguides,” *Journal of the Acoustic Society of America*, vol. 98, no. 3 (Sep), pp. 1486–1495.

26. Stein, D. W. J. 1995. “Detection of Random Signals in Gaussian Mixture Noise,” *IEEE Transactions on Information Theory*, vol. 41, no. 6 (Nov), pp. 1788–1801.

27. Stein, D. W. J. 1995. “Robust Detection of Random Signals in Exponential Mixture Noise,” 29th Asilomar Conference on Signals, Systems, and Computers, 30 October to 1 November, Asilomar, CA, pp. 1300–1304.

28. Stein, D. W. J. ____. “Robust Implementations of an Exponential Mixture Detector with Applications to Radar,” submitted to *IEE Proceedings on Radar, Sonar, and Navigation*.

29. Stein, D. W. J. ____. “Computing K-Clutter-Plus-Gauss Distributions,” submitted to the *Society on Industrial and Applied Mathematics (SIAM) Journal on Applied Mathematics*.

30. Stein, D. W. J. 1996. “Detection of Random and Sinusoidal Signals in Hidden Markov Noise,” *Proceedings of the 30th Asilomar Conference on Signals, Systems, and Computers*, 3 to 6 November, Asilomar, CA.

31. Urick, R. J. 1977. “Models for the Amplitude Fluctuations of Narrow-Band Signals and Noise in the Sea,” *Journal of the Acoustic Society of America*, vol. 62, no. 4 (Oct), pp. 878–887.

32. Vastola, K. S. 1984. “Threshold Detection in Narrow-Band Non-Gaussian Noise,” *IEEE Transactions on Communications*, vol. COM-32, no. 2 (Feb).

33. Ward, K. D. 1981. “Compound Representation of High Resolution Sea Clutter,” *Electronics Letters*, vol. 17, no. 16, pp. 561–563.

34. Ward, K. D., C. J. Baker, and S. Watts. 1990. “Maritime Surveillance Radar Part 1: Radar Scattering from the Ocean Surface,” *IEEE Proceedings*, vol. 137, pt. F, (Apr), pp. 51–62.

35. Wu, C. F. J. 1983. “On the Convergence Properties of the EM Algorithm,” *The Annals of Statistics*, vol. 11, no. 1 (Jan), pp. 95–103.

ACCOMPLISHMENTS AND IMPACTS

ACCOMPLISHMENTS AND IMPACTS

Dynamics and Exchange Processes at the Bay–Ocean Boundary

Background:

This project, completed in FY 96 after 3 years of IR support, studied the importance of tidal pumping in controlling the exchange of water at the bay–ocean boundary through observations at the mouth of San Diego Bay. The observations are novel in combining the use of shipboard acoustic Doppler current measurements with a unique bay-water tracer technique to provide visualization of the exchange as well as exchange budgets. The work is important because the Navy needs to know how its activities impact the environment and must comply with federal, state, and local water-quality regulations.

Scientific Accomplishments:

1. The project results have been incorporated in the first comprehensive analysis of physical oceanography and transport in San Diego Bay and documented in a comprehensive report to the California Regional Water Quality Control Board.

2. The project has also contributed in a collaborative study with Scripps Institution of Oceanography to evaluate the exchange mechanisms that control larval transport between coastal bays and the ocean. The larval transport investigation is funded by ONR.

Technology Impacts:

1. Development of novel methods for observation. As an example, instrumentation and techniques developed under the project were used in a Naval Seas Systems Command (NAVSEA) sponsored study of mixing in the wake of Navy ships.

2. The project results were used in a collaborative effort with the Water Quality Control Board to estimate total mass loading budgets of copper and hydrocarbons to San Diego Bay. The project provided a means of estimating the flushing rates of these contaminants in various regions of the bay.

3. The project provided data for a CINCPACFLT-sponsored study of the transport and residence time of contaminated sediments in San Diego Bay.

Fleet Impact:

The improved measurement and understanding of pollution dynamics will enable the Navy to maintain necessary operations while complying with environmental regulations.

Classification of Biological Echolocation Signals

Background:

From 1989 to 1992, an IR project was supported to study echolocation signals in dolphins.

Scientific Accomplishment:

A novel network architecture, the integrator gateway network was developed to classify multiple successive echoes from targets ensonified by a dolphin's natural echolocation signal in a naturalistic environment. The inputs to the network were spectral vectors of the returning echo plus one unit representing the start of each scan. This network combined information from successive echoes returning from the same target and reset between scans of different targets. The network was trained on a small subset (4 percent) of the total set of available echoes (1335). Depending on the measure used to assess it, the network correctly classified between 90 and 93 percent of all echo trains. In contrast, a standard back-propagation network with the same number of units and variable connections as in the integrator gateway network performed with only about 63-percent accuracy in classifying echo trains. The integration model seems to provide a better account of the dolphin's performance than a decision model that does not combine information from multiple echoes. Although the integrator gateway network does not prove that dolphins similarly combine information from multiple echoes, in the absence of relevant neurophysiological evidence, it provides support for such a hypothesis. It also suggests the potential benefits to be derived for pattern recognition from combining multiple samples from the same target.

Technology Impact:

The project has transitioned to a 6.2 development effort called Alternative Mine Detection and Classification (ALTER) sponsored by ONR Code 034 under the cognizance of Ms. Nancy Harned, (703) 696–4758, harnedn@onr.navy.mil.

Fleet Impact:

The work is important to the Navy because it has the potential to enable location of buried mines in shallow waters by mimicking demonstrated capabilities of marine mammals.

Solid-State Lasers Pumped by Laser Diodes

Background:

From FY 89 to FY 90, an Independent Exploratory Development (IED) project was funded to improve solid-state laser technology. The objective was to demonstrate improved performance of solid-state lasers by using laser diodes as pump sources.

Scientific Accomplishment:

The project pursued two separate tasks: one related to Nd:YAG ring-laser technology and the other an exploration of diode-pumping in chromium-doped laser materials.

A result of the Nd:YAG ring-laser investigation was the development of a novel multiple-rod ring laser. A patent was subsequently obtained on this device.

Chromium-doped materials were studied as laser sources using visible laser diodes as pump sources. Alexandrite, a Cr-doped chrysoberyl, is a laser material that is tunable and operates over the wavelength range of 700 to 850 nm. The output from alexandrite lasers can be efficiently doubled to produce blue and ultra-violet light. A low-threshold alexandrite laser was used in conjunction with visible-light laser diodes to demonstrate, for the first time, a diode-pumped alexandrite laser. Two other Cr-doped laser materials, LiCAF and LiSAF, were also demonstrated to be usable as laser sources under diode-pumped conditions.

Technology Impacts:

1. The program transitioned to ONR sponsorship for application to submarine laser communications. This program has since been discontinued.

2. A patent resulting from this work, U.S. Patent No. 5,249,196, was licensed in December 1996 to Nidek, Inc. As part of the license agreement, Nidek filed a business plan to develop the patented technology for use in opthalmic and dermatologic surgery.

Bioluminescence

Background:

During the 1980s, IR funding was provided to conduct oceanic bioluminescence research. At that time, very little information was available on the distribution and intensity of oceanic bioluminescence.

Scientific Accomplishments:

IR funding enabled initial development of instrumentation to measure bioluminescence. This work transitioned from 1981 to 1983 to the VARIFRONT oceanography program, under the leadership of Dr. Al Zirino, Dr. Dave Lapota, Dr. Jon Losee, and Dr. Steve Lieberman, who conducted a series of cruises in different oceans to map the distribution of bioluminescence. As a result of these efforts, NRaD (formerly Naval Ocean Systems Center [NOSC]) established a reputation for excellence recognized by the Navy and the academic community. Program quality has been reflected by contributions at numerous symposia and many publications in refereed literature. The work continued under ONR sponsorship from the mid 1980s to 1990 with measurements aboard ice breakers in the Arctic and in numerous other oceanographic expeditions sponsored by various Navy laboratories. One notable program included cruises in Norwegian coastal waters in Vestfjord from 1986 to 1990 sponsored by the Naval Research Laboratory (NRL). In all, 18 expeditions were fielded from 1979 to 1993, encompassing more than 1 year at sea for Dr. Lapota.

Technology Impact:

In the early 1990s, controlled bioluminescence of marine organisms was developed for measuring toxicity of water samples. This environmental application had roots in IR and was also supported by direct ONR funding. A prototype bioluminescence system, called QwikLite, was developed. The QwikLite Bioassay System has attracted considerable attention because of Navy applications and dual-use potential.

Fleet Impacts:

Presently, QwikLite Bioluminescence Bioassay Systems are installed at the Puget Sound Naval Shipyard and Norfolk Naval Shipyard. These facilities use QwikLite to check industrial effluent before discharge into marine waters. QwikLite technology has transitioned both to the Fleet and to civilian applications. A Navy patent on the technology has been licensed to, and a Cooperative Research and Development Agreement (CRDA) has been established with, Ocean Test Equipment, Inc., of Ft. Lauderdale, FL, to develop a commercial product. The first units are expected on the market in July 1997.

A future impact of bioluminescence research is anticipated in the field of Special Warfare Operations at night. NRaD is studying bioluminescence detection thresholds to warn of swimmers or vehicles present at night in coastal waters.

Without IR funding, the developments described above would not exist, and NRaD personnel employed in ongoing research would be pursuing careers unrelated to Navy requirements.


PROJECT SUMMARIES


COMMAND AND
CONTROL

Relational Event Algebra Extensions for Uncertainty Management in C^2 Systems

Objective(s): The FY 96 work had two main objectives: First, extend the introductory work on relational event algebra, as developed in the FY 95 IR work, to a more comprehensive setting. Second, establish corresponding feasible-to-implement algorithms that have wide application to command, control and communications ($C^{3)}$ decision-making systems and to the combination of both objective-based and subjective-based evidence for data fusion. Relational event algebra, a further development of conditional event algebra, can be shown to yield directly significant quantitative improvement of information content in probability modeling for data fusion.

Accomplishment(s): During FY 96, in addition to achieving the original main goal of establishing a more rigorous basis and wider applicability for relational event algebra, an important additional accomplishment was obtained. It was shown for the first time—by both theoretical means and numerical experiments—that conditional and relational event algebra are necessary mathematical tools in the development of naturally meaningful quantitative measures of similarity and redundancy that can be applied to rules of inference and other complex events that are described through functions of probabilities.

Conditional Event Algebra (CEA) originated because of a basic omission in the standard development of probability theory and applications: namely, the lack of a sound and feasible basis for combining logically conditional expressions compatible with conditional probability evaluations [1]. Specifically, CEA is a means by which any given probability space can be extended to a larger space, so that all conditional probability expressions can be interpreted as probability evaluations of corresponding single (albeit, possibly complex) events called "conditional events." In turn, such conditional events—often interpreted in natural language as in the form "if b, then a," "if d, then c" (or "a, given b," "c, given d," etc.)—can be logically combined and evaluated probabilistically, especially for the cases where antecedents b, d, ... are not identical [1–3]. Unfortunately, at first, there appeared many choices of CEA, each possessing certain desirable properties that the others did not [3]. (In this vein, see also the recent work of Hailperin [4], pp. 258 *et passim*, citing the desirability over other approaches of a CEA developed earlier by Goodman, Nguyen & Walker [1]). However, when the larger space to which the CEA is extended is also a probability space itself, only one natural choice of CEA can be shown to exist ([2]; [3], Section 3.6). This CEA—corresponding to a legitimate probability space and denoted as Probability Space Conditional Event Algebra (PSCEA)—is based upon the construction of a countable product probability space, all of whose factor or marginal spaces are identical to the original probability space of unconditional events. In turn, PSCEA has been shown to provide direct applications to data fusion and C^3 decision-making problems [5, 6].

CEA addresses actually only a special case of a much larger class of problems: the establishment of a consistent and mathematically sound basis for events that are compatible with given numerical functions of probabilities (conditional event algebra corresponding to arithmetic divisions only). This motivated the initial development of Relational Event Algebra (REA) based upon PSCEA (see, e.g., [6]), the main thrust of the FY 95 and FY 96 work. REA treats large classes of functions

of probabilities—not just divisions as in the case of CEA—and represents probabilities of single events, called “relational events,” which also can be logically combined and evaluated by probabilities analogous to the way PSCEA does for conditional events [4]. Extending the FY 95 work on developing REA correspondences to linear multiple argument forms with possible overlapping events, various polynomial and series forms, and certain nonlinear functions, REA was expanded even further during FY 96 so that new algebraic counterparts for several classes of nonlinear functions of probabilities were obtained, especially non-integer exponentials. A number of new applications of these results was provided for data fusion and combination of evidence problems [6].

Also, during FY 96, it was explicitly demonstrated that a natural justification for the use of CEA and REA is the implementation of natural event metrics, such as the well-known probabilistic distance between events a and b, P(a+b), or the relative distance P(a+b)/P(avb), among others [6–8]. *This is because the evaluation of such metrics requires explicit knowledge of the conjunctive probability P(a&b) that CEA and REA furnish for various classes of problems when a and b are not known at first explicitly, but rather through numerical descriptions of contributing probabilities*. Thus, in the past, prior to the development of CEA, and later REA, no such metric evaluations could be utilized except for situations where a and b were explicitly known unconditional events. In [9], preliminary results have already been established so that a new single comprehensive and consistent theory can be established, based on natural event metrics, which not only encompasses both CEA and REA, but also fuzzy logic—and hence natural language description—utilizing ongoing work on the one-point random set coverage representation of fuzzy logic. Documentation of the expanded scope of REA together with numerical experiments during FY 96 will also be forthcoming [10]. See figure 1 for a general overview of this project.

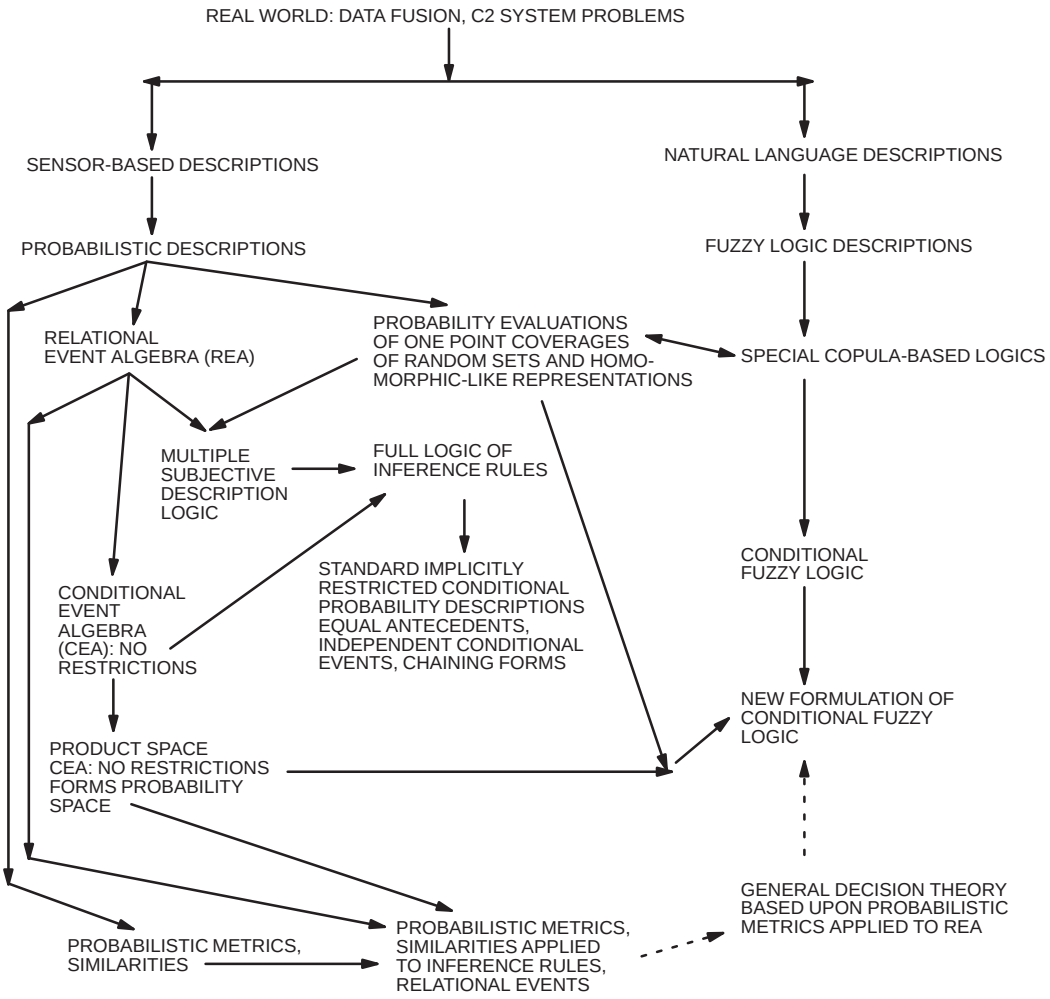

Figure 1. Relations between types of information descriptions treated in FY 96 IR Project "Relational Event Algebra Extensions for Uncertainty Management in C^2 Systems." The direction of each single-headed solid arrow is from one type of description to another that is derivable from, but not necessarily less general than the former; the solid double-headed arrow indicates equivalency; the single dotted arrow indicates projected relations based on upcoming FY 97 IR work.

REFERENCES

1. Goodman, I.R., H. T. Nguyen, and E. A. Walker. 1991. *Conditional Inference and Logic for Intelligent Systems*, North–Holland, Amsterdam.

2. Dubois, D., I. R. Goodman, and P. G. Calabrese. 1994. "Special Issue on Conditional Event Algebra," *IEEE Transactions Systems, Man & Cybernetics*, vol. 24, no. 12 (Dec).

3. Goodman, I. R. and H. T. Nguyen. 1995. "Mathematical Foundations of Conditionals and Their Probabilistic Assignments," *International Journal of Uncertainty, Fuzziness & Knowledge-Based Systems*, vol. 3, no. 3 (Sep), pp. 247–339.

4. Hailperin, T. 1996. *Sentential Probability Logic*, Lehigh University Press, Bethlehem, PA.

5. Goodman, I. R. 1995. “New Results in the Theory and Applications of Relational Event Algebra to the Combination of Evidence Problem,” *Proceedings of the First International Symposium on C^2 Research & Technology*, National Defense University, Washington, DC, (Jun), pp. 398–411.

6. Goodman, I. R., and G. F. Kramer. 1996. “Applications of Relational Event Algebra to the Development of a Decision Aid in Command & Control,” *Proceedings of the 1996 Command & Control Research & Technology Symposium*, Naval Postgraduate School, Monterey, CA, (Jun), pp. 415–435.

7. Goodman, I. R. 1996. “Similarity Measures of Events, Relational Event Algebra, and Extensions to Fuzzy Logic,” *Proceedings of the 1996 Biennial Conference of NAFIPS (North American Fuzzy Information Processing Society)*, University of California at Berkeley, (Jul), pp. 187–191.

8. Goodman, I. R. and G. F. Kramer. 1996. “Extension of Relational and Conditional Event Algebra to Random Sets with Applications to Data Fusion,” to appear in the *Proceedings of the Workshop on Applications and Theory of Random Sets*, held at the Institute for Mathematics and Its Applications, University of Minnesota at Minneapolis, (Aug).

9. Goodman, I. R. and G. F. Kramer. 1996. “Extension of Relational Event Algebra to a General Decision Making Setting,” *Proceedings of the Conference on Intelligent Systems: A Semiotic Perspective*, National Institute of Standards and Technology (NIST), 20 to 23 October, Gaithersberg, MD, vol. 1. pp. 103–108.

10. Goodman, I. R. and G. F. Kramer. “Further Extensions of Relational Event Algebra and Some Numerical Experiments,” to be submitted.

A Spherical Coordinate Algorithm for the Detection of Collisions (SCADCo) between Three-Dimensional (3-D) Objects in Computer Models

Objective(s): Develop and test an accurate and efficient algorithm for collision detection of 3-D virtual objects in real-time graphic simulations.

Accomplishment(s): The collision detection algorithm works with minimum calculation, can be made very accurate, and is independent of computer platforms, visualization software, and object format.

Collision detection can be a complicated and computationally expensive process for virtual environments and physical-simulation computer programs. Many current collision-detection algorithms that stress accuracy use Cartesian coordinates and rely either on testing for polygon intersections or attempt to solve multiple simultaneous polynomial equations to test for collisions between three-dimensional (3-D) surface patches. Less accurate, but faster, collision detection algorithms rely on bounding spheres or boxes. The Spherical Coordinate Algorithm for the Detection of Collisions (SCADCo) between 3-D computer objects uses envelopes with spherical coordinate meshes to represent the actual object in collision-detection calculations. High accuracy without invoking high computation rates is obtained by optimizing the envelope's granularity and limiting computation to nodes at angles of intersection. Four separate Application Programmer Interfaces (APIs) were developed to provide functionality: Mesh Builder API (MshBilAPI), SCADCo API, Collision Tester API (ColTstAPI), and Network Communication API (NetComAPI). Any software that has API's capability can use SCADCo.

The SCADCo design goal was to design an accurate and highly efficient collision detection algorithm. SCADCo was also designed to be independent of visualization simulation software, computer platforms, and object's format, as well as to minimize computational loading effects on the simulation's frame rate.

MshBilAPI is an automatic mesh builder program that builds the mesh using a spherical coordinate system to represent an object's surface based on radius, angle from z-axis, and angle in x-y plane. An object is "placed inside" the mesh that consists of nodes placed at fixed angular locations at radii corresponding to the object's surface. Figure 1 shows a 16-node sphere surrounding an object (cone). This mesh data will be read by SCADCo as part of the start-up sequence. The "wrapping" of the sphere onto the cone consists of tracing a ray from each node on the sphere and recording the intersects. A script file defines objects for mesh building and inputs mesh node descriptions.

The SCADCo API includes the basic mathematical routines, written in C++, interfaced to an interactive real-time, 3-D visual simulation environment on an SGI workstation. As objects in the visualization move, each collision-detectable object is enclosed by both a preprocessed envelope and a bounding sphere. The envelope defines a spherical coordinate mesh that represents the object's outer surface. A SCADCo mesh is a simple grid of points requiring less processing than a surface with tens or hundreds of polygons. SCADCo is invoked when two bounding spheres intersect. Only the nodes within the solid angles defined by these intersections are used by SCADCo for meshes-intersect determination (see figure 2). When a mesh intersects, SCADCo API sends a collision-detection signal to the simulation environment.

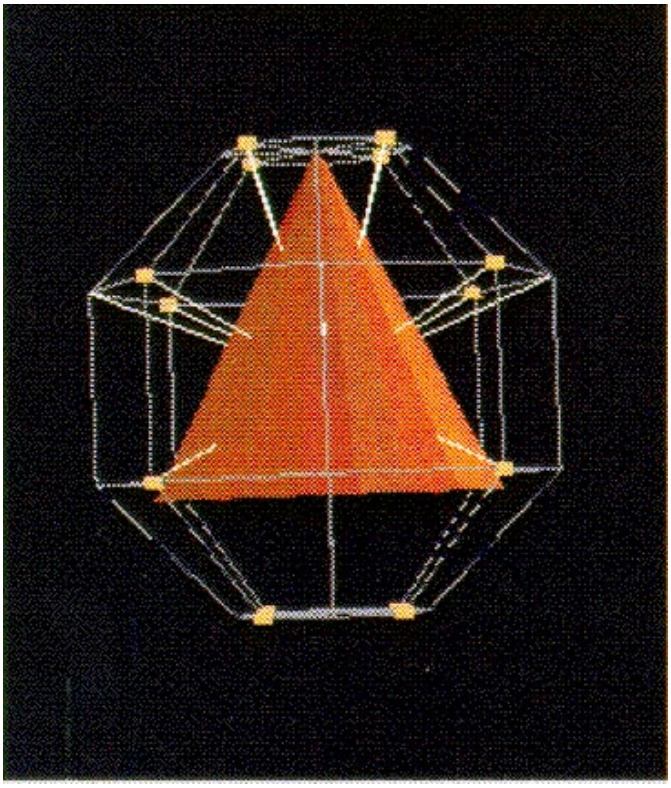

Figure 1. 16-node SCADCo sphere with cone object.

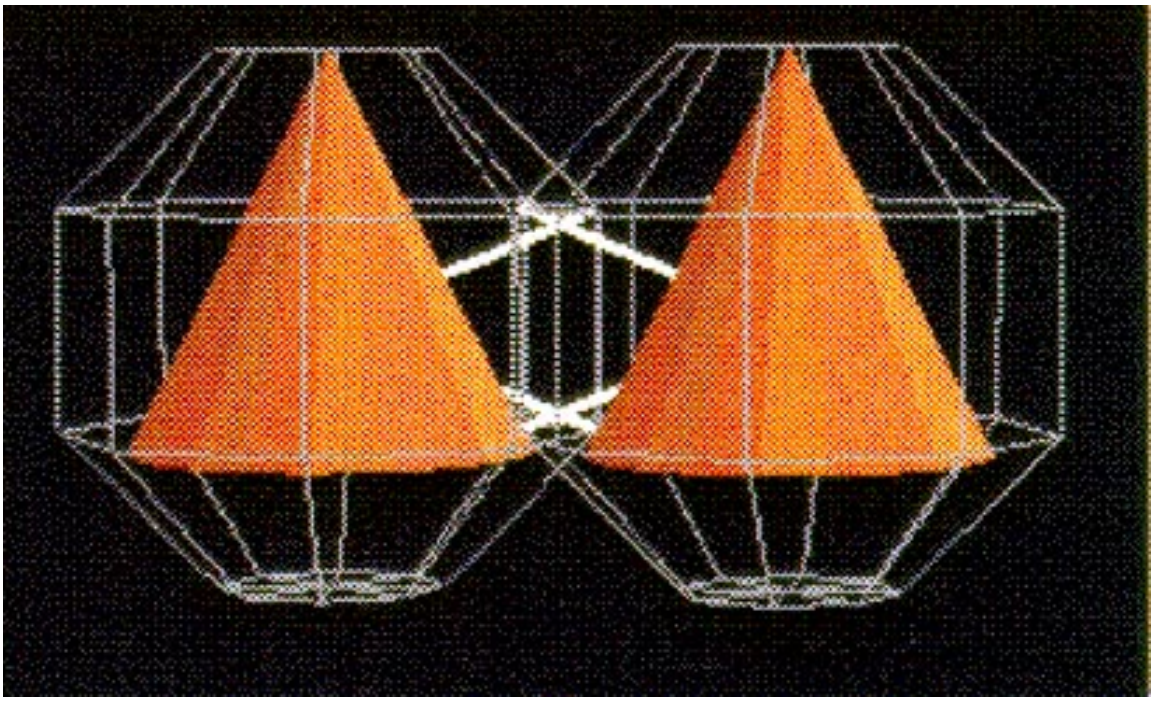

Figure 2. Two intersecting spheres showing activated nodal rays.

ColTstAPI was created using simulation software. For prototype testing, a simple visualization with two objects, one fixed and one orbiting, was created. When “hit,” the object is highlighted, indicating a collision detected by SCADCo (see figure 3 a and b).

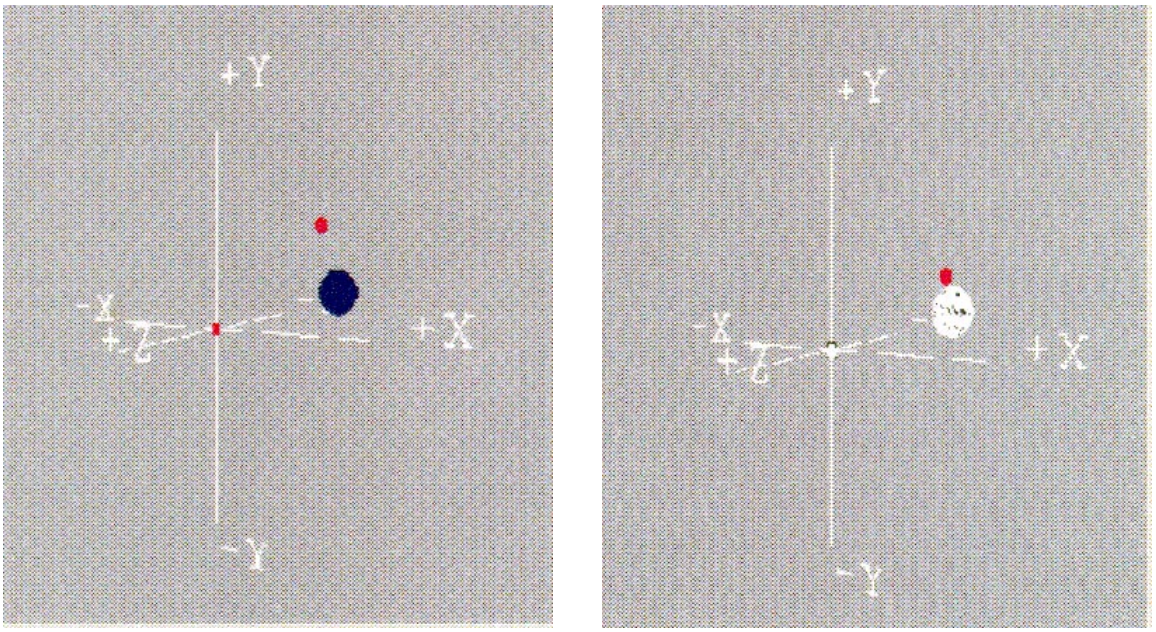

(a) *(b)*

Figure 3. Collision tester API, (a) simple two object simulation, (b) highlighted objects indicating collision detection.

NetComAPI provides communication capability between the ColTstAPI and the SCADCo API on two networked computers. NetComAPI is awakened by a ColTstAPI function call. A socket connection is made, and NetComAPI wakes up the SCADCo API. ColTstAPI sends a collision-detection object list to SCADCo API, which then reads the corresponding mesh databases. ColTstAPI obtains new object positions per frame and sends them to the SCADCo API using NetComAPI via shared memory. SCADCo checks for collision and sends results to the ColTstAPI, which responds appropriately to indicate collisions.

Techniques for Enhancing SmartNet Scheduling

Objective(s): Improve the accuracy of predicting the execution times of computational tasks in the SmartNet system to enhance its usability as a resource management system.

Accomplishment(s): Methods were added to SmartNet to account for processor loads, data dependencies between tasks, and tasks using only a percentage of a resource. These changes have contributed to the ability to apply SmartNet to the Defense Advanced Research Projects Agency's (DARPA's) Joint Task Force Advanced Technology Demonstration (ATD), the Pacific Disaster Center, the Office of the Chief of Naval Operations' (OPNAV's) Naval Simulation System, the National Aeronautics and Space Administration's (NASA's) Earth Observing System (EOS) project, and the Scalable High Performance Computing (HPC) Environment for Command, Control, Communications, Computers, and Intelligence (C^4I).

SmartNet is a scheduler for matching computational tasks (programs and data) to resources (networks and machines) to reduce the overall execution times of the tasks. Such scheduling can dramatically increase the processing capabilities of networks of machines in several ways.

1. Improved Redundancy: SmartNet allows tasks to be executed on a variety of machines rather than on a single machine specified by the user. If a machine goes down, SmartNet can reassign the tasks that were to be executed on that machine to other machines. Such a reassignment is transparent to the user.

2. Priority Consideration: Unlike academic scheduling systems that attempt to evenly balance the processing load from many users, most C^2 environments are more production-oriented and have inherent task priorities. For example, computational tasks needed for planning tomorrow's mission should be scheduled with a higher precedence than, say, daily administrative tasks. SmartNet allows each task to be assigned a priority to influence when it will be executed.

3. Accounting for Machine and Task Heterogeneity: Many tasks are optimized to execute quickly on specific machines, whereas slower versions of the program could be run on other machines if necessary. SmartNet appropriately considers the affinity of tasks to machines to obtain near-optimal assignments.

SmartNet can either act alone or as an advisor to other distributed environments. SmartNet has been integrated with Condor, Parallel Virtual Machine (PVM), IBM's LoadLeveler, Cray's Network Queing Environment (NQE), BBN's Cronus, and Corbus. A paper describing the general integration process has been written. SmartNet can globally orchestrate several computational sites, each running different underlying environments.

This work enhanced the SmartNet schedulers to consider background processor load information, sequencing constraints between tasks, and partial resource utilization. Profiling work from an FY 95 IR project identified these items as major contributors to uncertainty and inaccuracy in estimated task execution times, which in turn were negatively impacting the quality of the schedules produced by SmartNet.

To account for the effects of background processing loads, the estimated execution times of tasks are appropriately scaled prior to scheduling. Two new scheduling algorithms were developed to address data dependencies between tasks. These algorithms were novel extensions of level and clustering techniques that are well known in the scheduling literature. Finally, one of the schedulers was modified to account for partial resource utilization. Such a condition arises, for example, when a task is input/output (I/O) bound and only uses a portion of the processing resources. In such a case, it is possible to simultaneously execute another I/O bound task to efficiently use the processing resource.

Deductive Inference in a Nonmonotonic Logic

Objective(s): Two prerequisites for computers to have "common sense" are (a) relevant knowledge and (b) sophisticated logic. The goal of this project is to develop a logic that will enable computers to have the "common sense" to recognize when generalizations have exceptions and, thereby, avoid applying those generalizations "blindly."

Accomplishment(s): Starting from "first principles," a logic of generalizations was constructed. This logic can be used to recognize when a case under consideration is an exception to a generalization.

In classical logic, the conclusions inferred from premises are guaranteed to be correct. This means that it is impossible for the premises to be true and the conclusion false. However, in many situations where a human being would draw tentative conclusions that have high probability of being correct, classical logic concludes nothing because none of the potential conclusions are 100-percent certain. What is needed for use in computers is a new logic whereby conclusions need not be certain but do have high probability of being correct. Because such a logic would occasionally infer conclusions that were incorrect, it should have the property of "nonmonotonicity." This means that the logic should have the capability of retracting old conclusions when new information casts doubt on them. To accomplish this, the logic would need to be able to recognize exceptions to general rules.

Without going into technical details, the nonmonotonic logic developed in this project is based on the following idea. A *generalization* is a statement of the form "Nearly everything having property *A* also has property *B*." A *model* of such a generalization is a probability function in which the conditional probability of *B* given *A* is close to one. Implication in the logic was defined as follows. A collection of generalizations playing the role of premises *imply* a generalization playing the role of conclusion if and only if nearly every model of the premises is a model of the conclusion. This is illustrated in figure 1. Thus, if the premises are known to be correct, it is highly probable that the conclusion is correct. For that reason, any conclusions implied by the premises are said to be "probabilistically trustworthy." For the logic to have practical value, it was necessary to find a decision procedure for determining whether or not any hypothesized conclusion is implied by the premises. Such a decision procedure was successfully constructed.

It turns out that the constructed decision procedure is highly similar to Goldszmidt and Pearl's System Z^+. The significance of this is the following. Investigators in artificial intelligence and other fields have proposed a variety of nonmonotonic logics. Given the variety of proposed logics, how should one choose which one to use? It is argued here that, because we do not want to use a logic whose conclusions have a substantial probability of being incorrect, we should choose a logic whose conclusions are probabilistically trustworthy. This project has demonstrated that the conclusions from System Z^+ are probabilistically trustworthy—a fact that was not previously known.

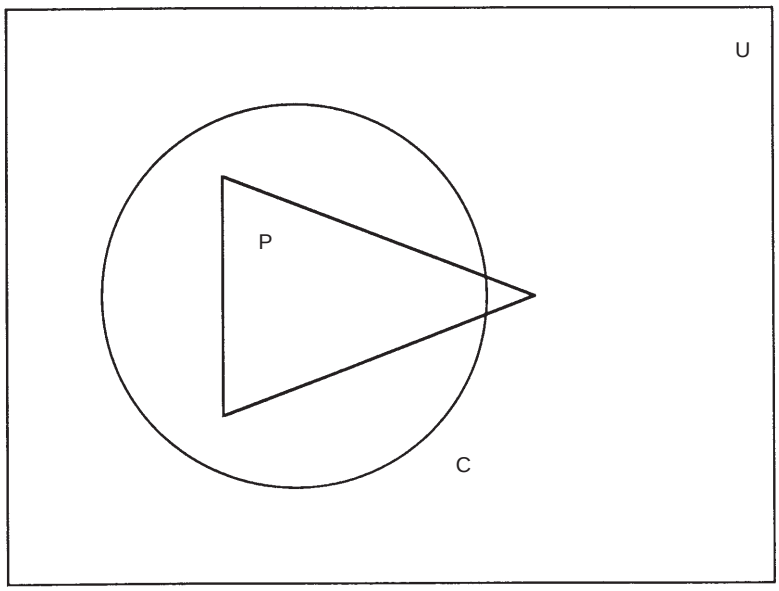

Figure 1. A Venn diagram illustrating what it means for a set of premises to imply a conclusion. The rectangle, U, is the set of all models. The triangle, P, is the set of models in which the premises are true. The circle, C, is the set of models in which the conclusion is true. The conclusion is implied by the premises because nearly every model of the premises is a model of the conclusion. Thus, in a valid implication, the conclusion has a high probability of being correct but is typically not certain to be correct.

Important Perceptual Features for Speaker Identity

Objective(s): The overall objective of this research is to determine the strongest components that affect human perception of speaker identity so that perceptual-based algorithms can be developed in the near future.

Accomplishment(s): Specifically, three of the most important features of speaker identity were identified and tested (pitch, formant frequency, and speaking rate). The relative contribution to speaker identity of these speech parameters and combinations of these particular parameters were evaluated.

In FY 96, the literature was reviewed to identify the most important feature of speaker identity. Various studies showed the importance of fundamental frequency and pitch in human perception of speakers. Perceptual experiments indicate that people cannot discriminate less than a 5-percent difference in pitch, speaking rate, and frequency scaling, taken individually, at the phrase level. Perceptual experiments also indicate that if a change is made of approximately 25 percent in pitch, speaking rate, or frequency scaling, identification cannot be made on the basis of that parameter only. The pilot study for this project indicated that repeated presentations of a speaker's voice can introduce familiarity problems and focus listeners on individual word differences and idiosyncrasies.

This basic research used software digital signal processor (DSP) tools, developed by the Speech Technology Group, for speech manipulation. The parameters of pitch, formant frequency, and speaking rate were perturbed by a collection of existing algorithms to find perceptual differences. The programmer wrote the test software and integrated this software with the DSP tools. The Speaker Identification program for comparing the results of human perceptual performance with computer identification was developed.

An experiment was conducted on human identification of speakers. In each trial, three candidate speakers and one test speaker were presented. The three candidate speakers stated the same phrase but the test speaker stated a different phrase from the candidate speakers. The subject was allowed to play the phrase for each of the candidate speakers twice only, but no restrictions were placed on the test speaker's phrase.

An $8 \times 6 \times 2$ within-subject experiment design was used. Eight speech conditions (normal, pitch, formant frequency, speaking rate, combined pitch and formant frequency, combined pitch and speaking rate, combined formant frequency and speaking rate, all factors combined) were presented to each subject. Excluding the normal condition, in each of the other conditions, the parameter(s) of the candidate speakers was perturbed within 10 percent of the test speaker (i.e., in the pitch condition, pitch was manipulated, etc.). One of the six different test speakers was presented in each speech condition. Two trials were randomly presented for each speaker in each condition, for a total of 96 trial presentations for each subject.

The results showed the parameters of pitch and formant frequency affected speaker identification. Accuracy was significantly lower for the conditions in which pitch and formant frequency were perturbed.

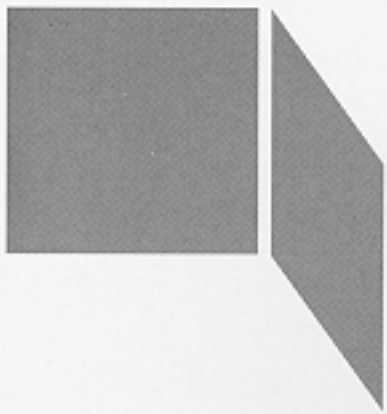

COMMUNICATIONS

Parameter Optimization for the Asynchronous Transfer Mode (ATM) Leaky Bucket Policing Algorithm

Objective(s): Develop a methodology to optimize Leaky Bucket parameters to maximize network efficiency.

Accomplishment(s): Developed tools to measure the Leaky Bucket performance subject to ON–OFF source queuing model. Demonstrated its limitations and sensitivity to the choice of the source model. Formulated a technique to optimize bandwidth and buffer requirements subject to delay and cell-loss constraints independent of Leaky Bucket.

The Leaky Bucket algorithm is a traffic-control mechanism to police users from violating their contracts during connection setup. To maximize network efficiency and control congestion, a proper dimensioning of Leaky Bucket buffer and leak rate is required. Our analysis is based on a discrete Leaky Bucket model subject to a geometrical distributed ON–OFF source model. The source model is characterized by three parameters: mean bit rate, peak rate, and burst duration. In last year's work, we developed an iterative numerical solution supported by simulations to find the cell-loss probability for a given leak rate and a bucket size. Our objective is to solve an inverse problem: Given the required quality of service (QoS), what buffer size and leak rate are required? We previously assumed the leak rate is constant. Because the Leaky Bucket leak rate is controlled by token generation, the leak rate is not constant. We revised the model slightly and developed more criteria to test the Leaky Bucket performance. The Leaky Bucket performance is very sensitive to the choice of the source model. We developed a close-form solution for the expected steady-state buffer distribution and derived performance measures to test the Leaky Bucket more thoroughly. We also developed approximate solutions for the steady-state buffer distribution using spectral decomposition criteria. We studied different scenarios including dual Leaky Bucket that has been recently standardized by ATM-Forum.

Our conclusion is the Leaky Bucket does not provide a good admission-control measure. First, the leak rate is not constant because it is controlled by the token generation period. Second, the Leaky Bucket size requirement increases drastically with the silence period. For that reason, it might fail to detect large bursts after a long silence period. Therefore, we developed a model to optimize buffer size and bandwidth independent of the Leaky Bucket and ON–OFF source. The problem we solved, given a limited bandwidth, was: Can two users with two different delay and cell-loss requirements and traffic loads share that same bandwidth? And what are the optimum buffer dimensions for those users and that bandwidth requirement? We successfully developed approximate solutions and supported our analysis with examples.

This work will greatly enhance the asynchronous transfer mode (ATM) traffic-management understanding should the Navy decide to use ATM. Also, the optimization criteria we developed for admission-control assumes a limited bandwidth that is typical of Navy systems.

H^{∞} Waves: A New Approach to Estimating Electromagnetic (EM) Fields

Objective(s): Develop an algorithm that is accurate, efficient, and robust in estimating the impedance function of an antenna from a minimal set of samples.

Accomplishment(s): Developed an algorithm that interpolates impedance data and provides a broadband estimate of the impedance function.

This project was inspired by the critical function that electromagnetic (EM) systems have on Navy ships. In the design of these ships, accurate modeling of radar and communication systems reduces cost and increases efficiency. An essential component of these systems is the antenna. The fundamental characteristics of an antenna are its impedance and its radiation pattern. How these characteristics vary with frequency is crucial to analyzing the performance of the antenna. Computing these attributes over frequency bands of interests can be prohibitively expensive. Antenna designers would welcome a method that would allow them to estimate the antenna's impedance from a minimal set of computed or measured samples. The goal of this project was to develop such a method.

Our approach was motivated by the conviction that any scheme for interpolating data from a physical system must incorporate knowledge of the system. One way to incorporate knowledge of an antenna system into an estimation procedure is to select estimates from a class of functions that correspond to that system. An appropriate class of functions corresponds to the reflectance, *W,* rather than the impedance function, *Z,* of the antenna. The reflectance is given by $W = (Z - 1)/(Z + 1)$. Since the impedance is analytic with a positive real part on the right half of the complex plane, the reflectance will be bounded and analytic in the right-half plane. (Here, frequency is mapped to the imaginary axis by the Laplace transform.) The functions defined on the complex plan that are bounded and analytic in the right half are denoted by H^{∞}. Since the reflectance of an antenna is an H^{∞} function, this is the class of functions to use in constructing an estimate of the reflectance from measured data.

H^{∞} methods arose in functional analysis from the study of Hardy spaces and have found important applications in such areas as control theory and circuit design. Nehari approximation formed the basis of this project. This method computes the best approximation from H^{∞} to a continuous function defined on the imaginary axis in the supremum norm. *Our contribution was to extend this method to incorporate physical constraints from the antenna model and point constraints from the data samples*. This extension, called the *constrained Nehari method,* was encoded in MATLAB* and used to estimate the reflectance from data computed by the Numerical Electromagnetic Code (NEC) or measured at NRaD's model range.

Figure 1 provides an example of the estimate resulting from the constrained Nehari method. The data set was measured at NRaD's model range from a brass model of a DDG 51. The measurements represent the impedance of a 35-foot monopole antenna as part of a twin system designed to operate at frequencies between 4 and 12 MHz. The data set consisted of 401 reflectance measurements at frequencies equally spaced between 4 and 12 MHz. In the figure, the solid line is formed by interpolating between the 401 measurements with a cubic spline. The constrained Nehari method used 34 evenly spaced samples and computed the dash–dot line. The constrained Nehari interpolant captures the analyticity implied in the model but misses some of the fine structure apparent in the full

*MATLAB is a registered trademark of The Math Works, Inc.

data set. The application of this method to estimating the reflectance of an antenna can be readily improved by incorporating more insightful models of antenna performance into the choice of physical constraints. It is this flexibility in the choice of constraints that will allow for the wide variety of applications of this method.

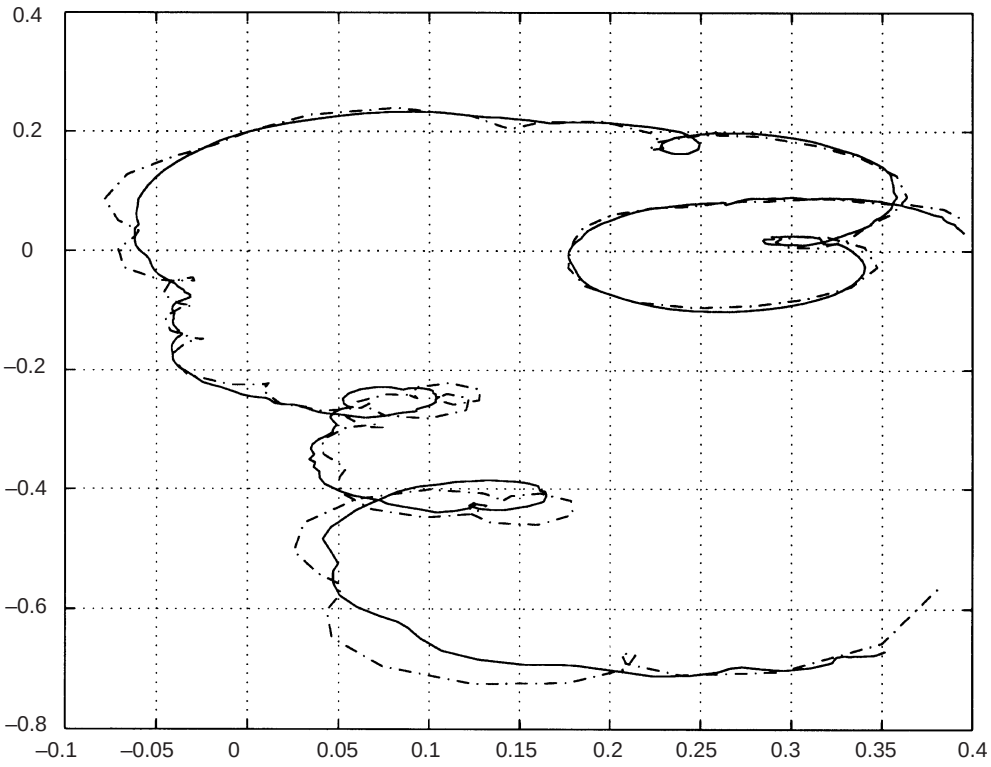

Figure 1. Estimate resulting from the constrained Nehari method.

Routing for Asynchronous Transfer Mode (ATM) Networks

Objective(s): Design and evaluate point-to-point routing algorithms for Asynchronous Transfer Mode (ATM) networks.

Accomplishment(s): Formulated a novel ATM routing algorithm based on the concept of equivalent bandwidth. Simulation studies showed that the algorithm yields good performance in terms of its simplicity, the degree of statistical gain achieved, and its low frequency of mistakes.

Asynchronous Transfer Mode (ATM) is a high-speed, packet-switched network. Even though packet-switched networks have been in existence since the 1960s, much of the insight gained in routing in low-speed networks cannot be used for routing in an ATM network because the environments under which the two types of packet-switching networks are expected to operate are quite different. Routing in a low-speed, packet-switched network is achieved through backward learning. In backward learning, congestion information is exchanged among switching nodes so that each node has some idea of the congestion in a particular region in the network. Routing decisions are made, typically, to avoid sending traffic through congested areas. Backward learning is effective in a low-speed environment because low-speed channels cannot clear congestion quickly. Congestion, once occurred, will persist, and congestion information exchanged among switching nodes remains valid for a relatively long period. In a high-speed network, congestion comes and goes extremely quickly because high-speed channels can clear a tremendous amount of traffic within a very short time. Further, the propagation delay experienced by a congestion packet is typically several orders of magnitude larger than the transmission time required to transmit a packet. This means that by the time a congestion package arrives at its intended destinations, the congestion that prompted the creation of the congestion packet may already be cleared. Clearly, backward learning, a reactive approach, will not work well in an ATM network. For this reason, it is conjectured that routing in an ATM network must be predictive.

Routing in ATM networks is challenging because it should be predictive, and predictive routing typically requires a great degree of foresight and insight. Also, unlike existing packet-switching networks that use best effort to deliver a user's traffic but offer no guarantee, an ATM network has the burden of meeting the conflicting objective of providing performance guarantee to each ATM connection admitted and ensuring a certain level of network efficiency. In general, the quality of service (QoS) requirement of a connection can reasonably be satisfied by artificially limiting the number of connections into a network. This may lead to inefficiency. On the other hand, letting a large number of connections into a network may lead to a more efficient use of network resources but may cause an unacceptable performance degradation to the connections. Satisfying these conflicting objectives is a difficult task.

A novel predictive routing algorithm based on the concept of equivalent bandwidth was formulated. This concept allows a simple metric to predict whether a connection can be added to a transmission channel without causing an appreciable degradation to the existing connections currently sharing the channel. Once such a metric is formulated, the next step is to find a route joining the source and destination of a connection such that each transmission channel on the route can accommodate the connection without violating the QoS requirements of all connections already in the network.

Further, the route can be determined recursively by properly defining the distance measure over a transmission channel. The routing algorithm has two main features: first, its time complexity is linear (optimal) with respect to the number of transmission channels in the network under consideration, and, second, the updating of connection establishments and releases requires only simple addition and subtraction operations.

The performance of the algorithm was evaluated through simulation studies. For all scenarios examined so far, the algorithm did not make any mistakes, that is, it did not admit a connection into the network without satisfying its QoS requirement. Also, a moderate level of statistical gain was achieved at each transmission channel. It may be possible to achieve a higher degree of utilization, but perhaps at the cost of occasionally admitting more connections than what the resources permit. The proposed routing algorithm takes the preferred approach of limiting the number of mistakes made by admitting fewer than the optimal number of connections. On balance, however, the algorithm yields good performance. It is simple to implement; it can achieve good statistical gain at each channel; and it seems to never make mistakes.

Although predictive routing is theoretically attractive, its practicality has not been empirically verified. The most significant contribution of this project is the demonstration that the predictive approach can be a practical solution to routing in ATM networks.

BIBLIOGRAPHY

1. Cox, D. R. and H. D. Miller. 1968. *The Theory of Stochastic Processes*. John Wiley, New York.

2. Guerin, R. et al. 1991. "Equivalent Capacity and Its Applications to Bandwidth Allocation in High-Speed Networks," *IEEE Journal on Selected Areas in Communication (JSAC)*, vol. 9, no. 7 (Sep), pp. 968–981.

3. Elwalid, A. I. and D. Mitra. 1993. "Equivalent Bandwidth of General Markovian Traffic Sources and Admission Control of High-Speed Networks," *IEEE/ Association for Computing Machinery (ACM) Transactions on Networking*, vol. 1, no. 3 (Jun), pp. 329–343.

4. Kesidis, G., J. Walrand, and C.-S. Chang. 1993. "Effective Bandwidths for Multiclass Fluids and other ATM Sources," *IEEE/ACM Transaction on Networking*, vol. 1, no. 4 (Aug), pp. 424–428.

5. Kleinrock, L. 1975. *Queuing Systems, Vol. I: Theory.* John Wiley, New York.

6. Papoulis, A. 1965. *Probability, Random Variables, and Stochastic Processes*. McGraw–Hill, New York.

7. Schwartz, M. 1996. *Broadband Integrated Networks*. Prentice Hall, New Jersey.

Non-Wiener Effects in Least-Mean-Square (LMS)-Implemented Adaptive Equalizers

Objective(s): Derive techniques and expressions that access performance of single and multichannel adaptive equalization as applied to the Navy line-of-sight digital radio environment.

Accomplishment(s): Developed mathematical tools and expressions that can be used to estimate line-of-sight communication system performance based upon design parameters such as number of antennas, spatial distribution of antennas, number of equalizer filter taps, signal-to-noise ratio (SNR) and channel fading rate.

Adaptive transversal equalizers are important components of digital receivers and are primarily used to mitigate the effects of intersymbol interference in bandwidth-constrained communication channels. An additional scenario of considerable interest, particularly in the mobile communication environment, is the operation of the adaptive equalizer in the presence of an interferer [1]. The interferer may be the result of intentional hostile jamming or unintentional self-jamming.

The computationally efficient least-mean-square (LMS) adaptive algorithm often is used in the implementation of the equalizer. Due to the nonlinearity of the LMS algorithm, the optimum performance of the equalizer often is accessed analytically using the Wiener realization of the adaptive filter [1]. The efficacy of this approach is based on the argument that the LMS algorithm will result in greater mean-square-error (MSE) than the corresponding Wiener filter due to gradient noise on the adaptive filter weights. This argument is supported by traditional analysis approaches that invoke the independence assumption in which it is assumed that the current filter-weight vector is statistically independent of the current tap-data vector [2]. Then, the resulting analytical expression of the MSE of the LMS algorithm is greater than the MSE produced by the Wiener filter.

However, recently it has been reported that an LMS-implemented adaptive equalizer, operating with a temporally correlated interfer, can produce better probability-of-error performance than the corresponding Wiener filter [3]. Subsequent simulations have revealed the unexpected result that with the proper choice of the step-size parameter, the nonlinear nature of the LMS algorithm can be exploited to generate MSE that is less than the Wiener MSE. As a result, an analysis of this problem cannot invoke the independence assumption.

To analyze this behavior, we use the transfer function approach first presented by Glover [4] for adaptive noise canceling of sinusoidal interferences and later generalized by Clarkson and White [5] to include deterministic interferences of arbitrary periodic nature and interferences that are stochastic. We develop an analysis approach that generates an approximate expression of the steady-state MSE for the LMS algorithm and demonstrate how it can be modified to include the normalized LMS algorithm (NLMS). We specifically analyze equalizer performance for interference that is sinusoidal and an autoregressive process of order one (AR(1)). Our results illustrate the relationship between the performance improvement of the LMS algorithm and system parameters such as signal-to-noise ratio (SNR), equalizer length, and the step-size parameter. We use this expression of MSE to determine the optimum step-size parameter that maximizes the performance improvement.

Figure 1 represents the baseband adaptive equalizer structure considered in this work. The equalizer input is decomposed into a sum of three statistically independent components as

$$\mathbf{u}(k) = \mathrm{s}(k) + \mathbf{x}(k) + \mathbf{n}(k), \tag{1}$$

where s(k) is the communication signal, $\mathbf{x}(k)$ is the interference vector, and $\mathbf{n}(k)$ is the noise vector.

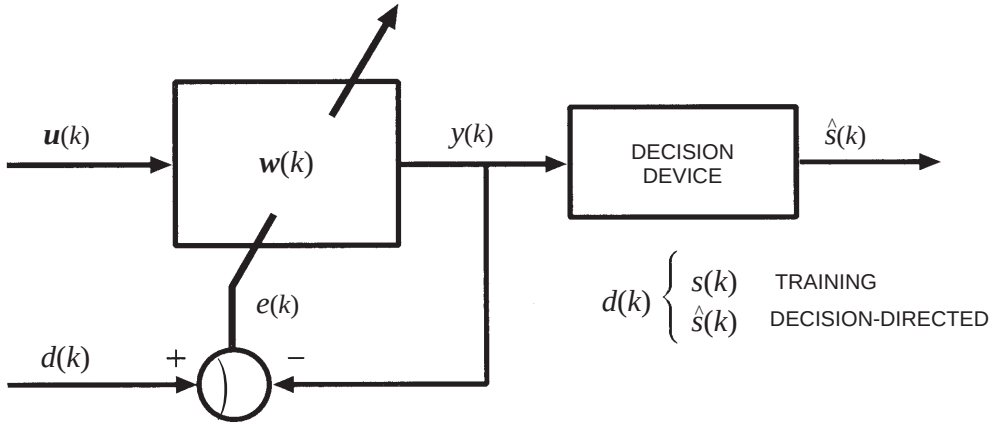

Figure 1. Adaptive equalizer structure.

We use a modification of the transfer function approach of analyzing LMS [5] to derive general expressions for the steady-state LMS and NLMS MSE. We demonstrate that an approximate analytical expression of the MSE is given by

$$J_{lms} = \frac{1}{2\pi i}\oint_{|z|=1} S_E(z)z^{-1}dz, \tag{2}$$

where $S_E(z)$ is the discrete power spectrum of the error process $e(k)$. $S_E(z)$ is determined analytically for scenarios in which the interference is a sinusoidal process and a complex AR(1) process.

As an example, figure 2 shows a plot of LMS MSE as a function of the step-size parameter η for the case in which the interference is sinusoidal. The equalizer tap length is L = 51, the SNR is 25 dB, and the signal-to-interference ratio (SIR) is –20 dB. The estimated LMS MSE obtained via simulations for the training phase and the decision-directed mode are plotted along with the theoretical approximation. Clearly, the MSE performance improvement of the LMS algorithm over the Wiener filter can be significant with the proper choice of η. Also, close agreement with theory is observed. Figure 2 is significant because it contradicts conventional wisdom in adaptive filter theory in which a smaller step-size parameter η is associated with less MSE. It can be seen that for a certain region, *increasing* η actually *decreases* MSE.

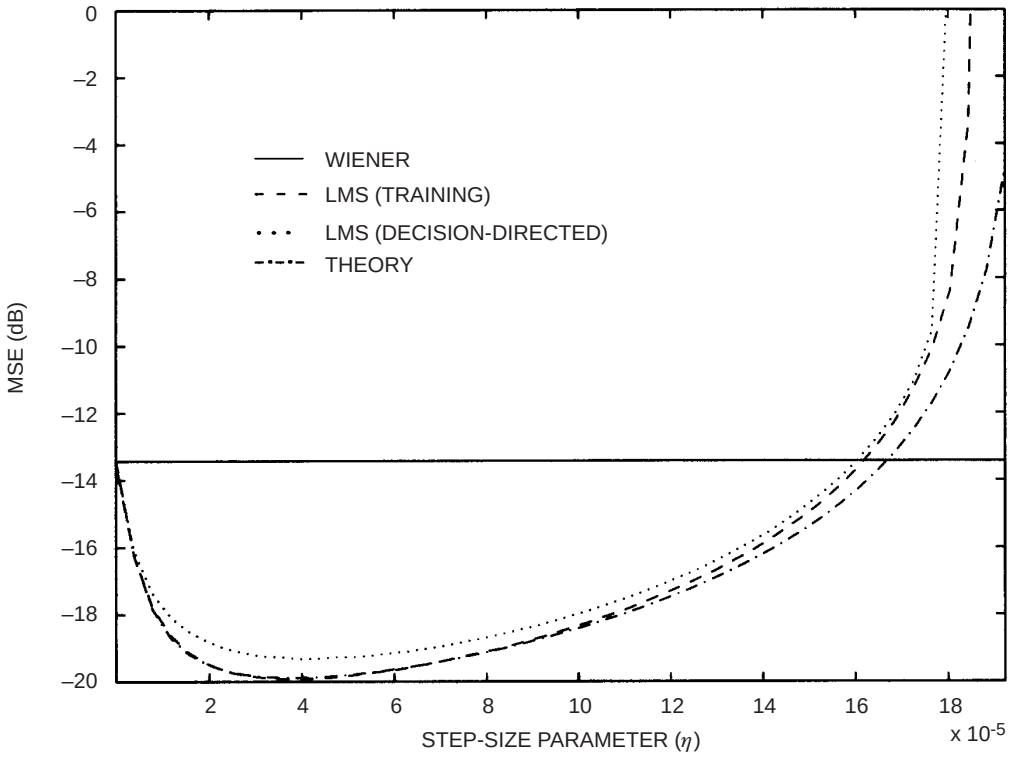

Figure 2. LMS MSE as a function of η for a sinusoidal interference, with L = 51, SNR = 25 dB, and SIR = –20 dB.

REFERENCES

1. Li, L. and L. Milstein. 1983. "Rejection of CW Interference in QPSK Systems Using Decision-Feedback Filters," *IEEE Transactions on Communications*, Com-31(4) (Apr), pp. 473–483.

2. Gardner, W. A. 1984. "Learning Characteristics of Stochastic-Gradient-Descent Algorithms: A General Study, Analysis, and Critique," *Signal Processing*, vol. 6, no. 2 (Apr), pp. 113–133.

3. North, R., R. Axford, and J. Zeidler. 1993. "The Performance of Adaptive Equalization for Digital Communications Systems Corrupted by Interference," *27th ASILOMAR Conference on Signals, Systems, and Computers*, pp. 1548–1553.

4. Glover, J. 1977. "Adaptive Noise Canceling Applied to Sinusoidal Interferences," *IEEE Transactions on Acoustics, Speech, and Signal Processing*, ASSP–25(6) (Dec), pp. 484–491.

5. Clarkson, P. M. and P. R. White. 1987. "Simplified Analysis of the LMS Adaptive Filter Using a Transfer Function Approximation," *IEEE Transactions on Acoustics, Speech, and Signal Processing*, ASSP–35(7) (Jul), pp. 987–993.

Algebraic-Geometric Error Control Coding for Improved Performance of High-Data-Rate Line-of-Sight and Satellite Naval Communications Systems

Objective(s): Develop algebraic-geometric (AG) error control coding techniques that improve the performance of high-data-rate (HDR) line-of-sight (LOS) and naval satellite communications (SATCOM) systems operating in the presence of error bursts caused by fading or pulsed radar.

Accomplishment(s): During FY 96, we identified Hermitian curves as a promising class of curves that contain the maximum possible number of points, and we analyzed the theoretical performance of AG codes based on these curves.

Error control coding is an important means of improving the performance of modern digital communications systems. In particular, Reed–Solomon (RS) codes have a number of desirable characteristics that have made them quite useful, such as a nonbinary alphabet that provides significant burst-error-correcting capability when used alone or as an outer block code concatenated with an inner convolutional code. Such concatenated systems, which may also employ interleaving and soft-decision Viterbi decoding, are used in a variety of applications, including: naval high-data-rate (HDR) line-of-sight (LOS) systems, which are subject to error bursts caused by fading or pulsed radar; National Aeronautics and Space Administration (NASA) and European Space Agency (ESA) deep-space exploration systems, where power savings are the main concern; and the satellite systems of both the International Telecommunications Satellite Organization (INTELSAT) and the European Telecommunications Satellite Organization (EUTELSAT).

The performance of concatenated systems could be enhanced by improving the performance of the outer block code. Performance of a block code, measured in terms of probability of decoding error, or coding gain, can be improved by increasing the word length relative to the size of the chosen code word alphabet. One of the undesirable restrictions of RS codes is that code word lengths are limited to the size of the alphabet. For this reason, RS codes have been generalized as algebraic-geometric (AG) codes, which allow code word lengths to be much greater than the size of the alphabet.

This generalization is based on an extension of the original RS code definition, in which code words are defined by evaluating polynomials at points on a line. In this context, it is evident that the code length of an RS code equals the number of points on a line over a finite field, and that an extension of an RS code to codes of greater length requires defining code words by evaluating rational functions at points on more complex curves that contain many more points than a line. The search for long AG codes is then a search for algebraic curves that contain many more points than a line. It has been shown that over certain fields, so-called Hermitian curves contain the maximum possible number of points, and hence AG codes based on these curves are much longer than RS codes over the same fields.

This research assesses the theoretical coding gain for Hermitian curves, that is, AG codes based on Hermitian curves, relative to RS codes over three small fields, assuming binary-phase-shift-keyed (BPSK) modulation and additive white Gaussian noise. The sample results (see figures 1 through 3) show that at bit-error probabilities of 10^{-3} and lower, positive coding gain is obtained for Hermitian codes with code rates equal to or exceeding that of the RS codes. Encoding and decoding complexity issues will be investigated in FY 97.

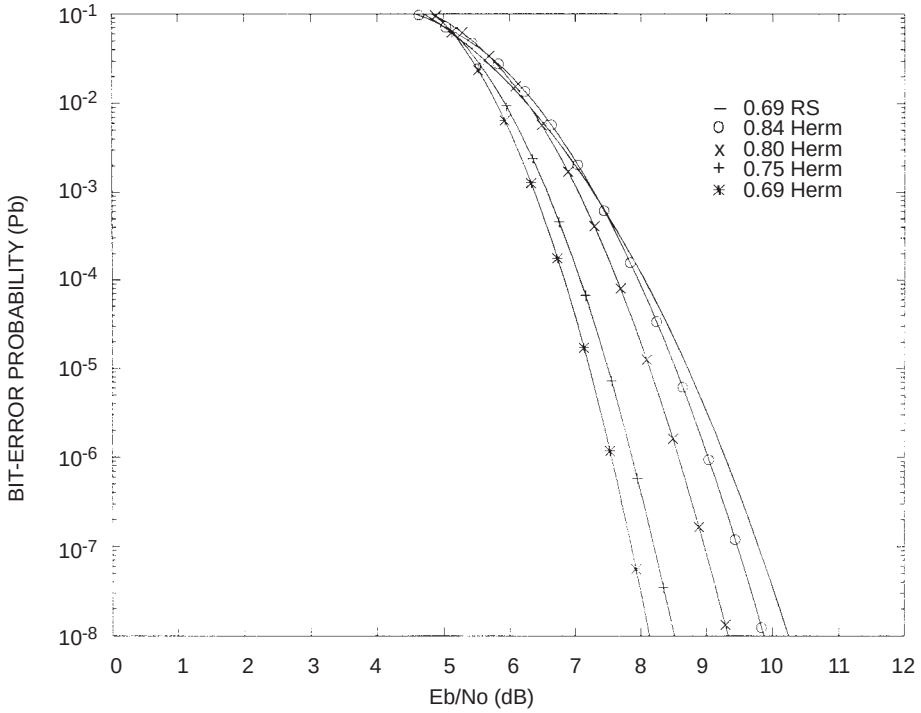

Figure 1. Bit-error probability versus SNR for low-rate RS code and selected Hermitian codes over F_{16}.

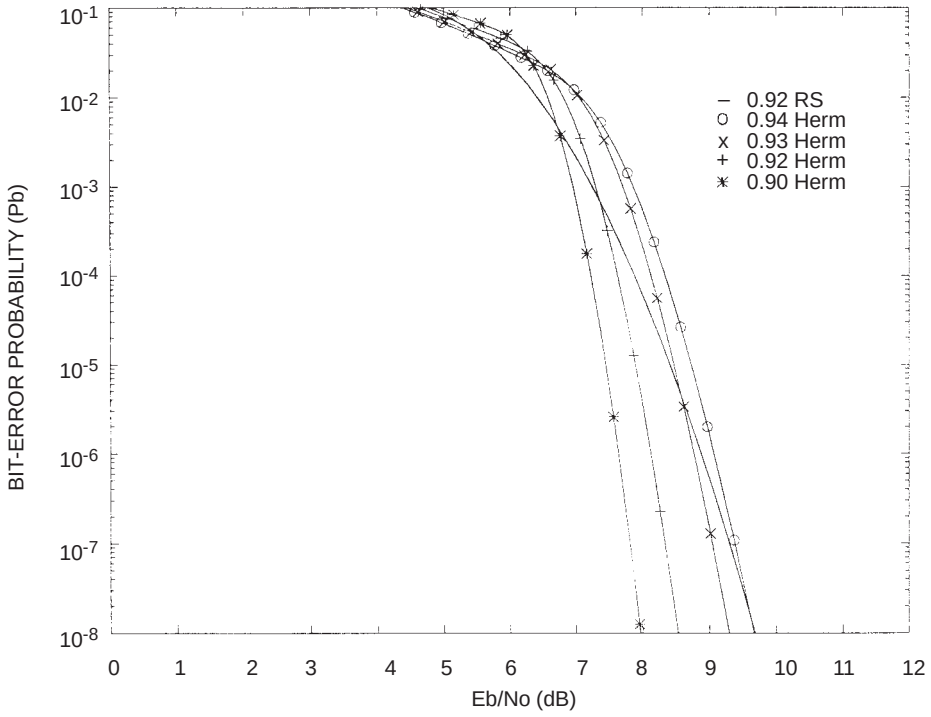

Figure 2. Bit-error probability versus SNR for low-rate RS code and selected Hermitian codes over F_{64}.

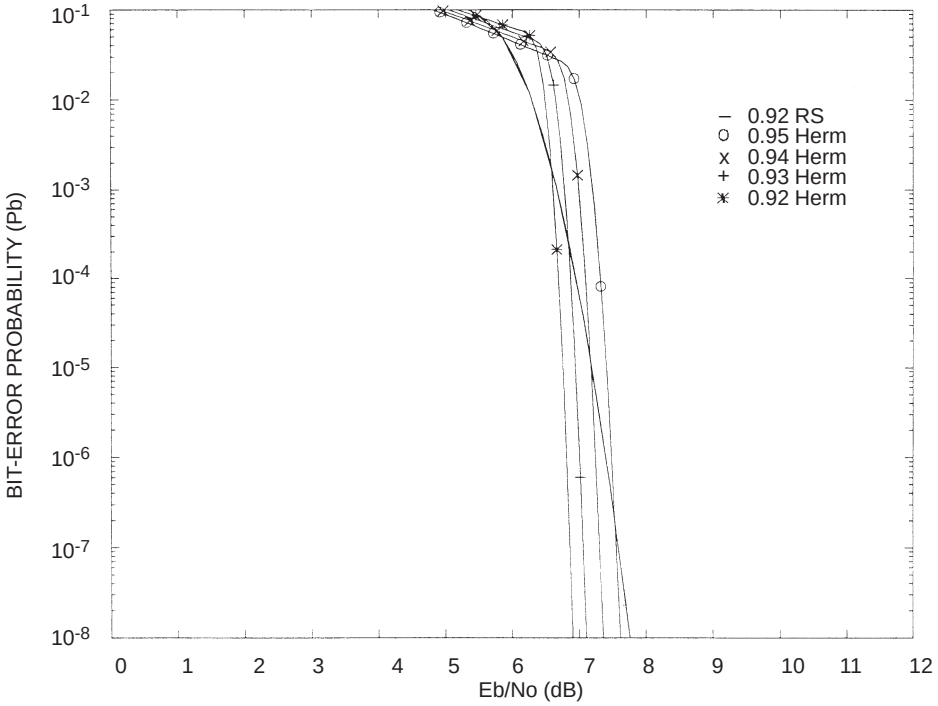

Figure 3. Bit-error probability versus SNR for low-rate RS code and selected Hermitian codes over F_{256}.

Integrated UHF Transceiver on Fully Depleted Silicon-on-Sapphire (SOS)/ Silicon-on-Insulator (SOI)

Objective(s): Integrate on a single chip the circuits required for a UHF L-band (2.4-GHz) radio transceiver to be fabricated using complementary metal-oxide semiconductor (CMOS) silicon-on-sapphire/silicon-on-insulator (SOS/SOI) technology. CMOS SOS/SOI would have the advantage of producing the entire circuit in a single monolithic technology using a relatively simple and reliable process.

Accomplishment(s): Finalized UHF subcircuit designs using transistor and passive element models developed in FY 95. Generated the reticle set necessary for circuit fabrication. Processed wafer lots to produce working subcircuits (e.g., low-noise amplifiers, mixers, transmit/receive (T/R) switches, and power amplifiers). Performed high-frequency performance testing of circuits for evaluation and comparison.

There is a general need for low-power receivers and transceivers at UHF frequencies and above. Individual transistors in fully depleted, thin-film silicon technologies have shown gain and noise performance appropriate for operation in UHF L-band and higher. Thin-film silicon-on-sapphire/ silicon-on-insulator (SOS/SOI) has price/performance advantages over both gallium arsenide (GaAs) and bulk silicon technologies. The CMOS monolithic technology available on thin-film SOS/SOI would also allow on-chip integration of additional signal-handling functions such as digital signal processing or encryption/decryption. This approach should produce the more compact receivers desired for programs such as the Defense Advanced Research Projects Agency's (DARPA's) Micro-Global Positioning System (GPS).

As mentioned above, individual transistors fabricated in NRaD's Integrated Circuit Research and Fabrication Branch have shown excellent high-frequency gain and noise performance. This project's objective was to incorporate these transistors in the design of UHF radio building block circuits (e.g., low-noise amplifiers, mixers, and power amplifiers) for performance testing. The initial system target specifications for the UHF transceiver were determined to be:

1. UHF frequency band: 2.4000 to 2.4835 GHz (ISM band)
2. Intermediate frequency: 200 to 400 MHz range
3. Low-noise amplifier noise figure target: <3.5 dB

Design studies were conducted on the UHF circuits by the University of California at San Diego (UCSD) Electrical and Computer Engineering (ECE) Department's High-Speed Electronics Group. Final designs for the subcircuits were completed in November 1995, and the data were used to generate a reticle to allow production at NRaD. The new reticle set arrived at NRaD in December 1996 and was checked for correct alignment of layers prior to use on wafer lots.

Processing of wafer lots using the new reticle began in January 1996. Since this was our first attempt to produce UHF passive elements (e.g., inductors) alongside transistors, the first lot was considered a pipe-cleaner to detect any unforeseen problems in the combined process, with the principle product's lot following a few weeks later. Several problems occurred with these lots that resulted in the first and second lots dying completely at different points in the process, and full circuits working on only

half the wafers in the third lot. The wafers in the third lot that produced full circuits also had problems. A critical step in the fabrication process is the alignment of the metal layer to the polysilicon layer to form the low-resistance T-gate structure. These layers had a designed overlap of 0.1 micron and were evidently misaligned by about this distance. This allowed some etching of the underlying polysilicon and resulted in higher than optimum gate resistance. The high-frequency performance of the transistors therefore suffered, and the number of working UHF circuits was not very high.

Several working circuits were identified and tested for performance at 2.4 GHz by the High-Speed Electronics Group at UCSD. Results on the best of these circuits were very encouraging considering the processing problems encountered. One low-noise amplifier design had a gain of 10 dB with a noise figure less than 2.5 dB at a DC power dissipation of 10 mW. A transmit/receive switch design had a 1.7-dB insertion loss with an intercept point, 3rd order (IP3) of 18 dBm. One mixer design had an IP3 of 5 dBm with a local oscillator power of 0.7 dBm (RF = 2.4 GHz, LO = 2.424 GHz, IF = 25 MHz). Although the above results were detrimentally affected by the alignment problem described previously, they still demonstrate the viability of the CMOS SOS technology for applications up to at least the 2.4-GHz frequency range. With improved equipment and processing to enhance high-frequency inductor and capacitor characteristics, operating frequencies may be extended above 10 GHz.

Additional wafer lots are currently being processed under funding from the Office of Naval Research (ONR) Microelectronics Block (Issac Lagnado) in coordination with some of the original T-gate transistor research that laid the ground work for this project. Additional refinements to the process have been introduced in an effort to improve device and circuit performance and yield.

Neural-Network-Based Adaptive Predistortion for the Linearization of Nonlinear RF Amplifiers

Objective(s): To develop signal processing that will allow the use of bandwidth-efficient modulation schemes with nonlinear amplifiers.

Accomplishment(s): Adaptive predistortion techniques have been developed for Traveling Wave Tube (TWT) amplifiers that provide performance nearly identical to linear amplifiers for bandwidth-efficient modulation techniques such as 64 Quadrature-Amplitude Modulation (QAM).

Neural-network adaptive predistortion techniques to compensate for nonlinearities in High Power Amplifiers (HPA) were investigated. The techniques developed allow bandwidth-efficient modulation schemes to be used with nonlinear HPAs with only minimal degradation in the system bit-error-rate (BER) performance. In addition, the technique adapts to changes in the nonlinearity of the HPA that could be caused by changes to the input power, carrier frequency, aging, temperature, or component replacement. Several other techniques have been applied to this problem, the most obvious being to use a linear class A HPA or to operate a nonlinear HPA sufficiently far from saturation to obtain near-linear performance. These techniques tend to require larger, heavier, more expensive, and less-efficient HPAs than necessary. Other predistortion techniques have been investigated, including analog feedback, analog feed-forward, and digital table-lookup mapping. The analog techniques have been limited by narrow operating bandwidths, extreme sensitivity to HPA variations, instabilities, and in some techniques, the requirement for additional RF amplifiers. The digital mapping techniques have been limited by the massive amount of storage required for a sufficiently accurate mapping to be stored. In addition, several digital techniques based on representing certain modulation constellations by means of signals that have (nearly) constant amplitude and have only phase variations have been proposed. These techniques can perform well with nonlinear amplifiers, but at present, seem to either provide only incremental improvements in bandwidth efficiency or require two mixers and two HPAs.

The use of neural networks was first investigated as a digital baseband predistortion technique that uses a multilayer perceptron to approximate the inverse of any amplifier response. While the neural-network predistorter was effective in reducing the effects of very general amplifier nonlinearities, it required a large number of parameters and extensive training to obtain good performance.

To reduce the complexity of the predistorter, we investigated the implementation of a neural-network adaptive predistortion technique in which the HPA nonlinearity is modeled by a general RF amplifier model, based on AM–AM and AM–PM distortion functions.

Figure 1 shows the structure of the neural-network predistorter. The neural network parameters are transferred to the predistorter after convergence and whenever significant changes in amplifier performance are detected. In this predistortion technique, the input amplitude is applied to the predistorter AM–AM function that yields the predistorted amplitude. This is then applied to the approximation of the amplifier AM–PM function, which is subtracted from the input phase value to realize the predistortion AM–PM function.

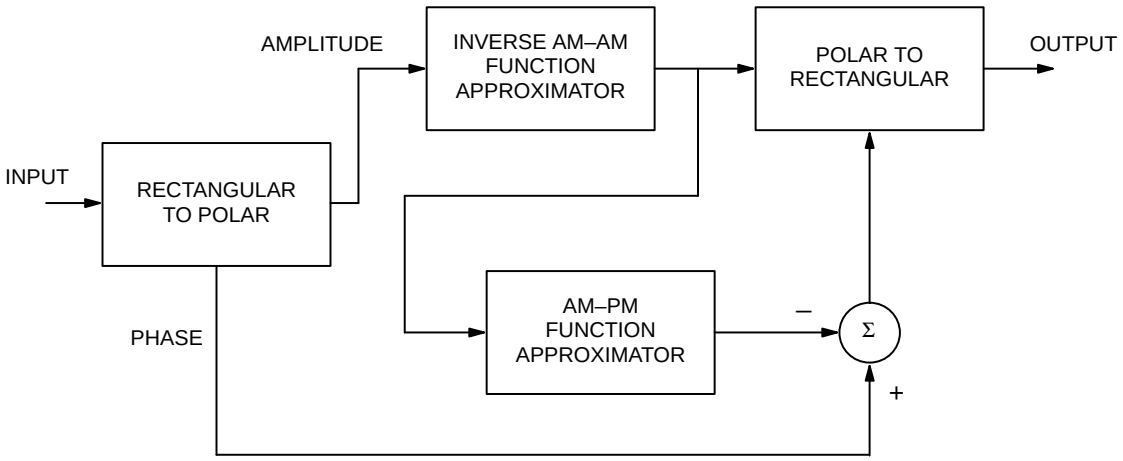

Figure 1. Model-based predistorter.

The performance of the model-based, neural-network predistorter (figure 2) was simulated by generating 100 random samples of amplifier input data and applying them to an amplifier simulator based on a TWT amplifier model. The two neural networks were trained until convergence. The model-based, neural-network predistorter was applied to the 64-Quadrature-Amplitude Modulation (QAM) symbol constellation. The predistorter eliminated the effects of the nonlinearity almost completely. The symbol error rate (SER) for the neural-network predistortion techniques are presented below. The model-based, neural-network predistorter performs almost identically to the purely linear amplifier.

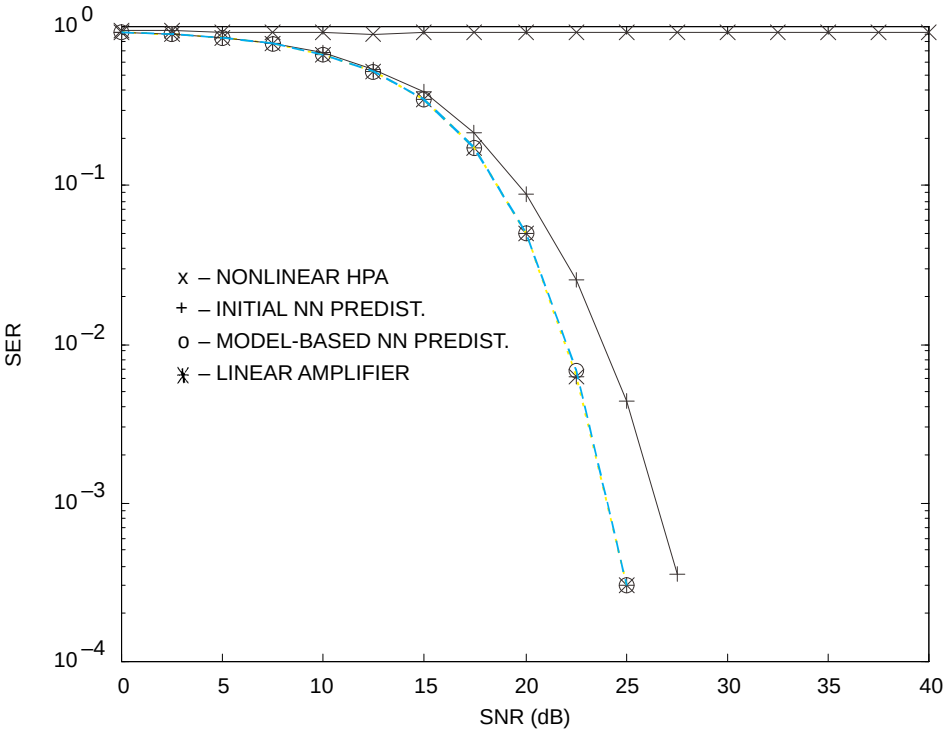

Figure 2. SER performance for 64 QAM.

The initial attempt at neural-network-based predistortion was sufficient to show the validity of using neural networks to approximate the general nonlinear functions required for predistortion. However, the initial technique required a relatively large number of parameters, which resulted in a substantial computational load. The BER performance of this technique was several dB from that obtained with a strictly linear amplifier. Utilizing knowledge of RF amplifier response properties allowed us to simplify the predistortion problem. Instead of estimating a function with complex-valued input and output, the problem was simplified to the estimation of two real-valued functions with a single common input. This resulted in a marked improvement in performance and reduced the computational effort required.

SURVEILLANCE

Correlations between Atmospheric-Turbulence-Induced Intensity Fluctuations in the Mid- and Long-Infrared (IR) Wavelength Bands for Over-Ocean Propagation Paths

Objective(s): Measure the correlation between the intensity fluctuations induced by atmospheric turbulence in the mid- and long-infrared (IR) bands for long near-sea transmission paths.

Accomplishment(s): The bichromatic correlation between the atmospheric turbulence-induced intensity fluctuations of carbon dioxide and deuterium fluoride lasers was measured for a 16-km transmission path over Chesapeake Bay.

The impact of atmospheric-turbulence-induced intensity fluctuations on the performance of electro-optical sensors is well known and has been extensively studied. A related topic that has received far less attention is the correlation between the intensity fluctuations in two or more wavelength bands. This information could be useful in exploiting the capabilities of multispectral (multiwavelength) sensors such as the Infrared Search and Track (IRS&T). Only a handful of experiments with bichromatic correlation have been performed, and almost no data exist for a long near-sea transmission path. The objective of this program was to measure the correlation between intensity fluctuations in the mid (3 to 5 microns) and long (8 to 12 microns) IR bands and compare the results to model predictions to identify limitations of the models.

During FY 95, the bichromatic correlation was measured over a 7-km path outside of San Diego Bay. For this experiment, a heater element, collimated with a 20-cm aperture Newtonian telescope, was used as source for both the mid and long IR. An identical telescope was used at the receiver. The intensity fluctuations were measured using a sandwiched mercury cadmium telluride/indium antimonide (MCT/InSb) detector (see figure 1). Since an objective of the FY 96 program was to identify model limitations, it was desirable to conduct the experiment over as wide a range of turbulence strengths as possible. The effects of atmospheric turbulence can be enhanced by operating over a longer transmission path. However, the source used in the FY 95 program was inadequate for ranges significantly greater than 7 km. To take advantage of existing Navy resources, the FY 96 experiment was performed using the Naval Research Laboratory's (NRL's) MATES (Multispectral Anti-ship Cruise Missile Tactical Electronics Warfare System) equipment.

The MATES equipment is ideally suited for this experiment since it consists of both carbon dioxide (CO_2: 9.24 microns) and deuterium fluoride (DF: 3.8 microns) lasers to provide both mid- and long-IR sources, as well as, a precision pointer and tracker to ensure proper alignment of the lasers on the receiver. The experiments were conducted on a 16-km range over Chesapeake Bay. The transmitter was located in a building at an altitude of approximately 100 ft. The NRaD receiver developed during FY 95 was located at the opposite end of the transmission path at a height of approximately 12.5 ft. The beam divergence of both lasers was 0.6 milliradians, and the lasers were operated in the transverse electromagnetic $(TEM)_{00}$ mode. The centroids of the CO_2 and the DF lasers were separated by approximately 4 cm on the beam director mirror. Measurements were made over a 4-day period during which there was great variation in atmospheric conditions.

Figure 2 shows the theoretical prediction of the bichromatic correlation coefficient as a function of the receiver aperture, based on a weak turbulence model for a uniform refractive-index-structure

Figure 1. 20-cm aperture telescope and sandwich detector.

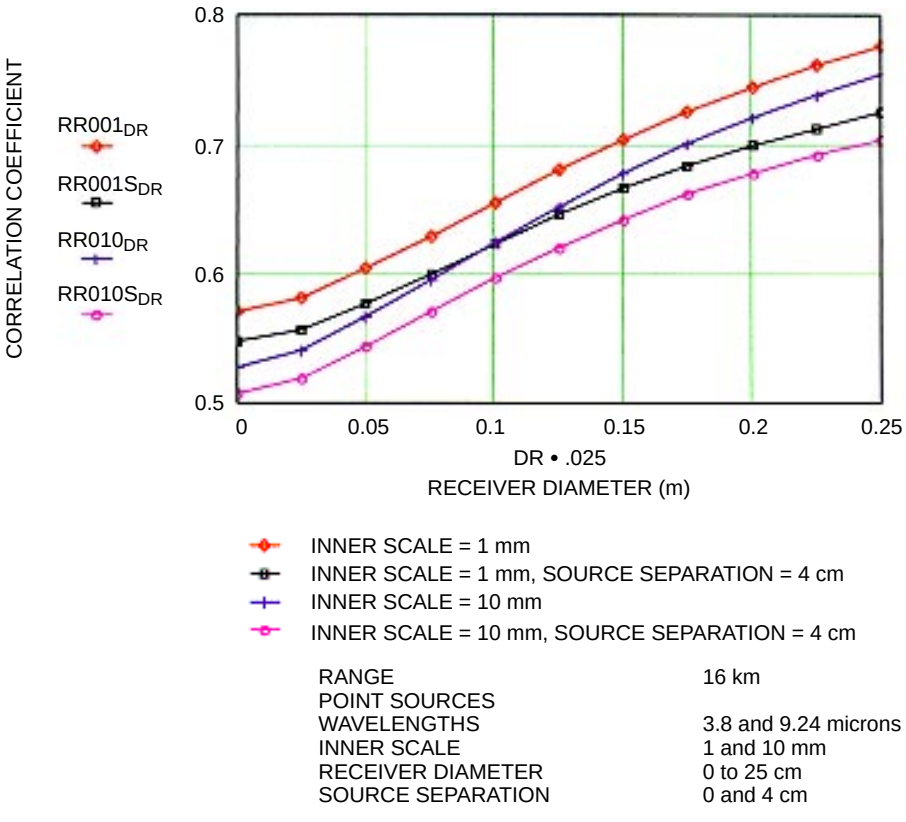

Figure 2. Bichromatic correlation as a function of receiver diameter.

constant (C_n^2). For fixed laser wavelengths, transmission range, and receiver aperture size, the correlation coefficient depends only on C_n^2 and the inner scale (l_o). The inner scale is the smallest eddy size and generally ranges from 1 to 10 mm. If C_n^2 is uniform over the transmission path, then the correlation coefficient is independent of C_n^2 and only depends on the inner scale. Figure 3 indicates that for conditions under which our experiment was performed, there should be only a slight dependence on the inner scale. The two sets of curves in figure 3 correspond to source separation of 0 and 4 cm.

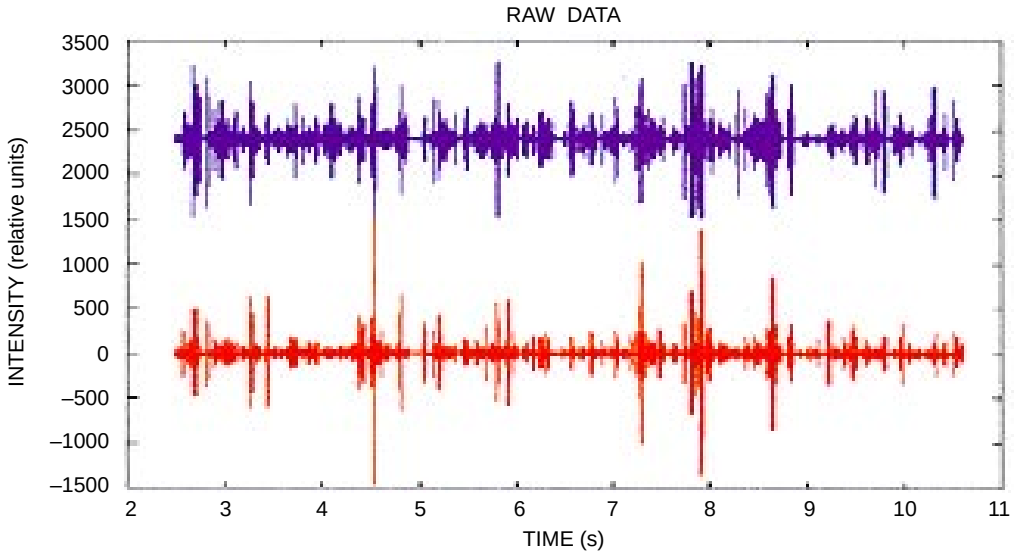

Figure 3. Raw data: red/bottom curve (CO_2), blue/top curve (DF). The separation between the curves is for viewing purposes only.

The results of the experiment were very interesting, although inconclusive. Under the strongest turbulence conditions, there was excellent agreement between our experimentally measured correlation coefficient and the theoretical prediction shown figure 2. A sample of the data is shown in figure 3. The correlation of the 8-second segment shown in figure 3 was 0.70, which is in excellent agreement with the theoretical prediction of 0.68 to 0.70. Correlation measurements taken under weaker turbulence conditions were in very poor agreement with the theoretical predictions. This is totally unexpected, since the agreement between the model and the experimental results should increase as the turbulence decreases.

The explanation for this discrepancy is still under investigation, but at this time no experimental error has been identified. Systematic errors, such as laser misalignment, that might be responsible for reducing the correlation would be more likely to occur under the stronger turbulence conditions. One possible explanation for the low correlation is that the fluctuations occurring during the weak turbulence conditions were produced in part by atmospheric processes not included in the weak turbulence model. As the strength of the turbulence increased, refractive index fluctuations could become the dominant source of fluctuations, resulting in good agreement between theory and measurements.

It is difficult to envision a process that would artificially enhance the correlation, and we are confident that we have demonstrated that, under the proper conditions, the intensity fluctuations in mid and long IR bands can be highly correlated over long transmission paths.

Fourth Cumulant Processing Study

Objective(s): Develop the basis for modification of spectrum analysis methods to include sensitivity to fourth-order moment variations.

Accomplishment(s): Experiments on measured and synthetic data sets have been run to gain experience with the methods.

A data set from a towed array was investigated using the new analysis techniques. The fourth-order moments showed strong agreement with the signal indications from the normal spectrum, but no unequivocal signals were found in the fourth-order moments that could not be found in the second-order moments.

To get more experience with the techniques, a synthetic data set with a small, high kurtosi signal was manufactured and embedded in white Gaussian noise. The plots generated show what was generally expected.

Figures 1 through 8 show data taken from a bottom-mounted array in shallow water. For this result, the data were beam-formed in the laboratory, and the beam amplitudes analyzed for second- and fourth-order moment information. Figure 1 shows the spectrum taken from a direction in which very little was happening. The solid curve shows the second-order spectrum, and the dotted curve shows the fourth-order cumulant spectrum. In general, the second- and fourth-order spectra agree with a few exceptions. The most notable exception is at approximately 457 Hz, where the fourth-order spectrum seems to show a line not seen in second-order moments. The data logs said nothing about a known 457-Hz signal, so it may have been a false alarm.

Figure 2 shows the fourth-order spectrum normalized by the second-order spectrum for the same data. An overlay with the previous plot shows nothing new except at 457 Hz.

Figures 3 and 4 show blow ups of the region from 400 Hz to 500 Hz in figures 1 and 2, respectively.

Figure 5 shows the second- and fourth-order spectra from a beam pointing in the direction of some shipping. Below 250 Hz, the second-and fourth-order spectra agree. Above 250 Hz, the fourth-order spectrum begins to show some broad-band-noise indications that the second-order plot does not see.

Figure 6 shows the ratio of the fourth-order cumulant spectrum to the second-order spectrum for the same data. As before, this indicates signals up to 500 Hz, where the second-order spectrum indicated little of interest above 250 Hz.

Figures 7 and 8 show blow-ups from figures 5 and 6. Here, the comparison with figures 3 and 4 shows what signal indications can look like.

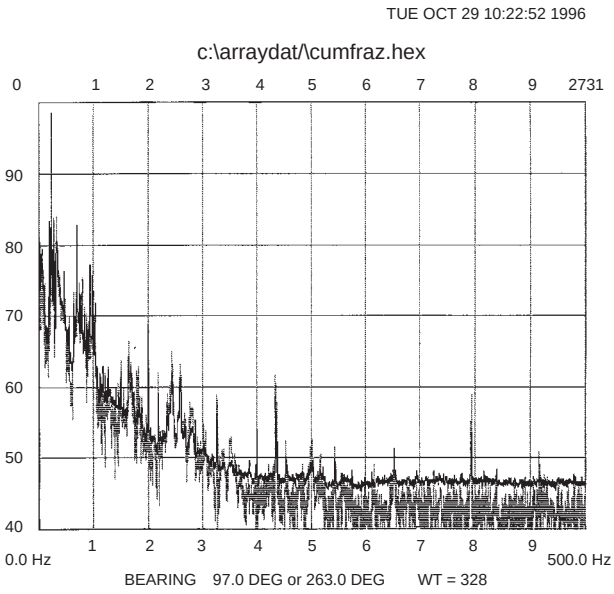

Figure 1. Spectrum and fourth cumulant for quiet beam.

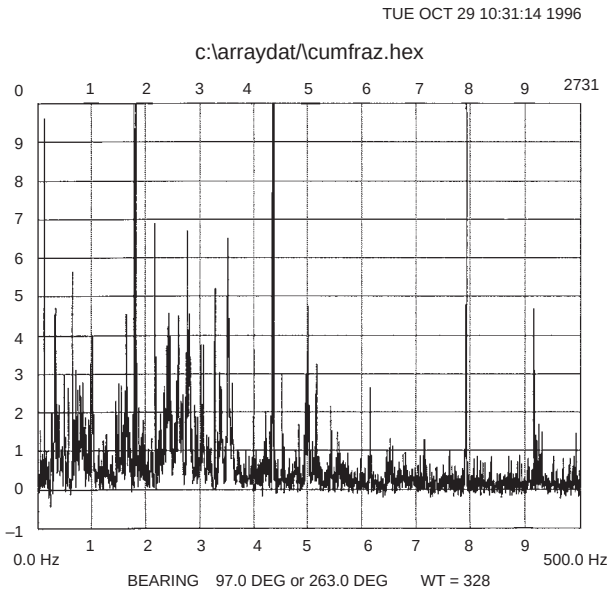

Figure 2. Normalized and fourth cumulant for quiet beam.

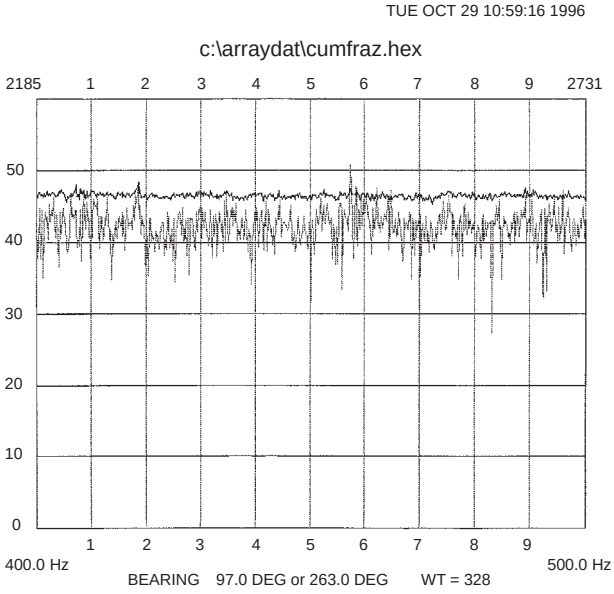

Figure 3. Spectrum and fourth cumulant for 457-Hz signal in quiet beam.

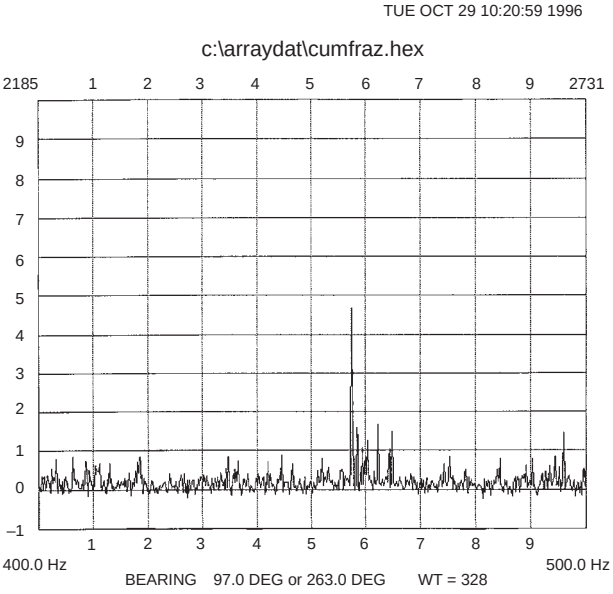

Figure 4. Normalized fourth cumulant for 457-Hz signal in quiet beam.

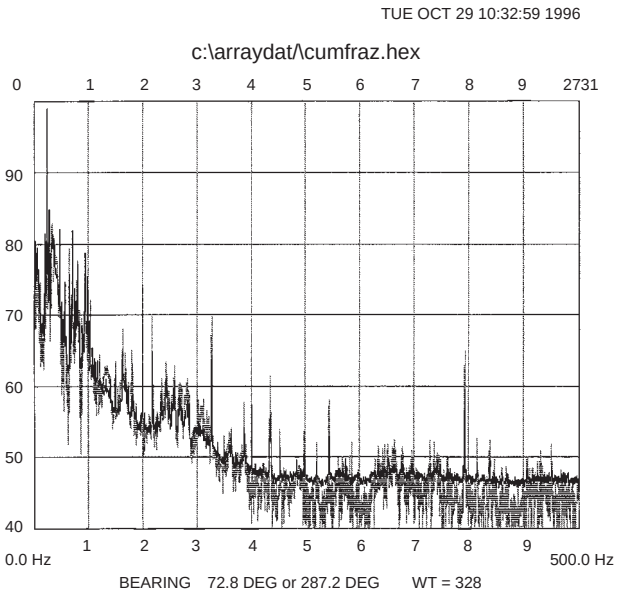

Figure 5. Spectrum and fourth cumulant for noisy beam.

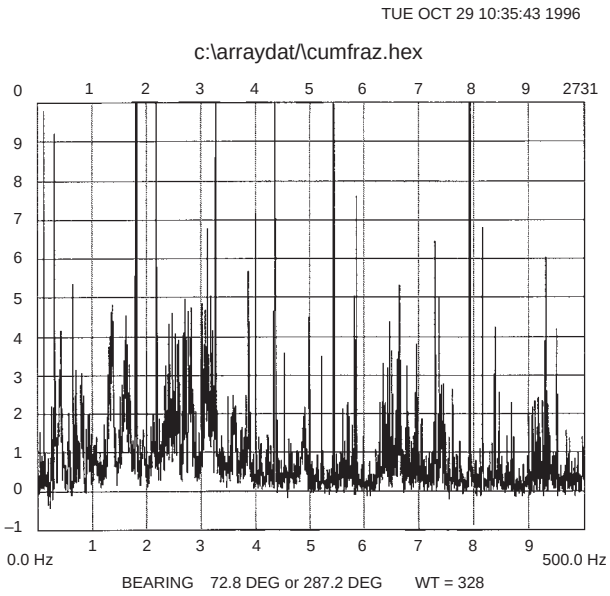

Figure 6. Normalized fourth cumulant for noisy beam.

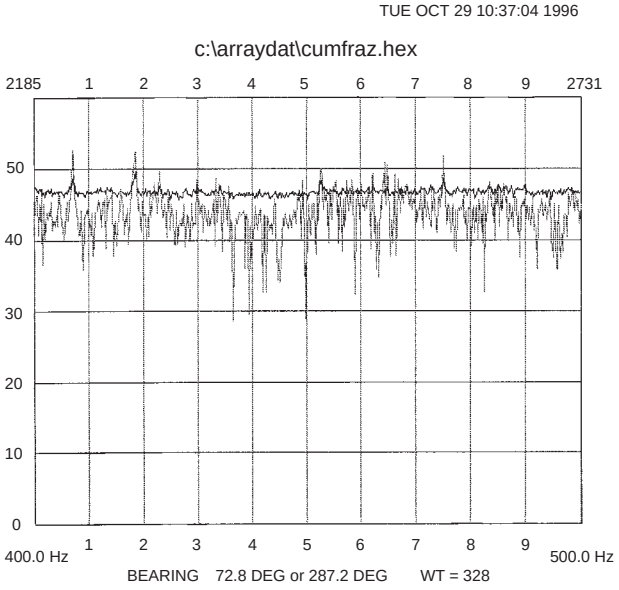

Figure 7. Spectrum and fourth cumulant for 400- to 500-Hz band in noisy beam.

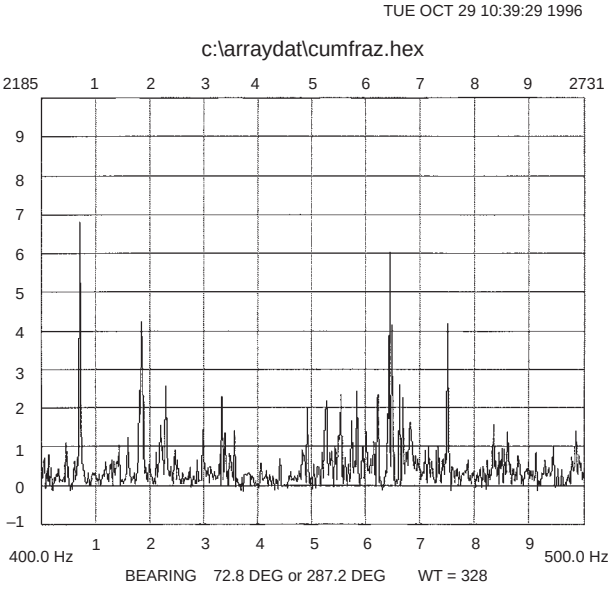

Figure 8. Normalized fourth cumulant for 400- to 500-Hz band in noisy beam.

High-Modulation-Rate Tunable Laser

Objective(s): Produce a laser diode-pumped, solid-state dye laser capable of high-modulation frequency.

Accomplishment(s): Solid-state dye laser rods made from a variety of materials were evaluated, and a 100-MHz modulated dye laser was demonstrated.

The goal of this project was to produce a laser diode-pumped, solid-state dye laser capable of high-modulation frequency. The program approach required that two major tasks be completed. The first was a demonstration of high-modulation-rate laser operation. To this end, we modified our existing, laser diode-pumped, continuous wave (cw) dye laser to demonstrate amplitude-modulated output using a modulated pump source (figure 1). By modulating the current drive to the laser diodes, we demonstrated a directly modulated laser diode-pumped dye laser that produces pulse modulation rates in excess of 100 MHz.

The second major task was to obtain solid-state dye laser gain elements that can be used in the high-repetition-rate modulated dye laser. This task had several components. One was the identification of vendors and obtaining dye laser rod samples for evaluation. The important parameters for evaluation were: dye fluorescence lifetime, spectral emission and absorption bandwidths, aging (dye depletion), fluorescence efficiency, and ability of the dye/matrix pair to produce high-repetition-rate laser output. The evaluation task led to a better defined understanding of the appropriate laser dye and solid-state host type. For example, we evaluated dye laser rods fabricated from modified plastics doped with dyes. The most promising plastic dye laser rod is composed of modified polymethyl methacrylate (PMMA). It was found that plastic dye laser rods, while excellent for low-repetition-rate operation, did not perform well at higher modulation rates. On the other hand, rhodamine 700 dye samples in glass-like substrates (ORMOSILS) perform much better at higher repetition rate. We found that the thermal and optical properties of the glasses were far superior to those of the modified polymers. This evaluation process and the dye laser resonator design task have led to the successful demonstration of a modulated all solid-state dye laser.

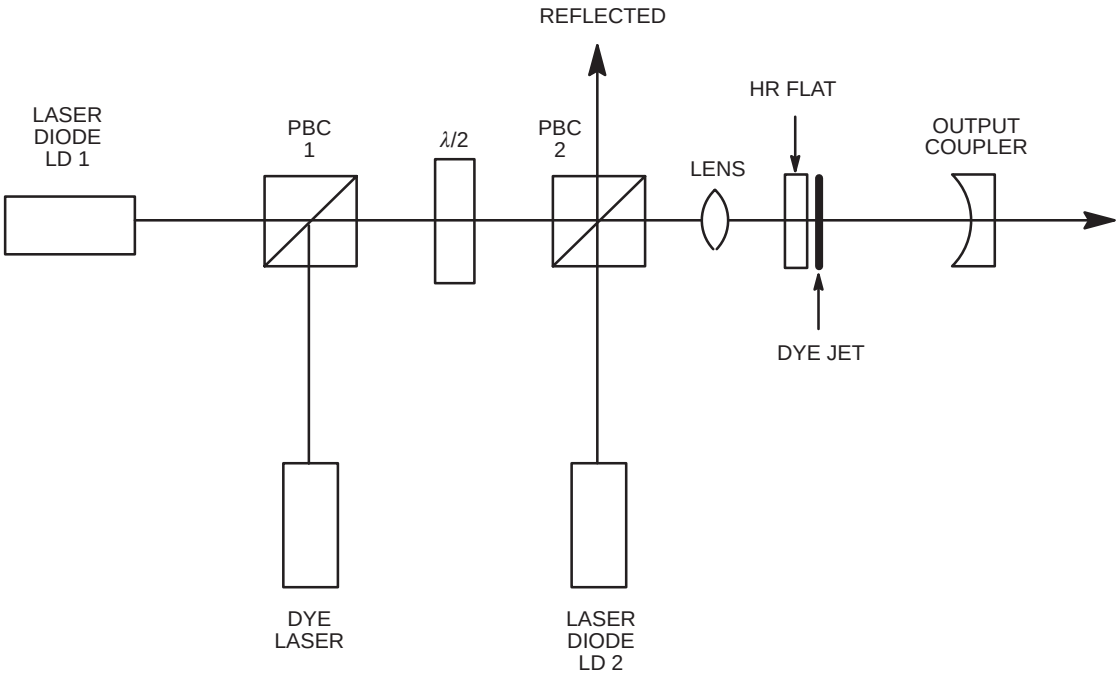

Figure 1. Pump optics and laser resonator configuration. Polarization beam combiner cubes are labeled PBC.

Super Composite Projectors

Objective(s): Experimentally validate the theoretically discovered bending-extension (b-e) coupling effect of certain composite radiator materials for potentially substantial improvements (e.g., substantial reductions in fundamental frequencies) of low-frequency, wall-driven composite projectors, such as the bender bar projector and the split cylindrical transducer.

Accomplishment(s): Planned a program of controlled experiments on b-e coupled and homogenized composite beams and split cylinders, bare or bonded to one-side with lead zirconium titanate (PZT) actuators. Contracted the experimental program to San Diego State University (SDSU) for fabricating specimens and testing to generate the experimental data needed for validation.

The objective of this 3-year research project (sponsored by ONR for FY 94 and NRaD for FY 95 and 96) was to establish the mechanical foundation for developing low-frequency, wall-driven, super-performance composite projectors that use lead zirconium titanate (PZT) or high-energy density active materials as actuators and fiber-reinforced composites with bending-extension (b-e) coupling properties as radiator materials. The technical focus was on exploring the b-e coupling properties for potentially substantial (20 to 40 percent) improvement in either resonant frequency or size reductions of the low-frequency, wall-driven composite projectors (e.g., bender bar and split [slotted] cylinder projectors currently used in mobile and deployed ocean surveillance systems). The size-reduction was particularly important to the Navy because it would reduce platform limitations and, in the case of towed sources, reduce drag limitations. It would also reduce the costs of making and operating these projectors.

As is well known, the basic acoustic radiation mechanism for all wall-driven projectors is the conversion of the extensionally actuated deformation of the actuator into the bending motion of the radiator, thereby radiating acoustic waves through water for detecting targets such as submarines. Hence, it seems beneficial to try using a radiator material with inherent b-e coupling properties, such as the N-layered regular (equal-thickness layers) antisymmetric, cross-ply laminate. For such a b-e coupled composite, the largest coupling occurs at N = 2 (two-layered, cross-ply laminate), whereas the coupling vanishes as N (even number) approaches infinity (homogenized cross-ply laminate).

In FY 94 and FY 95, we conducted exploratory theoretical studies on the (in-air) free vibration and induced-strain actuation of b-e coupled composite beams bonded to one side or both sides with actuator(s), and split cylindrical shells bonded to their concave side with an actuator. In these studies, we developed consistent classical plate and beam actuation theories for antisymmetric, cross-ply laminated beams and split cylinders bonded with actuator(s), properly accounting for the b-e coupling properties of the antisymmetric, cross-ply laminate, combined with the effects of stiffness and densities of the (relatively thick) actuator(s). We then used these theories to obtain closed-form solutions for simply supported b-e coupled composite beams and split cylinders bonded with actuator(s) and subjected to induced-strain actuation or free vibration. We concluded that substantial bending-deformation increases and fundamental frequency reductions of the composite beams and split cylinders can be achieved with graphite/epoxy; Kevlar 49/epoxy; and s-glass/epoxy, two-layered cross-ply laminates, as compared with homogenized cross-ply laminates.

In FY 96, to confirm the theoretical discoveries, we conducted experimental investigations on the static bending and free vibration of simply supported, graphite/epoxy, two-layered and homogenized cross-ply laminated beams and split cylinders. We also investigated the induced-strain actuation and free vibration of the above-mentioned beams and split cylinders bonded with a PZT actuator to one side of the beams and the concave side of the cylinders, respectively. Based on theoretical results obtained in [1, 2, 3], we planned a program of controlled experiments. San Diego State University was then contracted to fabricate the specified test specimens (P.I.: Dr. James Burns) and to conduct planned static and dynamic tests (P.I.: Dr. Chen Liang) to obtain the data required for comparisons with theoretical predictions. Unfortunately, the death of Dr. Liang caused a major setback to the project. Dr. Burns is attempting to complete the remaining contracted work in FY 97 at no additional cost to the government.

REFERENCES

1. Tang, P. Y. 1995. "Bending Deformation Increase of Bending-Extension Coupled Composite Beams Bonded with Actuator(s)," *Proceedings of the Second International Conference on Composite Engineering (ICCE/2)*, 21 to 24 August, New Orleans, LA, pp. 743–744.

2. Tang, P. Y. 1995. "Fundamental Frequency Reduction of Bending-Extension Coupled Composite Beams Bonded with Actuator(s)," *Proceedings of the Society of Engineering Science, 32nd Annual Technical Meeting*, 29 October to 1 November, New Orleans, LA, pp. 609–610.

3. Tang, P. Y. 1996. "Induced Strain Actuation of Bending-Extension Coupled Composite Split Cylinders," *Proceedings of the Society of Photo-Optical Instrumentation Engineering (SPIE) 1996 Symposium on Smart Structures and Materials*, 26 to 29 February, San Diego, CA, vol. 2715, pp. 670–681.

Active Matched-Field Tracking (AMFT)

Objective(s): Develop new method for detecting quiet submarines (i.e., diesel-electric on battery power) in shallow water.

Accomplishment(s): An algorithm has been developed that allows coherent processing over a 3- to 5-minute period of time. Realistic simulations show reliable shallow-water detection for a low-powered, inexpensive shallow-water system at a range of approximately 5 km.

Data were collected for an extended period (approximately 3 to 5 minutes in the underwater case), and a set of covariance matrices was calculated. A new set was generated at approximately 10-second intervals. The matched-field tracking (MFT) algorithm calculated the set of tracks that best corresponded to the experimental data set. The algorithm included the effects of shallow-water multipath propagation and the spectral content of possible targets.

A realistic simulation was made for a maneuvering submarine (10-dB target strength) operating in a variable depth, shallow-water environment. A solid submerged track was obtained in spite of low average transmit power (10 watts), a high ambient noise level, and interference due to three surface vessels (see figure 1).

Advantages of MFT include automatic target detections, low false-alarm rate, and good connectivity. The algorithm collects data in approximately 3-to 5-minute segments and, without operator intervention, generates a list of possible targets. Because this list includes target depth, the identification of submarines is greatly simplified. The false-alarm rate tends to be low because of the low output data rate. Obviously, a system that produces output every 5 minutes will tend to have a lower false-alarm rate than one with a 10-second output schedule. Also, connectivity is good because the low data rate simplifies the connection of the signal processor to associated data networks.

The algorithm has been sent (on request) to the Naval Undersea Warfare Center (NUWC) group that operates the Tongue of the Ocean acoustic test range. A copy of the basic matched-field tracking algorithm was sent to Professor Stewart Glegg at Florida Atlantic University. The extension of MFT to active systems, such as the Multistatic Active Capability Enhancement (MACE) Program, is under development.

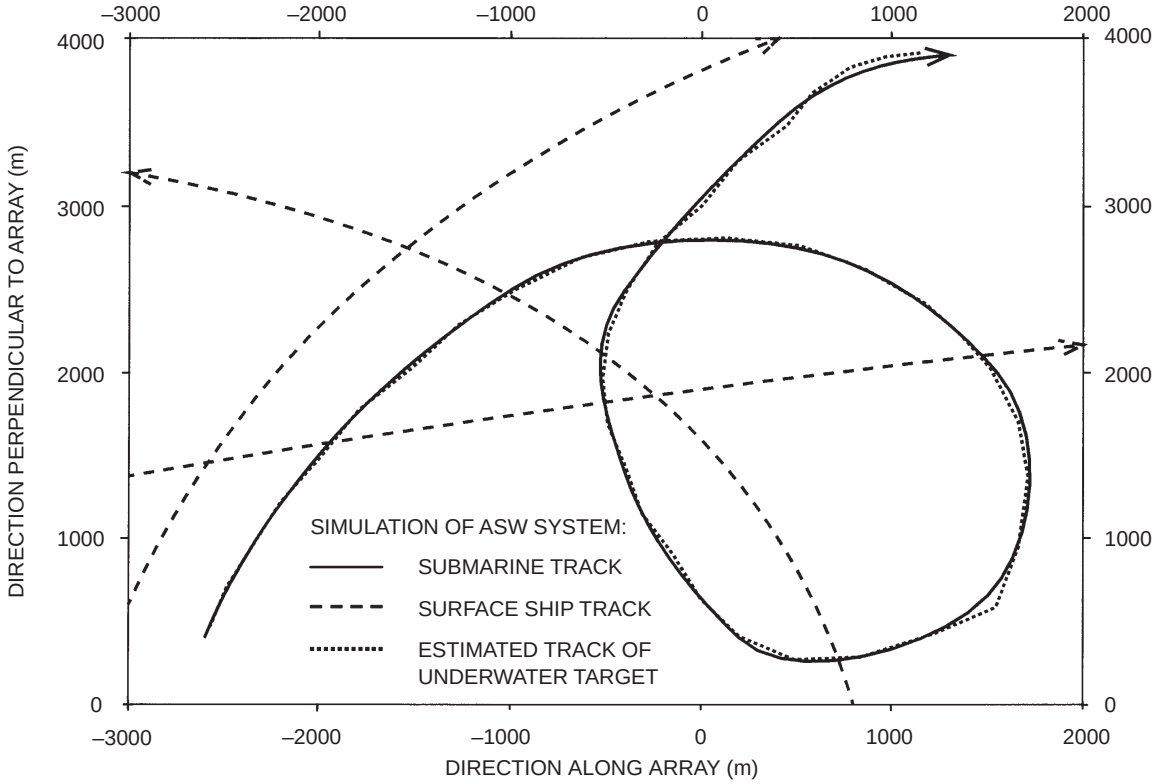

Figure 1. Submarine and three surface ships in shallow channel with sloping bottom.

Array Processing with Three-Dimensional Bathymetry

Objective(s): To quantify the effects of the two-dimensional (2-D) bathymetry assumption on the performance of underwater acoustic array processors (conventional beamforming and matched-field processing) when the bathymetry is actually three-dimensional (3-D). Demonstrate performance improvement by the inclusion of 3-D effects into the processor.

Accomplishment(s): A thorough understanding of 3-D effects on the performance of underwater acoustic array processors has been obtained, and a criterion for determining when these effects are important has been established.

Array processing on underwater acoustic arrays is traditionally performed without regard for the three-dimensionality of the acoustic propagation. Shallow-water environments, however, are seldom two-dimensional (2-D), particularly with regard to bathymetry. Depending on the degree of bottom slope, the path of the acoustic energy can "bend" out of the vertical plane containing the source and receiver, creating an acoustic field significantly different from that predicted with the 2-D assumption. Consequently, serious localization errors and correlation degradations may result from this neglect of the three-dimensional (3-D) effects in array processors. Or, in the case of extreme bending, the acoustic energy may never reach the array, creating a type of horizontal "shadow zone."

These effects were systematically studied via simulations for a wedge-shaped waveguide using a 3-D Gaussian Beam propagation model. A source was allowed to move along a track of constant bathymetry parallel to the wedge apex and away from well-sampled horizontal and vertical line arrays (HLAs and VLAs). Beam degradations and localization errors resulting from the sloping bathymetry were then determined as a function of wedge parameters and source range by comparing performance with that obtained for a source moving over a flat bottom of the same water depth.

Some typical effects are illustrated in figure 1, which compares transmission loss (figure 1a), HLA beam response (figure 1b), and VLA matched-field response (figures 1c and 1d), for a flat bottom with that for a 5°-slope wedge. In both cases, the water depth along the track is 100 m; the source depth is 10 m; and the frequency is 25 Hz. Three distinct regions are clearly discernible in the wedge results. For true source ranges less than about 2.5 km, the results are similar to those for the flat bottom, except for a slight bending of the tracks in figure 1c. The similarity results from the fact that two modes are propagating in both cases. For true source ranges between 2.5 and 6.0 km, the field drastically changes because the higher mode has been stripped out as a result of the sloping bottom, leaving a single propagating mode. The HLA beamformer reports arrivals from other than the broadside direction in this region because each mode travels laterally to the receiver along hyperbolic paths instead of along the track direction. While the matched-field correlation remains high in this region, the absence of the higher mode has degraded the main peak so that reliable range estimation is destroyed by the presence of the high sidelobes. While the source depth estimate is fairly stable in this region, it is in error from the true depth by about 50 m. The 6.5-km boundary marks the entrance into a horizontal shadow zone where the remaining lowest mode is stripped out. Array responses in this region are meaningless and would normally be masked by the ambient noise. The range boundaries defining modal cutoffs can be easily calculated using simple algebraic expressions dependent on mode number, wedge angle, perpendicular distance of source (and receiver) from wedge apex, frequency, and critical angle. These expressions provide a convenient means of determining if 3-D effects will be important in a given scenario.

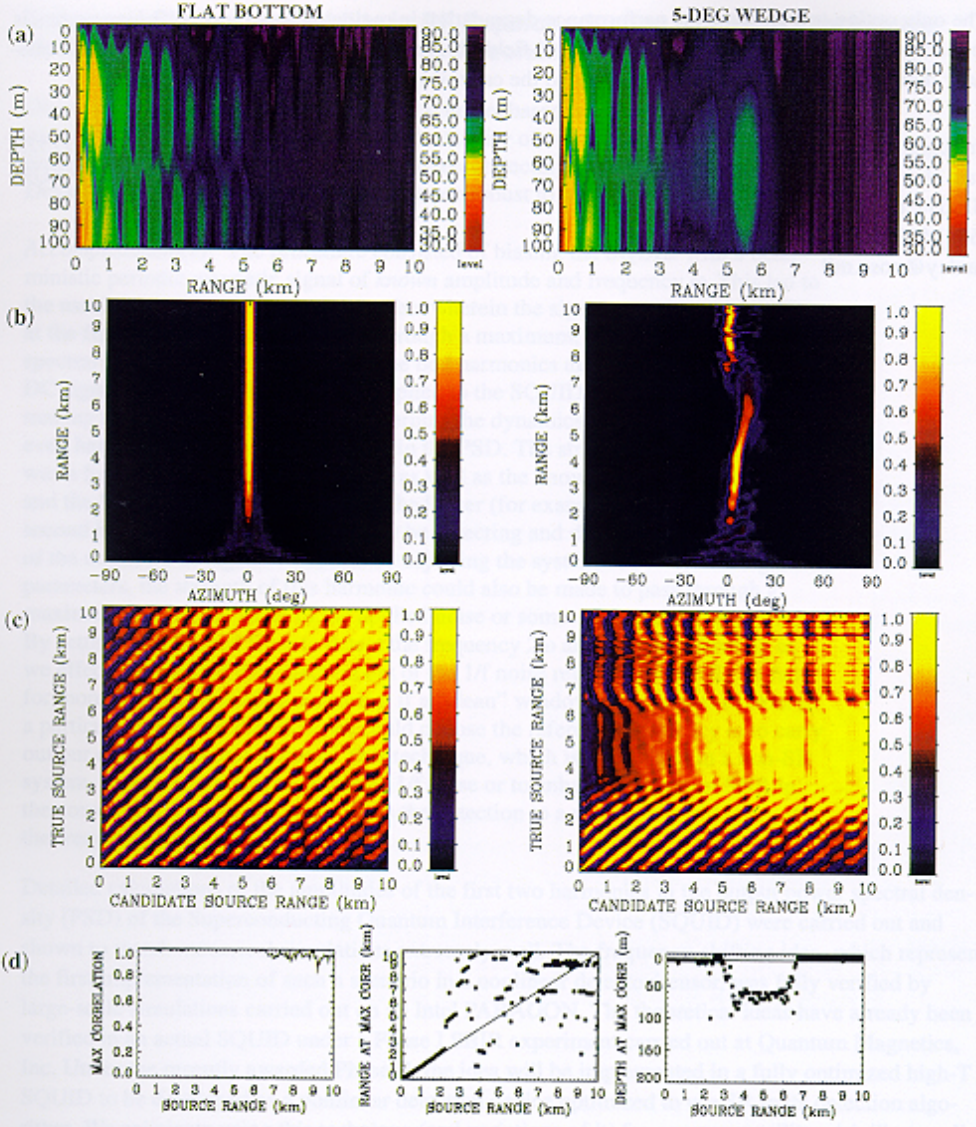

Figure 1. Typical 3-D bathymetric effects on (a) signal field, (b) HLA beam response, and (c and d) VLA matched-field response. Frequency = 25 Hz. Source depth = 10 m. Water depth along track = 100 m. In (a) through (c), the left column is for a flat bottom while the right column is for a 5-degree wedge. In (b), source track is in broadside direction to HLA aperture. All matched-field results use replicas obtained for flat bottom. In (c), candidate source depth = 10 m, and main peak track begins near zero candidate source range (near diagonal in left column). Large sidelobes occur in (c) because only a few modes propagate at this frequency and water depth. In (d), the maximum correlation, and the candidate range and depth of that maximum, for the full range-depth ambiguity surfaces, are plotted over the direction of the track. In (d), the light solid line represents results for flat bottom, for which the maximum correlation is always unity (no mismatch).

The only option to overcome the performance degradation in regions where mode-stripping occurs is to incorporate the 3-D effects into the matched-field processor. Application of this technique successfully regained the lost performance and added the capability of azimuthal discrimination.

Enhanced Signal Detectability in RF Superconducting Quantum Interference Devices (SQUIDs) Using Stochastic Resonance

Objective(s): Investigate a novel biasing scheme, based on the stochastic resonance phenomenon, that will enhance detectability of very weak DC signals in the presence of low-frequency noise in the Superconducting Quantum Interference Device (SQUID), and make the SQUID more robust to background noise.

Accomplishment(s): The procedure consisted of biasing the SQUID with a deterministic periodic magnetic signal of *known* amplitude and frequency ω. This led to the usual stochastic resonance (SR) effect wherein the signal-to-noise ratio (SNR) at the fundamental frequency passes through a maximum, and the output power spectral density (PSD) contains only the odd harmonics ω, 3ω, 5ω, etc. Then, the DC signal that is to be detected was applied to the SQUID. This had the effect of making the potential function that underpins the dynamics asymmetric, and the even harmonics 2ω, 4ω, etc., appeared in the PSD. The strength of these harmonics was a function of the applied dc signal as well as the known signal of frequency ω, and the SQUID parameters. So, a matched filter (for example), set to detect the second harmonic 2ω, would effectively be detecting and determining the strength of the unknown dc signal. Note that by adjusting the system and reference signal parameters, the strength of this harmonic could also be made to pass through a maximum at a critical value of the applied noise or some other control parameter. By setting the matched filter to detect the frequency 2ω and suitably selecting ω, we effectively shifted the detection out of the 1/f noise regime of the PSD. In fact, for more complex operating scenarios, if a "clean" window were known to exist in a particular regime of the PSD, we could choose the reference frequency ω to carry out our detection in that window. This technique, which is impossible in a non-SR system, makes no attempt to eliminate 1/f noise or to enhance the output SNR in the conventional sense; it merely shifts the detection to a more acceptable part of the frequency spectrum.

Detailed calculations of the amplitudes of the first two harmonics in the output power spectral density (PSD) of the Superconducting Quantum Interference Device (SQUID) were carried out and shown to match numerical simulations extremely well. The frequency-shifting idea, which represents the first implementation of such a scenario in a nonlinear detector/sensor, was fully verified by large-scale simulations carried out on an Intel PARAGON. The theoretical ideas have already been verified in an actual SQUID under a Phase I SBIR experiment carried out at Quantum Magnetics, Inc. Under the recently awarded Phase II, the idea will be implemented in a fully optimized high-T SQUID to be developed as a nonlinear detection device optimized to use SR in its detection algorithm. We anticipate using this technique (and variations of it) for numerous military/civilian applications, including nonacoustic-antisubmarine (NA-ASW), mine-detection, biomagnetic sensing, nondestructive evaluation (NDE) sensing, nuclear quadrapole resonance (NQR) detection of explosives (PETN, RDX) and heavy metals (e.g., plutonium) as well as chemical weapons. The last two applications are being considered in connection with the monitoring of weapons' treaty compliance.

BIBLIOGRAPHY

Bulsara, A., M. Inchiosa, and L. Gammaitoni. 1996. “Noise-Controlled Resonance Behavior in Nonlinear Dynamic Systems with Broken Symmetry,” *Physical Review Letters*, vol. 77, p. 2162.

Inchiosa, M., A. Bulsara, and L. Gammaitoni. 1996. “Higher Order Resonant Behavior in Asymmetric Nonlinear Stochastic Systems,” *Physical Review E*, (April, in press).

Environmentally Adaptive Radar Waveforms

Objective(s): Model the physics of low-altitude radio frequency (RF) electromagnetic propagation and surface clutter in range-dependent littoral environments and develop waveforms and signal processing to allow for improved sensor and combat system performance via adaptation to synoptic conditions. Adaptation would entail design of RF waveforms for use in the remote sensing of the propagation environment to allow for improved sensor and combat system performance via adaptation to synoptic conditions.

Accomplishment(s): Computer simulations were made of focused wave mode (FWM)-type waveforms in marine refractivity ducts using an electromagnetic parabolic wave equation model. Validation of this model was accomplished by independent calculations using Sommerfeld-type wave models for mixed (Robin)-type boundary conditions, and by comparison with exact geometric and uniform theory of diffraction calculations for wedge diffraction models in collaboration with the Applied Research Laboratory, University of Texas.

The smooth variable surface electromagnetic (EM) parabolic equation model was extended to include surface roughness effects and to compute surface back scatter corresponding to a rough ocean surface. This was done by incorporating an ocean spectral surface wave model to produce a two-scale rough surface, and modeling the coherent surface Bragg back scatter from capillary waves. The scattering calculation makes use of a multiple forward scatter, single back-scatter parabolic equation (PE) model via a distorted-wave Born approximation that takes into account the tilt of the ocean surface due to gravity waves. Basically, the low-wave-number surface gravity waves provide a tilt to the ocean surface upon which the higher wave number capillary waves then propagate.

Unlike other two-scale theories of surface scatter, surface shadowing and diffraction are automatically included via the parabolic equation. Finite conductivity effects and polarization-dependent reflection losses (e.g., Brewster angle phenomenon) are included in the surface scatter treatment. The ocean spectral wave model depends upon wind speed, wind direction, fetch, swell direction, and water temperature. Preliminary comparisons with sea surface clutter data from the LOGAN (Low Grazing ANgle) experiment in Chesapeake Bay indicate qualitative agreement with X-band simulations for spatially varying normalized radar cross-section from a periscope-type target at the ocean surface. In particular, strong fluctuations in sea clutter power and target echo are observed.

Propagation simulations of low-altitude (e.g., 3- to 10-m) targets in range-dependent surface ducts characteristic of marine environments have shown substantial improvement in target illumination over conventional types of transmit waveforms. The focused wave mode (FWM) pulse involves spatial aperture shading based upon matching dominant propagation modes in ducts. This technique was based upon a hypothesized or known refractive environment. A method has been proposed in conjunction with D. Boyer, Naval Surface Warfare Center, Dahlgren Division (NSWCDD), to do passive remote sensing using matched-field-type algorithms by using an existing forward propagation model based upon the PE method.

Figure 1 shows an example of the rough sea surface scattering for a 20-knot wind speed case at X-band. This simulates the sea surface clutter for an APS-137-type radar.

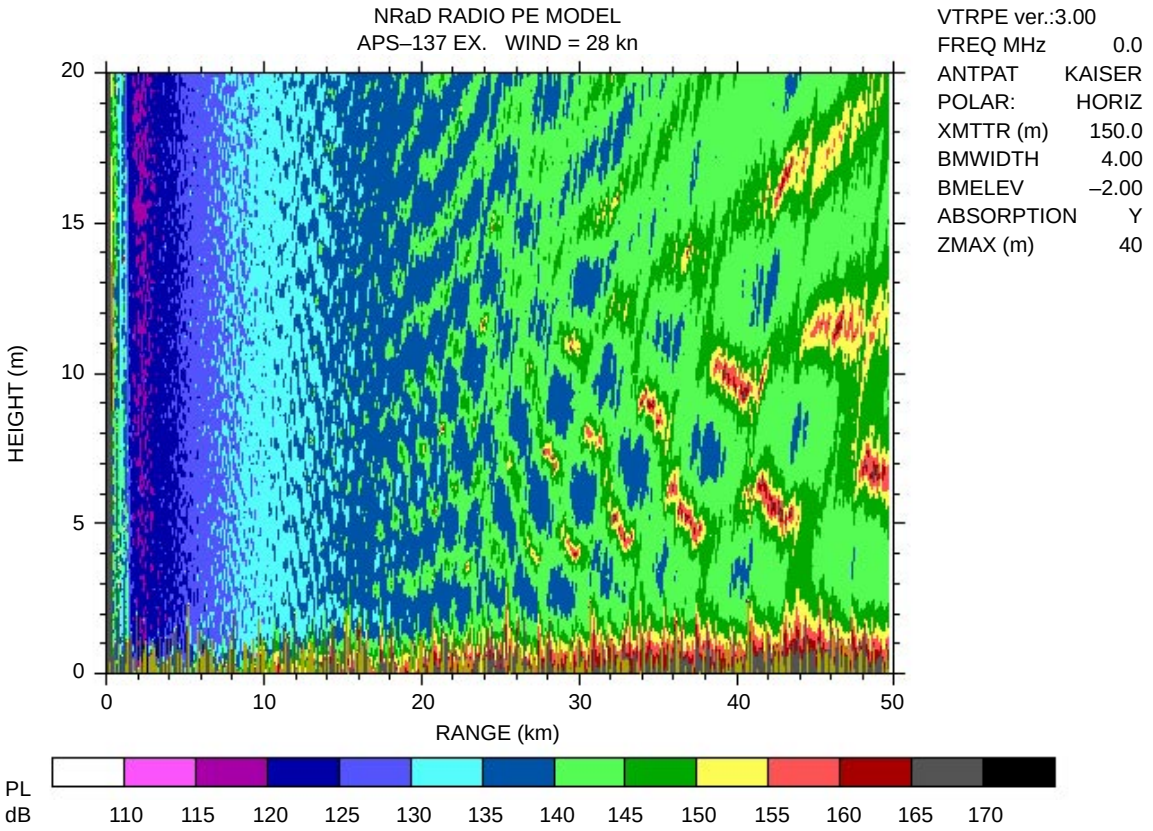

Figure 1. APS-137 sea clutter.

Low observable targets, such as cruise missiles, flying at low altitudes are difficult to detect at long ranges and place increasing demands on shipboard weapon and fire control systems. The propagation and clutter environment, as sensed by shipboard radar sensors, limits system detection and tracking effectiveness and thereby degrades reliable weapon delivery. The propagation and clutter seen by sensors is highly variable spatially and temporally, but current sensors are optimized to operate based upon static environmental assumptions.

The problem is both one of obtaining sufficient target illumination at long range and of detecting a small radar-cross-section target echo against strong surface clutter. The target-detection problem is often compounded by atmospheric environmental conditions that give rise to anomalous propagation effects. In marine environments, or over land, there often exist spatial gradients of temperature or humidity near the surface. These gradients produce local extrema in the index of refraction profile, called surface ducts, that can channel or trap electromagnetic energy. Detailed measurements of near grazing incidence propagation and clutter display large variations with respect to frequency, target and sensor altitude, target bearing, and time.

Usually, the presence of a surface duct is viewed as being deleterious to radar system performance because the resultant propagation conditions are often complex and vary dramatically with the local environmental conditions. However, instead of viewing anomalous propagation as simply a detriment to system performance, one could adopt the approach of trying to mitigate or even exploit the environmental effects to improve system performance. In fact, it may be feasible to design

waveforms that can probe or remote-sense the propagation conditions surrounding a ship, or transmit environmentally adaptive radar pulses that reduce surface clutter.

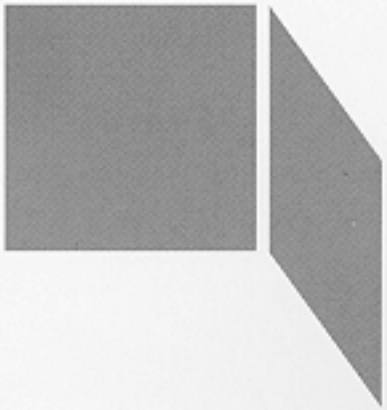

OTHER LEADERSHIP AREAS

Modeling of Diffusion and Flow in Porous Media

Objective(s): Investigate and describe the behavior of model porous systems in order to better describe and predict the behavior of real-world systems such as subsurface contaminate spread and migration.

Accomplishment(s): Models were created to produce fractal flow paths through random porous three-dimensional (3-D) structures. The geometries of these flow paths and the flow patterns within them were investigated.

The migration of subsurface contamination occurs through the pores inherent in geological structures. The need to identify and monitor this migration has become a significant cost of the base-closure process, as well as a significant cost borne by some private-sector corporations. An increased ability to predict this migration of subsurface contamination would speed clean-ups, reduce the need for expensive, multiple site characterizations, and increase the effectiveness and certainty of clean-up efforts. Modeling of porous structures, and the analysis of the net transfer of material within and through such structures, should lead to a fundamental increase in the predictability of real-world transport.

This project has focused on the creation of models of flow volumes within porous media and the interactions that affect the movement of material through these volumes. The flow volumes created were generated by allowing the infusion of a liquid to occur through a three-dimensional (3-D) model of a porous structure; we used the techniques previously applied to two-dimensional models. The porous structure was assumed to consist of two intertwined regions, one solid and one void. The void volume was assumed to be initially filled with some fluid. The modeling process began by randomly assigning pore sizes to the connections between the void microvolumes. These pores then acted as choke points for the infusion and flow of material within the solid network.

The invasion process began by allowing invasion into one side of a 3-D box of pores/voids. The box was assumed to possess periodic boundary conditions in all directions other than the flow direction. During the infusion, the invading liquid expanded in a step-wise fashion to occupy an additional microvolume through the pore with the maximum pressure differential, which was through the smallest, non-zero pore. The infusion was terminated when a preset number of pores on the exit side were invaded. This infused volume was then used in a second step to allow flow and diffusion to occur. The two separate components of flow and diffusion were quite distinct due to the total infusion volume consisting of two distinct regions: the primary connected path (through which the flow occurred) and a secondary set of dead-end branches in which no flow occurred but into which material could diffuse.

Crystallization of Silicon Films with Contoured Excimer Laser Beams

Objective(s): Investigate the usefulness of contoured excimer laser beams in forming device-quality, thin silicon films on amorphous surfaces.

Accomplishment(s): Developed the use of three-dimensional (3-D) plots of temperature or melt depth vs. time and energy to model the effects of excimer laser heating of thin amorphous silicon (a-Si) films. Linear-graded intensity, excimer laser beams were used to heat and crystallize 1000-Å a-Si films. Chemical techniques were used to characterize the laser-crystallized silicon films.

High-quality, thin silicon films on amorphous surfaces are important in many present and planned Navy communication, signal-processing, and display systems. The deficiencies in current methods either limit the substrate to silicon, as with the Separation by Implantation of Oxygen (SIMOX), or result in low device quality, as with the use of uniform temperature heating to crystallize the thin silicon film. This project seeks to overcome these limitations by developing a technique of excimer laser heating with contoured beams.

A laser-heating program for silicon on sapphire (SOS) was obtained from Prof. Michael Thompson of Cornell University. Modeling was performed on SOS structures to evaluate the program. Initial outputs were individual plots of surface temperature and melt depth as a function of time, for various laser intensity (energy) levels. The program was modified to deal with silicon, fused silica, and other substrates. The program has been further modified to include an intermediate layer of fused silica and to obtain the interlayer temperature between the fused silica and the substrate. Three-dimensional (3-D) plots of temperature or melt depth vs. time and energy have been obtained to model the effects of uniform and gradient heating of thin silicon films. Figure 1 shows a modeled 3-D plot of a thin silicon film melting on a sapphire substrate with a uniform intensity beam.

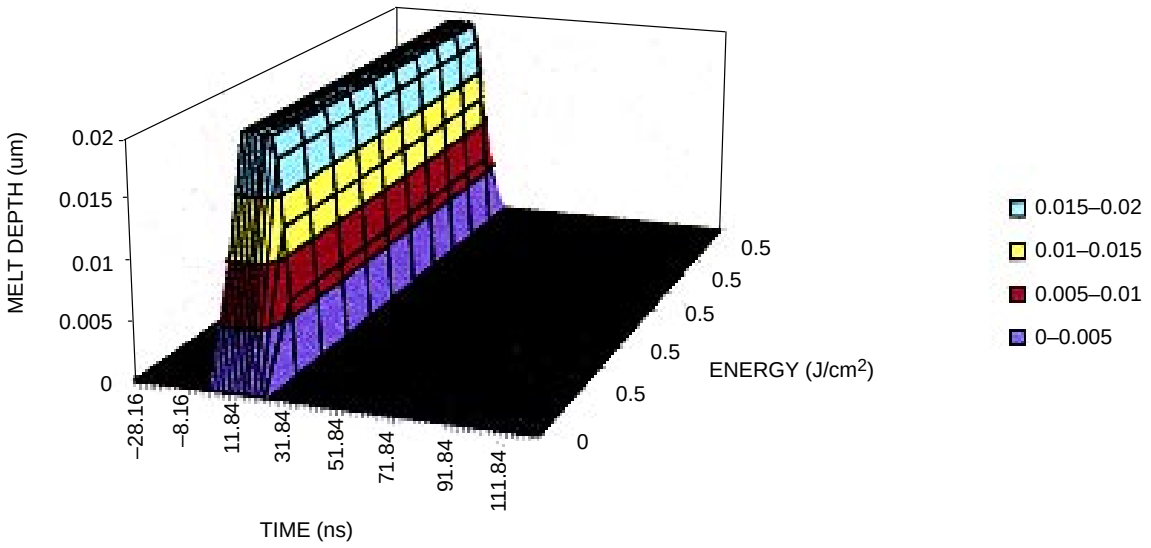

Figure 1. Modeled 3-D plot of thin silicon film melting on a sapphire substrate with a uniform intensity beam.

Figure 2 is a plot generated in a similar manner but with the use of a linear-graded intensity beam.

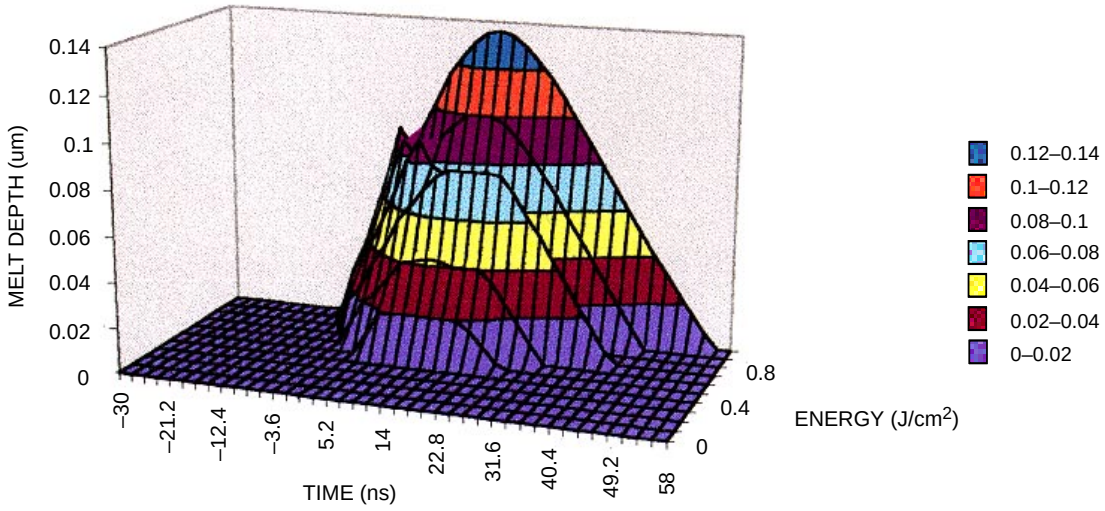

Figure 2. Modeled 3-D plot of thin silicon film melting on a sapphire substrate with a linear graded intensity beam.

The effect of placing a lower thermal conductivity layer between the thin silicon film and the substrate has been modeled. Figure 3 is a plot of the interface temperature between an intermediate layer of fused silica and the substrate at different laser-beam intensities.

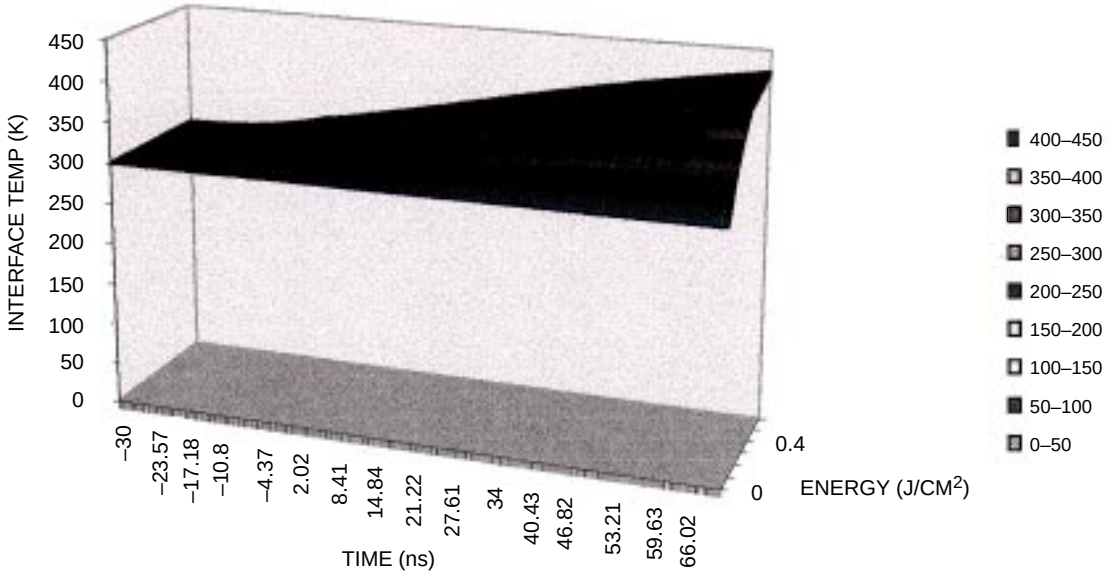

Figure 3. Modeled 3-D plot of the interface temperature between a fused silica thermal barrier and the silicon substrate as a result of linear-graded intensity beam heating of a thin silicon film.

These results indicate that the fused silica layer acts as a thermal barrier. As a result, a-Si layers may be crystallized in the liquid phase without detrimentally affecting temperature-sensitive substrates. A better means of understanding the effects of gradient heating in the liquid phase crystallization of thin silicon films through the use of gradient optics can be visualized when the plot of varying-beam intensity is transposed into terms of lateral distances. As compared to uniform heating in figure 1, one can now envision a directionality to gradient heating and its subsequent cooling when referring to figure 2. This directionality can provide a means by which preferred directed crystal growth can now proceed in the thin silicon film.

A computer-controlled laser heating station with an optical-beam delivery system designed to produce linearly graded intensity profiles has been developed. It consists of a Questek model 2860 excimer laser with specially designed linear-gradient optics. The excimer wavelength used was 248 nm. The structure used for the laser-heating experiments was a stack that consisted of a 1000-Å-thick a-Si layer that was deposited on a 5000-Å-thick fused silica film. This in turn was supported on a {100} oriented single crystalline silicon substrate. The beam size used was 0.5 cm by 0.5 cm. Silicon-film structural changes, noted by changes in film color, occurred at energy densities between 0.7 and 1 J/cm^2. Above 1 J/cm^2, film ablation was noted. Both single- and multiple-beam exposures were used to heat these 1000-Å thin a-Si films. If the beams were stepped in the multiple exposure mode, overlap effects were noted with uniform intensity profile beams. However, for linear-gradient intensity beams, little or no stepping effects were noted.

A rapid means of characterizing the crystal nature of the laser-heated film is with the use of chemical etches. A 10-percent water-diluted, Secco etch (2HF:0.15M $K_2Cr_3O_7$) has been found to be a good method in delineating the grain boundaries of thin silicon films. Both uniform and linear-graded laser beams were used to crystallize 1000-Å silicon films on 5000-Å fused silica/silicon substrates. Preliminary results indicated that the use of a 10- to 90-percent linear intensity gradient over a 10-cm length resulted in a grained crystalline film. These results are encouraging and warrant further examination in the use of contour gradients in the excimer laser heating and crystallization of thin silicon films.

Segmentation of Independent Motion via Pattern Recognition of Motion Flow in the Log-Polar Transformed Domain

Objective(s): Develop a robust method for segmentation of independent motion as observed by a moving camera through the use of pattern recognition of motion flow in the log-polar transformed domain.

Accomplishment(s): Developed a mathematical model for robust motion classification through pattern matching of the sign of the motion flow along predefined sets of directions in the log-polar domain.

Segmenting independent motion from a moving background (as observed by a moving camera) has been a problem for vision researchers. However, the human visual system can segment independent motion with signal-to-noise ratios as low as 1/100. Recently, neurobiologists have found the existence of cells in the visual pathways of monkeys that perform global operations on large-area motion (as required for characterizing egomotion) and other cells that responded to the motion of small objects. Mathematical projections have also been developed recently that allow robust (although computationally intensive) computation of many navigational parameters via pattern matching of qualitative visual motion information. These findings suggest that there may be efficient and robust methods of motion segmentation based on pattern matching in the biologically based, log-polar domain.

We developed a mathematical model for a fast and robust motion-classification method through template matching of the signs (positive/negative) of the projections of the motion flow on predefined sets of directional vectors. The speed of the algorithm was derived from the data-reduction nature of the log-polar transform. The robustness came from the nature of the information used, namely the signs of the projection of the normal flow (the component of the optical flow perpendicular to the brightness edges—the only motion information that can be extracted by local computations from a sequence of images). Pattern matching provided a means to reduce the dimensionality and complexity of the problem.

We conducted tests of the model with calibrated image sequences. Along the way, we obtained significant findings regarding the exact discrete method for performing the log-polar transformation to preserve conformality. We also developed and published specific techniques for optimizing visual computations in the discrete domain.

Solution of Large Sparse Indefinite Systems in Least Squares and Optimization

Objective(s): Develop a sparse-ordering and factorization algorithm that applies to general systems of equations Mx = b, in which M may be symmetric or unsymmetric, definite or indefinite.

Accomplishment(s): Extended and improved on the computational efficiency of the original sparse-ordering algorithm by developing and implementing an efficient linear method for the symbolic factorizations required in a new recursive version of the sparse-ordering method. The new symbolic factorization method has led to an implementation that is very suited for parallel-architecture machines. Also, the core of the invention, described in a patent on this subject called “search” pre-processor, has been improved significantly.

Large sparse systems of equations Mx = b arise in many important DoD applications. Examples include least-squares and damped-least-squares computations for estimating unknown parameters, curve fitting, and data smoothing in signal-processing applications, optimization, as well as target strength and structural acoustic interaction problems investigated at NRaD with the aid of the computer program CHIEF (Combined Helmholtz Integral Formulation).

In the majority of these computationally intensive DoD applications, the total cost is completely dominated by the equations solver, and so by taking advantage of the sparsity inherent in a problem, huge savings in storage and execution time can be obtained. The basic strategy in sparse matrix theory is two-fold: First, store only the nonzero data. Second, perform operations only on nonzero operands. For example, consider a typical 935-by-900 matrix arising in a target-strength problem investigated at NRaD [1] where the number of nonzeros in the matrix is 22,860. If one represents M as a full matrix, a storage of 841,500 words is required, and operations are done on 841,500 words. In contrast to the full case, sparse matrix theory allows us to store the matrix in about 22,860 words and perform operations on 22,860 words. This example taken from a real Navy investigation gives us an idea of why and how huge savings in execution time can be obtained in the solution of large sparse systems of equations.

In most sparse systems of equations Mx = b, there is significant structure hidden within the underlying matrix, M. With the current emphasis placed on parallel architecture computers, a major direction in scientific computation is to find within the sparse problem, a structure that is well-suited for computation on these parallel computers. In other words, we wish to partition the original problem into smaller parts so that these parts can be solved independently on different processors of the parallel machine.

In recent years, we developed an ordering algorithm [2] for computing a permutation matrix, P, so that parallelism inherent in a general symmetric matrix, M, is fully exposed in the reordered matrix, PMP^T. In principle, our approach was designed for symmetric matrices, but more general systems such as overdetermined (nonsquare) or nonsymmetric systems may be cast into the symmetric form [3]. The approach in [2] was a one-step procedure that finds parallel parts only in the original symmetric matrix. Subsequently, we extended the work in [2] to design an algorithm that recursively uses the ordering scheme in [2] to find, as well as eliminate, all identified parallel parts until the original

problem is reduced to a small dense system. At this point, a standard dense solver is applied to the reduced system to obtain the final solution of the original system.

The most demanding and costly component in our new recursive ordering scheme is a part that requires the computation of fill-ins. In sparse matrix terminology, a fill-in is a nonzero entry in a position that was zero in the original matrix. The key difficulty in the computation of a fill-in stems from the fact that it has to be done without any numerical computation, a feature called symbolic factorization. A key characteristic of symbolic factorization is that it is highly sequential, requiring the traversal of long paths in the undirected graph of the original matrix in order to compute each fill-in. The traversal of long paths in graphs can be very costly. Moreover, a sequential traversal does not lend itself to parallel computation so that one could make use of parallel computers to speed up the computation of fill-ins.

We have derived a new formulation that has led us to the development of a new procedure for computing fill-ins with the following two important properties: First, for each fill-in computed in the recursive ordering scheme, the procedure traverses a path no longer than length 2. This is a significant improvement since the previous scheme required traversal of paths proportional to the size of the matrix. Second, the scheme derived from the traversal of paths of length 2 has allowed us to formulate a procedure that is ideally suited for parallel-architecture computers.

The extension of the ordering scheme reported in [2] to the recursive form, coupled with the new results obtained on the computation of fill-ins, as well as a pre-processor called “search,” bring in a major improvement over a patent published in this area [2] by this author. Finally, a C implementation of the algorithm written presently in MATLAB language, has been initiated.

REFERENCES

1. Schenk, H. A., G. W. Benthien, and D. Barach. 1995 “A Hybrid Method for Predicting the Complete Scattering Function from Limited Data,” *Journal of the Acoustical Society of America*, vol. 98, no. 6, pp. 3469–3481.

2. Kevorkian, A. K., 1995. “Method and Apparatus for Pre-Processing Inputs to Parallel Architecture Computers,” United States Patent 5,446,908.

3. Gill, P. E., W. Murray, D. B. Ponceleon, and M. A. Saunders. 1991. “Solving Reduced KKT Systems in Barrier Methods for Linear and Quadratic Programming,“ Technical Report SOL 91–7. Systems Optimization Laboratory, Department of Operations Research, Stanford University, Stanford, CA.

Use of the “Laser pH Jump” to Initiate Ground-State Reactions for Robotics

Objective(s): Investigate the “laser pH jump” as a means of sustaining a macroscopic pH change long enough for a polymer to expand or contract (milliseconds). To date, pH changes have been sustained for nanoseconds in a microscopic volume.

Accomplishment(s): Synthesized an expandable polymer and measured a 22-fold reversible volume change by manually changing the pH a half unit; confirmed the existence of a jump molecule with a protonated peak large enough to be used for the muscle experiment (see figure 1).

This project investigated a novel concept (the “laser pH jump”) for light activation of polymeric actuators (“artificial muscles”) for robotics. Some polymers swell or shrink dramatically as the pH is increased or decreased, respectively. Until now, the activation process has been limited by the slow diffusion of hydrogen ions to the active site. We suggested an *in situ* technique whereby jump molecules located *immediately adjacent* to the polymer network would be accessible for irradiation. These jump molecules have grossly different acidity constants in the ground and excited electronic states. Thus, when a jump molecule is excited with *visible light*, the hydrogen ion concentration changes by orders of magnitude (“pH jump”) in a very short time (nanoseconds).

This work affects virtually all applications in which actuators might be used, including sensors and pumps where nonmetallic parts are required. For underwater use, light-activated actuators can be controlled using fiber-optic cables, further eliminating the need for mechanical or electrical components. In the biomedical area, these synthetic muscles approach the peak powers of mammalian muscle and can be used in telepresence surgery.

Kinetic equations were written and used to predict the characteristics required in a jump molecule. These characteristics are: (1) long lifetime at room temperature; (2) excited-state pK grossly different from ground-state pK; (3) the pK change must go through the midpoint of the polymer; and (4) last, but very important, the jump molecule must absorb in the visible region of the spectrum. A family of candidate jump molecules with these characteristics was found. The 0-time absorption spectrum of a typical candidate jump molecule was obtained in a highly protonating solvent, thereby confirming the existence of a protonated peak with a large absorption coefficient. The 0-time spectrum was extrapolated from a series of spectra taken at 20-second intervals, with the first spectrum at 10 seconds and the last at 790 seconds. Figure 1 shows the initial and final spectra. Note that, as indicated by the arrows, all the peak intensities increased with time except the peak at 424 nm (protonated anthracene), which decreased with time.

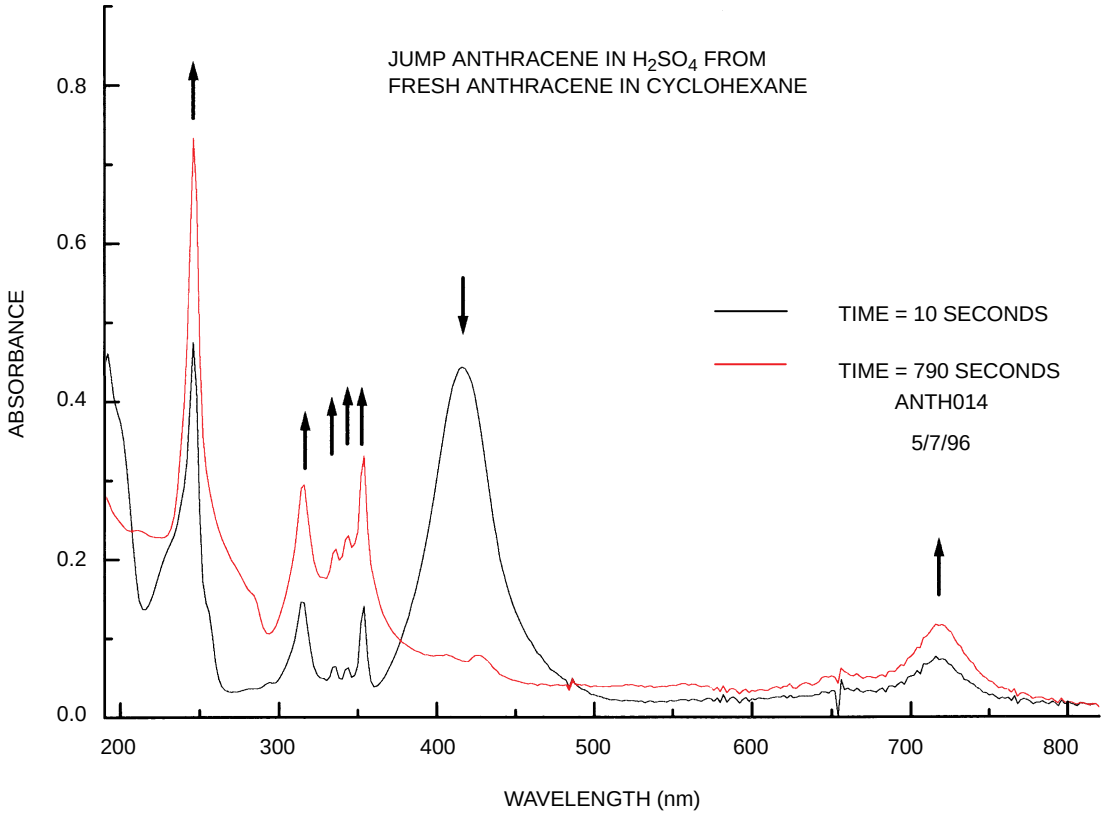

Figure 1. Absorption spectra at t = 10 s and t = 790 s of candidate jump molecule anthracene in sulphuric acid. Note that impurity peaks (indicated by up arrows) increase with time; the peak at 424 nm due to protonated anthracene (indicated by a down arrow) decreases with time.

Principal Investigator:
Dr. Carol A. Becker
NRaD Code D894
(619) 553–3906
becker@nosc.mil

0601152N
NRaD ZU28

The Dirac Wave Equation—Multiple Quantum-Well Structures

Objective(s): Develop an eight-by-eight matrix representation of the quantum-mechanical Dirac equation suitable for solving wave-propagation problems involving the interaction of single free electrons in the presence of multiple quantum-well structures.

Accomplishment(s): (a) An eight-by-eight matrix representation of the quantum-mechanical Dirac equation has been developed for solving wave-propagation problems involving the interaction of single free electrons in the presence of multiple quantum-well structures. (b) A computer program, using MATLAB software on a Sun 4 SPARCstation 2, has been developed for predicting transmission and reflection characteristics of multiple quantum-well structures.

Research in solid-state materials and devices is necessary for continued improvement in performing mathematical functions in computing, signal and image processing, and displaying information required in the areas of information understanding, ocean surveillance, communications, high-performance computing, human–computer interfaces, and navigation. In particular, research directed toward understanding the behavior of quantum-mechanical electronic and electro-optical nanostructures is essential in achieving long-range goals associated with the fabrication of high-speed, high-density computer chips to be used in futuristic Navy computing architectures.

During the past 4 years, a new matrix representation of the Maxwell field equations has been developed by Dr. Richard P. Bocker of NRaD in collaboration with Dr. B. Roy Frieden of the University of Arizona Optical Sciences Center. NRaD Technical Documents 2259, 2320, and 2569 and the *IEEE Transactions on Education* paper (vol. 36, no. 4, November 1993, pp. 350–356) describe this newly developed matrix representation. The basis of this matrix representation is an eight-by-eight space-time differential matrix operator. This matrix operator was formulated from the vector differential form of the Maxwell field equations. The resulting matrix formulation of Maxwell's equations allows simple and direct derivation of the electromagnetic wave and charge continuity equations; the Lorentz conditions and definition of the electromagnetic potentials; the Lorentz and Coulomb gauges; the electromagnetic potential wave equations; and Poynting's conservation of energy theorem. This matrix representation has been used to solve multilayer thin-film optical wave-propagation problems where the polarization state, angle of incidence, and wavelength of incident electromagnetic waves may be specified for thin-film geometries involving any number of dielectric and/or conducting layers. Specifically, the reflection and transmission characteristics of dielectric interference band-pass filters, high-reflection coatings, anti-reflection coatings, Fabry–Perot filters, polarization filters, evanescent wave couplers, and plasmon surface-wave modulators can be easily analyzed using computer software developed here at NRaD based on this eight-by-eight matrix representation. The software package called MATURE (Matrix Approach To Understanding Relativistic Electrodynamics) was written using the high-level programming language MATLAB for use on a Sun 4 SPARCstation 2 workstation.

The primary goal of this project is to extend the newly developed eight-by-eight matrix representation of the electromagnetic Maxwell field equations to the quantum-mechanical Dirac equation, with specific application to the interaction of electrons with multiple quantum-well structures. Particular goals include the following items:

1. Solve the eight-by-eight representation of the Dirac equation for an infinite space containing fixed potentials. Determine the energy and spin-eigenstates.
2. Solve the eight-by-eight representation of the Dirac equation for two semi-infinite spaces with constant potentials separated by a planar interface. Determine the boundary conditions imposed on the wavefunctions through the use of partition functions. Look for relationships analogous to Snell's law, law of reflection, and the Fresnel equations obtained for electromagnetic counterpart.
3. Solve the eight-by-eight representation of the Dirac equation for a single layer separating two semi-infinite spaces separated by parallel planar interfaces. Consider both the quantum-well and barrier-tunneling scenarios. Determine the transmission and reflection characteristics of the single layer as a function of incident electron energy, angle of incidence, and spin-state. This is analogous to the electromagnetics thin-film problem involving monochromatic plane-wave light of arbitrary wavelength, angle of incidence, and polarization state.
4. Map solutions obtained using the eight-by-eight Dirac representation to solutions satisfying the four-by-four Dirac representation. Compare results with known results in the literature. Also, compare solutions to those obtained using the Schrodinger equation.
5. Develop a computer program using MATLAB software on a Sun 4 SPARCstation 2 for multiple quantum-well structures analogous to the MATURE program developed for electromagnetic wave propagation through multilayer thin-film problems. Test and evaluate the software.

The aforementioned eight-by-eight space-time differential matrix operator has been successfully used in formulating a new eight-by-eight representation of the Dirac equation for describing the behavior of free Dirac spin-1/2 particles. It is noted that the conventional four-by-four matrix representation of the Dirac equation forms the basis of quantum-mechanical phenomena involving particles where spin, high speed, and positive (negative) energy states are of importance. An eight-by-four transfer matrix, describing the mapping of solutions obtained from the eight-by-eight representation to the four-by-four formulation, has been derived. The eight-by-eight matrix representation of the Dirac equation has also been used to formulate a vector differential and integral formulation of the Dirac equations, which resemble the Maxwell field equations in vector form. The eight-by-eight matrix representation of the relativistic quantum-mechanical Dirac equation has been successfully used to solve wave-propagation problems involving electrons through multilayer thin-film structures. The MATURE software package has been expanded to handle the propagation of quantum-mechanical matter waves through thin-film structures as well. The spin state, angle of incidence, and relativistic energy (positive or negative) of incident matter waves may be specified for thin-film geometries involving any number of potential barrier and/or potential well layers in the presence of external electric and magnetic fields. The reflection and transmission characteristics of multiple quantum-well structures, superlattices, quantum-mechanical tunneling diodes and transistors, as well as other nanostructures can be analyzed using the MATURE computer software. Present experimental work at NRaD in the area of multiple quantum-well structures heavily relies on the use of the Schrodinger wave equation. Hence, electron spin, relativistic speed, and negative energy states are not taken into account. Solutions of the Dirac equation when applied to multiple quantum-well structures in the presence of electric or magnetic fields may yield new insights and structure geometries not available with the Schrodinger approach.

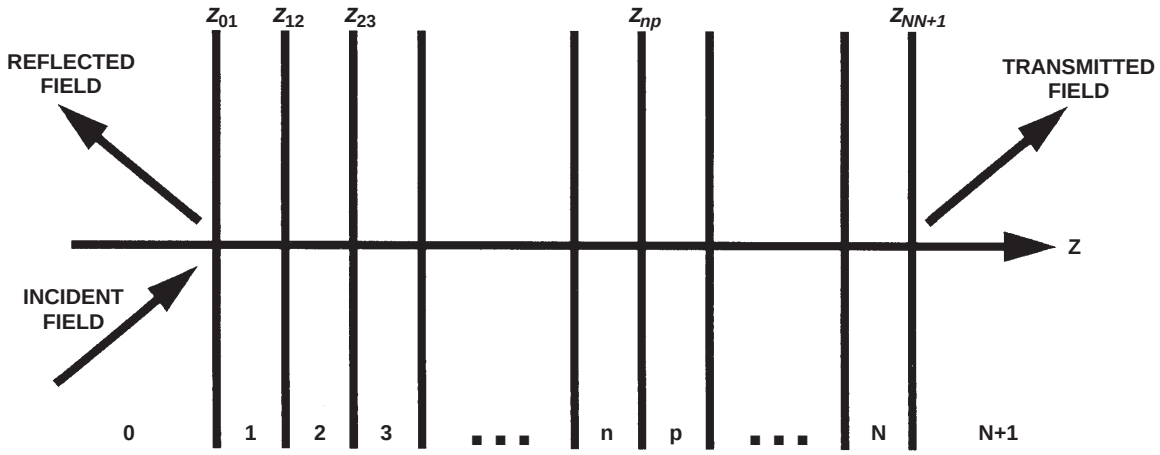

Figure 1. Multilayer thin-film geometry.

A Predictive Capability for the Fate of Shipboard Discharges

Objective(s): Develop a numerical model that can predict the fate of Navy shipboard discharges by accounting for both the hydrodynamics of the turbulent wake and the far-field ambient advection-diffusion.

Accomplishment(s): The numerical wake model, TBWAKE, was successfully combined with an ambient advection-diffusion model, RMA11, providing an integrated numerical procedure for predicting the fate of Navy shipboard discharges.

The US Navy is required by law to comply with International Maritime Organization regulations restricting discharges from vessels in international waters. Because of the potential impact such restrictions impose on maritime operations, the Navy is interested in determining to what extent, if any, discharges from US Navy vessels lead to adverse marine environmental effects.

The basic problem of interest involves a surface ship in the open ocean on a fixed heading at constant speed. A pollutant is discharged at a constant rate and fixed concentration from a discharge port in the hull. The discharge plume streams aft along the hull and into the wake of the vessel. In the "near wake," mixing is dominated by wake turbulence due to the action of the hull and propellers. In the "far field," where wake turbulence is negligible, dispersion is due primarily to currents, settling, and ambient ocean turbulence. The challenge is to predict the far-field pollutant concentration and discharge-plume geometry.

Currently available numerical models, applicable to the problem at hand, are either "near-field" ship wake models or "far-field" advection-diffusion models. None of the models currently addresses both near-field and far-field dispersion. The objective of the present IR effort is to combine a wake model with an advection-diffusion model, creating an integrated system that can predict the fate of Navy shipboard discharges. The wake model selected for this effort was TBWAKE, developed by Mark Hyman of NSWC, Coastal Systems Station, Panama City, Florida. The far-field model selected was RMA11, developed by Ian King of the University of California at Davis. These two codes have been successfully integrated such that the "near wake" solution from TBWAKE serves as the initial conditions for a far-field solution from RMA11.

TBWAKE is a Reynolds-averaged Navier-Stokes solver with turbulence models. TBWAKE was originally written to model microbubbles in the wake but was adapted to handle a distribution of particulates with densities greater than that of water. The particle diffusivities vary with particle size and depth and are read-in from an input file. A passive dye tracer, or scalar, can also be tracked downstream.

RMA11 is a three-dimensional finite element model for simulating water quality in estuaries and streams. In addition to solving the transport equations, RMA11 also solves biological and chemical rate reactions including, but not limited to, the oxygen cycle, phosphorous cycle, nitrogen cycle, and algae growth. RMA11 solves the transport and reaction equations at each time step and outputs pollutant concentrations.

In an effort to verify the RMA11 solution of the transport equations, RMA11 predictions were compared with exact solutions for a number of one-dimensional and two-dimensional advection-diffusion problems. In each case, the RMA11 solution converged to within 1 percent of the exact

analytical solution. TBWAKE comparisons were made to measurements collected by the *ECOS*. The *ECOS* traversed the wakes of the *Acoustic Explorer* and the frigate USS *Vandergrift* (FFG 48). The TBWAKE predictions compared favorably with the measured field data. The main difference was that the discharge plume in the experiments spread horizontally more than the TBWAKE solution. Furthermore, while the TBWAKE concentration contours retained a self-similar geometry, the measured data did not. Figure 1 compares the measured dye dilution with those predicted by TBWAKE for the frigate *Vandergrift* at 15 knots. The output data from TBWAKE's near-field solutions were used as the initial conditions for several RMA11 dye-plume simulations. Figure 2 presents the combined TBWAKE–RMA11 solution at 30 ship lengths behind the 15-knot frigate. This figure shows the dye concentration contours of the discharge plume cross-section.

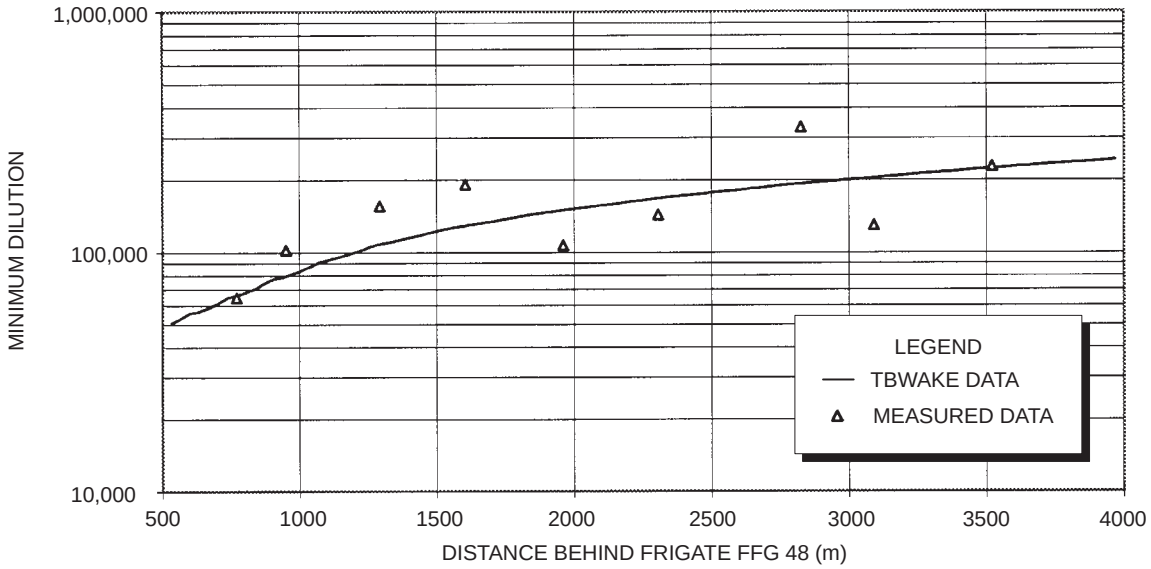

Figure 1. Comparison of TBWAKE solution with measured dye dilution.

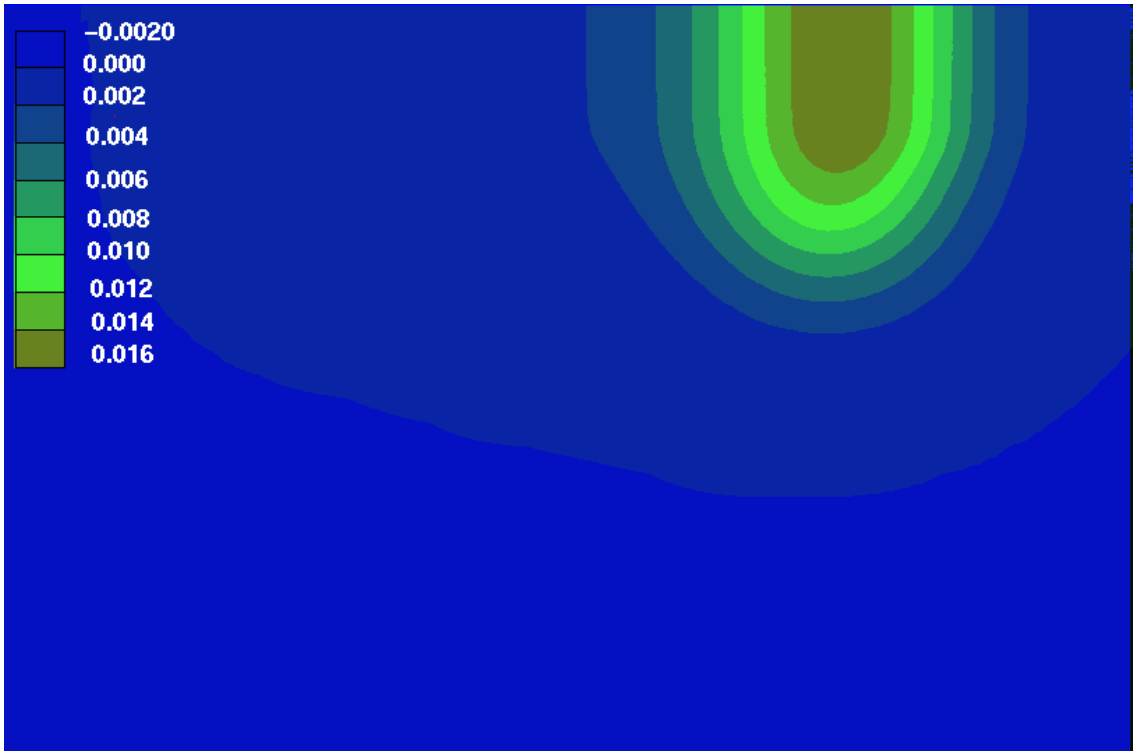

Figure 2. Cross-wake dye concentration contours in mg/l. Combined TBWAKE–RMA11 solution at 30 ship lengths behind 15-knot frigate.

Development of Ultramicroelectrode (UME) Arrays for Use in a Remote Probe

Objective(s): Develop ultramicroelectrode (UME) arrays to perform electrochemistry in both the gas and liquid phases for use as sensors in a remote probe. Such a remote probe could be used to continuously monitor a given environment or for field screening.

Accomplishment(s): Prepared disk and ring UME arrays and used the arrays to obtain voltammograms of target compounds in the gas and liquid phases. Determined the effects of epoxy resin and temperature on the voltammetric response.

NRaD has been involved in developing sensors to detect environmentally important compounds in both marine and subterranean environments. To detect fuel products *in situ* in soils, a truck-mounted, cone penetrometer system was equipped with a fiber-optic-based, laser-induced fluorometer (LIF) system. Other sensors currently under development at NRaD for the cone penetrometer include the camera, to measure soil porosity as a function of depth; time-domain reflectometry (TDR), to monitor moisture content in the soil; and laser-induced breakdown spectroscopy (LIBS), for metal detection in soil. However, despite the need, a cone-penetrometer-based sensor that can detect benzene-toluene-ethylbenzene-xylenes (BTEX) and chlorinated solvents is not currently available. A practical chlorinated solvent–BTEX sensor needs to detect contaminant concentrations in the parts per million (ppm)/parts per billion (ppb) range. Since these materials either do not fluoresce or fluoresce at wavelengths incompatible with the fiber optics, LIF cannot be used. Although these materials exhibit a characteristic Raman emission, Raman spectroscopy is a very sensitive technique. Therefore, another approach needs to be used to detect these materials. Electrochemical techniques can often detect materials in the ppm–ppb range, and the use of ultramicroelectrodes (UMEs) as sensors and detectors in gas-phase chromatography and in high-performance liquid chromatography has been described. We began to investigate the possibility of using UMEs as cone penetrometer sensors to detect BTEX, chlorinated solvents, and other volatile organic compounds (VOCs).

UMEs have diameters less than 50 μm. Because of their small size, fast response time, and diminished Ohmic losses, UMEs are being used to monitor electrochemical reactions *in vivo* in cells and tissues, in liquids of low conductivity, in the gas phase, and in solids. UMEs can be made from any electrode material (Au, Pt, C, etc.) in any geometrical arrangement (discs, rings, plates, etc.), and they can be assembled into arrays. We have prepared disk and ring UME arrays out of Au, Pt, Pd, Ag, Ni, and C. These UME arrays have been used to obtain voltammetric curves, between 0 and 8 V vs. the auxiliary electrode, for the compounds of interest in the gas and liquid phases. Figure 1 shows the voltammetric response of acetonitrile as it evaporates into the gas phase. The effects of temperature and epoxy resin, used to pot the inner UME into the auxiliary electrode assembly, have also been characterized.

Although electrochemical detection is very sensitive, the difficulty arises in identifying the species giving rise to the electrochemical response. We are in the process of evaluating three methods of species identification. One is to use the voltammetric response of the UME arrays to identify an unknown. While the peak current in a voltammorgram depends on the concentration of the species giving rise to the response thereby allowing quantification, the shape of the voltammetric curve depends on both thermodynamics and kinetics. As such, the adsorption of the electroactive species and the rates of charge transfer depend on the chemical nature of both the electroactive species and

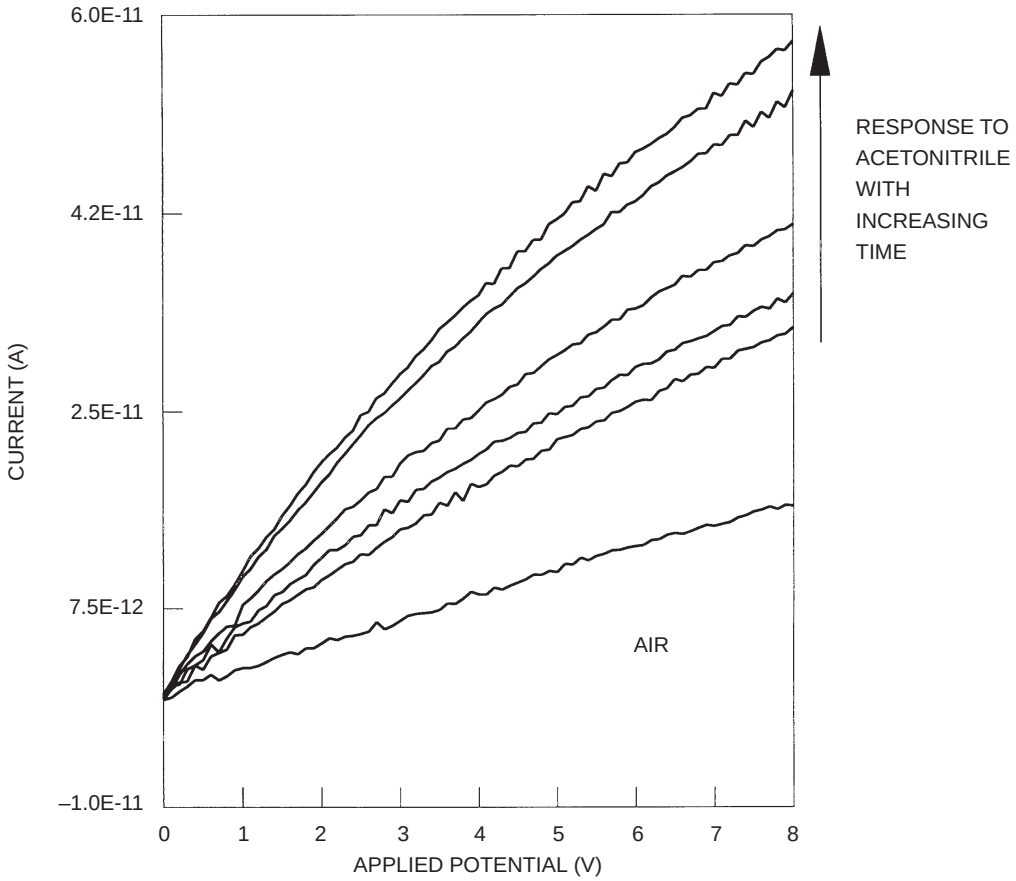

Figure 1. Voltammetric response of acetonitrile in the gas phase at room temperature. A 25-μl aliquot of acetonitrile was injected into a 5-ml glass flask. The evaporation of acetonitrile was monitored electrochemically using a UME array in which the inner working electrode was a 7-μm C disk, and the outer auxiliary electrode was an Au ring. Sweep rate was 100 mv s^{-1}.

the electrode substrate. We thought that if the voltammograms were sufficiently different, a neural network could be trained to differentiate species based on the shape of their voltammetric curves on different substrates. However, the voltammetric curves for the target compounds were not sufficiently different to allow for positive identification.

Another approach to species identification is to chemically modify the electrode substrate so that the UME will only respond to specific compounds. The compounds of interest (i.e., BTEX and chlorinated solvents) can act as either Lewis acids or bases. There are commercially available thiols, *RSH*, whose R groups exhibit Lewis acid-base chemistry. On Ag and Au metal surfaces, these thiols are known to self-assemble to form compact layers. The metal-thiolate bond anchors the organic functionality, *R*–, attached to the thiol group. We have purchased several thiols and are evaluating their selectivity and specificity for the compounds of interest using surface-enhanced Raman spectroscopy (SERS). Figure 2 shows the SERS response of 4-chlorothiophenol on a roughened Ag substrate as well as the response of benzene as it partitions into the coating.

Alternatively, UME arrays can be combined with a hot wire to create an amperometric gas sensor. As the gas, containing the contaminants, flows over the heated filament, ions are formed. The ions flow

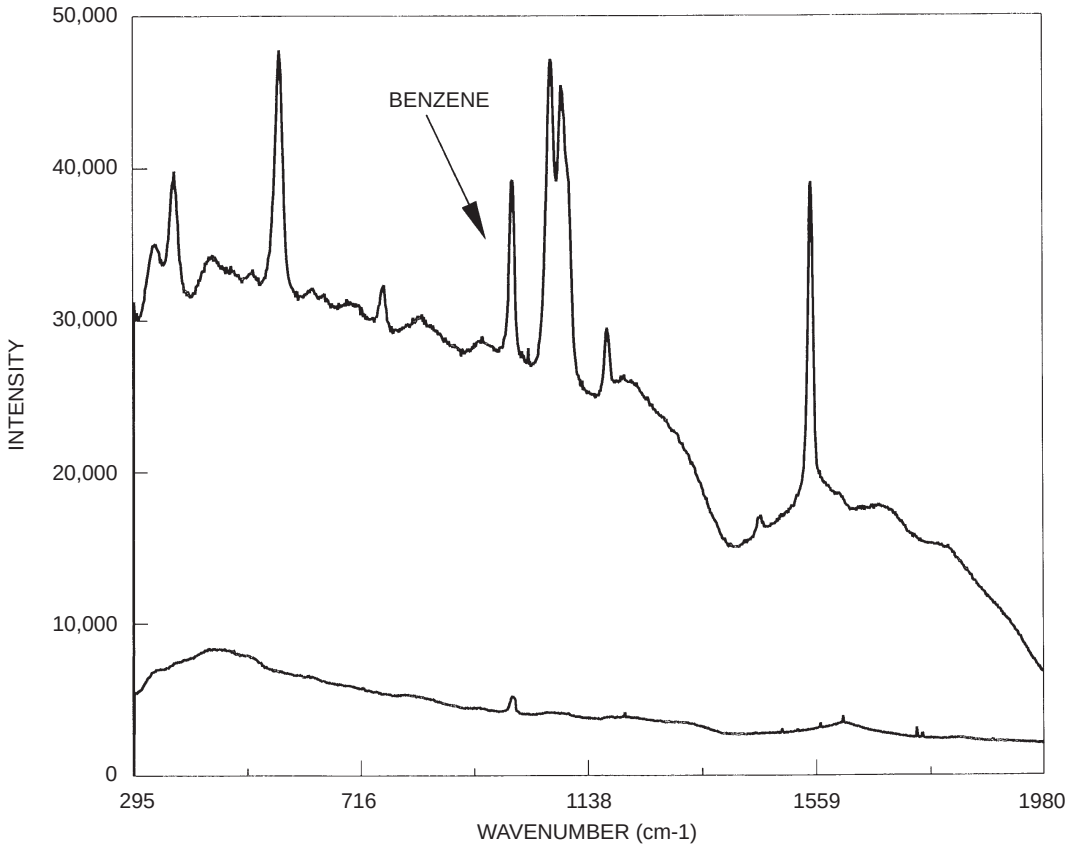

Figure 2. The bottom spectrum is of 661-ppm benzene in water. The top spectrum shows the SERS response of 4-chlorothiophenol on a roughened Ag substrate. The substrate is immersed in an aqueous 661-ppm benzene solution. The spectrum clearly shows the partitioning of benzene into the 4-chlorothiophenol coating.

to the sensor electrode of the electrochemical cell, which is set at a bias voltage relative to the reference electrode. The ions are then either oxidized or reduced or nothing happens. If oxidation/reduction occurs, current flows. By varying filament temperatures, UME materials, and bias voltages, a number of "channels" can be created. Each channel will display its own characteristic response to the ionized gas. Consequently, each organic contaminant will give rise to a specific pattern, thereby enabling species identification.

In summary, UME arrays have a number of applications. They can be used in a stationary sensor to monitor exposures to chemicals in a workplace, or they can be deployed in a "sniffer" probe and be used for real-time delineation of contaminants in a site. As such, there is great potential for dual use in the military and private sector.

PUBLICATIONS AND PRESENTATIONS

REFEREED JOURNALS, BOOKS/CHAPTERS, AND DISSERTATIONS (PUBLISHED/ACCEPTED)

Refereed Journals

Bulsara, A. M., M. E. Inchiosa, and L. Gammaitoni. 1996. "Noise-Controlled Resonance Behavior in Nonlinear Dynamic Systems with Broken Symmetry," *Physical Review Letters*, vol. 77, p. 2162.

Bulsara, A. M. and M. E. Inchiosa. 1996. "Array Enhanced Stochastic Resonance," *DoD Mission Success from High Performance Computing*, p. 1553.

Carter, B. R., D. W. Watson, R. F. Freund, E. Keith, F. Mirabile, and H. J. Siegel. 1997. "Dynamic Task Scheduling and Data Placement for Heterogeneous Computing Systems," *Information Sciences Journal*, Elsevier Publishing, (accepted to appear).

Goodman, I. R. and H. T. Nguyen. 1995. "Mathematical Foundations of Conditionals and Their Probabilistic Assignments," *International Journal of Uncertainty, Fuzziness and Knowledge-Based Systems*, vol.3, no. 3, pp. 247–339.

Inchiosa, M., A. Bulsara, and L. Gammaitoni. 1997. "Higher Order Resonant Behavior in Asymmetric Nonlinear Stochastic Systems," *Physical Review E*, (April, in press).

Johnson, R. A., C. E. Chang, P. M. Asbeck, M. E. Wood, G. A. Garcia, and I. Lagnado. 1996. "Comparison of Microwave Inductors Fabricated on Silicon-on-Sapphire and Bulk Silicon," *IEEE Microwave and Guided Wave Letters*, vol. 6, no. 9, p. 323.

Kundu, A. and G. C. Chen. 1997. "An Integrated Hybrid Neural Network and Hidden Markov Model Classifier for Sonar Signal Classification," to appear in *IEEE Transactions on Signal Processing*.

Mosier-Boss, P., R. Newbery, S. Szpak, S. H. Lieberman, J. W. Rovang. 1996. "Versatile, Low Volume, Thin Layer Cell for *In Situ* Spectroelectrochemistry," *Analytical Chemistry*, vol. 68, pp. 3277–3282.

Orazi, R. J. and M. N. McLandrich. 1994. "Bidirectional Transmission at 1.55 Microns Using Fused Fiber Narrow Channel Wavelength Division Multiplexors and Erbium-Doped Fiber Amplifiers," *IEEE Photonics Technology Letters*, vol. 6, no. 4, pp. 571–574.

Orazi, R. J., S. D. Russell, T. T. Vu, and P. K. L. Yu. 1997. "UV Fine Tuning of Narrow Channel Fused Fiber Wavelength Division Multiplexing Couplers," *IEEE Electronics Letters*, vol. 33, no. 2, pp. 154–155 .

Orazi, R. J., T. T. Vu, M. N. McLandrich, C. A. Hewett, and P. M. Poirier. 1996. "Cascaded Narrow Channel Fused Fiber Wavelength Division Multiplexors," *Electronics Letters*, vol. 32, no. 4, pp. 368–370.

Reuter, M. 1997. "Numerically Efficient Fourier-Based Technique of Calculating Error Probabilities for Intersymbol Interference," to appear in *IEEE Transactions on Communications*.

Scheps, R. 1996. "Upconversion Laser Processes," *Progress in Quantum Electronics*, vol. 20, pp. 271–358.

Winton, M. J., S. D. Russell, J. A. Wolk, and R. Gronsky. 1996. “Processing Independent Photoluminescence Response of Chemically Etched Porous Silicon,” *Applied Physics Letters*, vol. 69, no. 26, pp. 4026–4028.

Books/Chapters

Chadwick, D. B., J. L. Largier, and R. T. Cheng. 1996. “The Role of Thermal Stratification in Tidal Exchange at the Mouth of San Diego Bay,” *Buoyancy Effects on Coastal Dynamics*, D. G. Aubrey, ed., American Geophysical Union, Washington, DC, part III, chap. 12, pp. 155–174.

Goodman, I. R. 1997. “A New Approach to Conditional Fuzzy Sets,” *Advances in Machine Intelligence and Soft Computing*, P. P. Wang, ed., Duke University, Durham, NC, vol. IV, pp. 121–131.

Goodman, I. R. and G. F. Kramer. 1997. “Extension of Relational and Conditional Event Algebra to Random Sets with Applications to Data Fusion,” to appear in *Institute for Mathematics and Its Applications (IMA) Series*, Springer–Verlag, Berlin.

Largier, J. L., C. J. Hearn, and D. B. Chadwick. 1996. “Density Structures in Low Inflow Estuaries,” *Buoyancy Effects on Coastal Dynamics*, D. G. Aubrey, ed., part IV, chap 16, pp. 227–242.

McDonnell, J. R. 1997. “Control,” *Handbook on Evolutionary Computation*, Oxford University Press, (in press).

REFEREED JOURNALS, BOOKS/CHAPTERS, AND DISSERTATIONS (SUBMITTED)

Refereed Journals

Chadwick, D. B. and J. L. Largier. “Tidal Exchange at the Bay–Ocean Boundary, submitted to the *Journal of Geophysical Research*.

Edelblute, D. J. “Complex Cumulants and Spectral Analysis,” submitted to *IEEE Signal Processing Letters*.

Johnson, R. A., P. R. de la Houssaye, M. E. Wood, G. A. Garcia, C. E. Chang, P. M. Asbeck, and I. Lagnado. “A Silicon-on-Sapphire MOSFET Transmit/Receive Switch for L and S Band Transceiver Applications,” submitted to *IEEE Microwave and Guided Wave Letters*.

McGuiness, W. C., T. E. Jones, C. T. Blue, and J. S. Briggs. “Effects of Low Oxygen Pressure and Reflected Sputter Gas Bombardment on YBa2Cu307 Thin Films Deposited by Ion Beam Sputtering,” submitted to *Physica C*.

Rees, D. “An Adaptive Visoelastic Parabolic Equation Propagation Method,” submitted to the *Journal of the Acoustic Society of America*.

Reuter, M. and J. Zeidler. “Non-Linear Effects in LMS Adaptive Equalizers,” submitted to *IEEE Transactions on Signal Processing*.

Schwartz, D. F. “H^{oo} Approximation with Point Constraints Applied to Impedance Estimation,” submitted to *Circuits, Systems, and Signal Processing.*

Stein, D. W. J. “Computing K-Clutter-Plus-Gauss Distributions,” submitted to *Society on Industrial and Applied Mathematics (SIAM) Journal on Applied Mathematics.*

Stein, D. W. J. “Robust Implementations of an Exponential Mixture Detector with Applications to Radar,” *IEEE Proceedings on Radar, Sonar, and Navigation.*

NRaD PUBLICATIONS

Abusalem, H. A. and C. J. Warner. 1996. “Parameter Optimization for Asynchronous Transfer Mode Leaky Bucket Policing Algorithm,” NRaD TR 1732 (Dec). Naval Command, Control and Ocean Surveillance Center RDT&E Division, San Diego, CA.

Curtis, S. L., D. B. Chadwick, C. N. Katz, J. Rohr, M. Caballero, A. Valkins, and A. Patterson. 1996. “Environmental Analysis of U.S. Navy Shipboard Solid Waste Disharges,” NRaD TR 1716 (Feb). Naval Command, Control and Ocean Surveillance Center RDT&E Division, San Diego, CA.

Nguyen, H. G. 1996. “Obtaining Range from Visual Motion Using Local Image Derivatives,” NRaD TD 2918 (July). Naval Command, Control and Ocean Surveillance Center RDT&E Division, San Diego, CA.

Vu, T., C. A. Hewett, M. N. McLandrich, and R. J. Orazi. 1996. “Manufacturing Science and Technology for Polarization Independent Narrow Channel (PINC) Wavelength Division Multiplexing (WDM) Fiber Couplers,” NRaD TR 1724 (Sep). Naval Command, Control and Ocean Surveillance Center RDT&E Division, San Diego, CA.

PRESENTATIONS TO PROFESSIONAL MEETINGS

Invited Papers and Lectures

Bendall, C., T. Bull, and J. Caulfield. 1997. "Correlation Between Intensity Fluctuations in the Mid and Long IR Bands for Near Sea Transmission Paths," Infrared Search and Track (IRST) Systems and Related Issues Conference, 21 to 25 April, Orlando, FL.

Chadwick, D. B. 1996. "Mixing and Exchange Processes in San Diego Bay," Coastal Oceanography Seminar, (June), Scripps Institution of Oceanography, San Diego, CA.

Chadwick, D. B. 1996. "Tidal Exchange at the Mouth of San Diego Bay," Coastal Oceanography Seminar, (June), Scripps Institution of Oceanography, San Diego, CA.

Chadwick, D. B., C. N. Katz, and J. L. Largier. 1995. "Contaminant Transport Measurements in San Diego Bay," *Proceedings of Oceans '95,* San Diego, CA, vol. 3, pp. 1691–1699.

Freund, R. F., T. Kidd, and D. Hensgen. 1996. "SmartNet: A Scheduling Framework for Heterogeneous Computing," IEEE International Symposium on Parallel Architectures, Algorithms, and Networks (ISPAN) Conference, 12 to 14 June, Beijing, China.

Goodman, I. R. and G. F. Kramer. 1997. "Extension of Relational and Conditional Event Algebra to Random Sets with Applications to Data Fusion," to appear in the *Proceedings of the Workshop on Applications and Theory of Random Sets*, 22 to 24 August 1996, Institute for Mathematics and Its Applications, University of Minnesota at Minneapolis, MN.

Hibbs, A., E. Jacobs, A. Bulsara, J. Bekkedahl, and F. Moss. 1996. "Signal Enhancement in an RF SQUID Using Stochastic Resonance," Proceedings: *Fluctuations in Physics and Biology: Stochastic Resonance, Signal Processing and Related Phenomena,* 5 to 10 June 1994, Elba, Italy, pp. 811–817.

Lowen, S. and A. Bulsara. 1996. "Modulated Wiener Process, " Proceedings: *Fluctuations in Physics and Biology: Stochastic Resonance, Signal Processing and Related Phenomena,* 5 to 10 June 1994, Elba, Italy, pp. 847–854.

Scheps, R. 1996. "Upconversion Laser Pump Processes in Er^{3}+:$YA1O_{3}$," Society of Photo-Optical Instrumentation Engineers (SPIE) Proceedings, *Solid-State Lasers V,* 29 to 30 January, San Jose, CA, vol. 2698, pp.124–135.

Stein, D. W. J. 1996. "Detection of Random and Sinusoidal Signals in Hidden Markov Noise," *Proceedings of the 30th Annual IEEE Asilomar Conference on Signals, Systems, and Computers*, 3 to 6 November, Pacific Grove, CA.

Watkins, B. E., R. North, and M. Tummala. 1995. "Neural Network Based Adaptive Predistortion for the Linearization of Nonlinear RF Amplifiers," *Proceedings of IEEE MILCOM-95*, 5 to 8 November, San Diego, CA, pp. 145–149.

Watkins, B. E., R. North, and M. Tummala. 1996. "Predistortion of Nonlinear Amplifiers Using Neural Networks," *Proceedings of IEEE MILCOM-96,* 21 to 24 October, McLean, VA, pp. 316–320.

Contributed Papers and Lectures

Ambrosius, S. L., J. K. Byram, M. Campbell, R. F. Freund, T. Kidd, D. Klich, G. Dramer, M. Weissman, and R. Wellington. 1996. "Dynamic Segment Scheduling in JMCIS," *Proceedings of the 1996 Command and Control Research and Technology Symposium,* Monterey, CA, (June), pp. 669–685.

Bamber, D. 1995. "A Nonmonotonic Logic of Imperfect Generalizations," *Proceedings of the International Joint Conference on Artificial Intelligence*, Montreal, Canada.

Bamber, D. 1996. "A Doubly Probabilistic Approach to Nonmonotonic Reasoning," presented to the Logic Workshop, University of California at Irvine, 29 May, Irvine, CA.

Bamber, D. 1996. "A Doubly Probabilistic Approach to a Nonmonotonic Logic of Generalizations," presented to the Sixth International Workshop on Nonmonotonic Reasoning, 10 to 12 June, Timberline, OR.

Bamber, D. 1996. "Entailment in Probability of Thresholded Generalizations," *Proceedings of the Twelfth Conference on Uncertainty in Artificial Intelligence*, 1 to 4 August, Portland, OR, pp. 57–64.

Baxley, P. A. 1996. "The Effect of Three-Dimensional Bathymetry on Array Processor Performance," 132nd Meeting of the Acoustical Society of America, 2 to 6 December, Honolulu, HI.

Bendall, C. 1995. "Near Sea-Surface Infra-Red Transmission Experiments," *Proceedings of the SPIE International Symposium on Infrared Technology XXI,* 7 to 14 July, San Diego, CA., vol. 2552, pp. 181–191.

Bucker, H. 1996. "Active Matched-Field Tracking (AMFT)," *Proceedings of the 8th International Workshop on Matched-Field Processing and Model-Based Signal Processing,* 12 to 14 June, Victoria, Canada, pp. 29–30.

Bucker, H. and P. Baxley. 1996. "Active Matched-Field Tracking," 131st Meeting of the Acoustical Society of America, 13 to 17 May, Indianapolis, IN.

Chadwick, D. B., J. L. Largier, and R. George. 1996. "Tidal Exchange at the Bay–Ocean Boundary," *Proceedings of ERF (Estuarine Research Federation) '96*, 12 to 16 November, Corpus Christi, TX.

Fast, S. F. and F. J. Ryan. 1996. "A Numerical Comparison of Wedge Diffraction and Parabolic Equation Methods," *Proceedings of the IEEE Antennas and Propagation Society (APS) International Symposium and Union Radio-Scientifique Internationale (URSI) Radio Science Meeting*, 21 to 26 July, Baltimore, MD, vol. 1, pp. 490–493.

Freund, R. F., B. R. Carter, D. W. Watson, E. Keith, and F. Mirabile. 1996. "Generational Scheduling for Heterogeneous Computing," *Proceedings of the 1996 International Conference on Parallel and Distributed Processing Techniques and Applications*, (PDPTA '96), 9 to 11 August, Sunnyvale, CA, pp. 769–778.

Goodman, I. R. 1996. "Similarity Measures of Events, Relational Event Algebra, and Extensions to Fuzzy Logic," *Proceedings of the 1996 Biennial Conference of NAFIPS (North American Fuzzy Information Processing Society)*, 19 to 22 July, University of California at Berkeley, pp. 187–191.

Goodman, I. R. and G. F. Kramer. 1996. “Applications of Relational Event Algebra to the Development of a Decision Aid in Command and Control,” *Proceedings of the 1996 Command and Control Research and Technology Symposium*, 25 to 28 June, Naval Postgraduate School, Monterey, CA., pp. 415–435.

Goodman, I. R. and G. F. Kramer. 1997. “Extension of Relational Event Algebra to a General Decision Making Setting,” *Proceedings of the Conference on Intelligent Systems: A Semiotic Perspective*, 20 to 23 October, National Institute of Standards and Technology (NIST), Gaithersberg, MD, pp. 103–108.

Johnson, R. A., P. F. Chen, C. E. Chang, P. M. Asbeck, P. R. de la Houssaye, M. E. Wood, G. A. Garcia, I. Lagnado, and B. Xavier. 1997. “Silicon-on-Sapphire Technology for 2.4-GHz Applications,” Research Review and Industrial Advisory Board for the National Science Foundation (NSF) Industry/University Cooperative Research Center on Ultra-High-Speed Integrated Circuits and Systems (ICAS), 30 to 31 January, University of California at San Diego, La Jolla, CA.

Orazi, R. J. 1996. “Fused Fiber Devices for Wavelength Division Multiplexing Fiber Optic Systems,” Electrical and Computer Engineering Department Graduate Seminar, University of California at San Diego, 18 October, San Diego, CA.

Orazi, R. J., M. N. McLandrich, T. T. Vu, P. M. Poirier, and C. A. Hewett. 1996. “Polarization Independent Narrow Channel Wavelength Division Multiplexing Fiber Coupler Technology,” *Proceedings of the DoD Photonics Conference ’96*, 26 to 28 March, McLean, VA, pp. 243–247.

Reuter, M. 1997. “Non-Weiner Effects in LMS-Implemented Adaptive Equalizers,” 1997 International Conference on Acoustics, Speech, and Signal Processing (ICASSP-97), 20 to 24 April, Munich, Germany.

Scheps, R. 1996. “The Importance of Laser Beam Quality Measurements for Medicinal Treatment,” *Lasers in Surgery and Medicine*, Annual Conference of the American Society for Lasers in Medicine and Surgery (ASLMS*)*, 15 to 17 April, Orlando, FL, supplement 8, p. 4.

Scheps, R. 1997. “Considerations for Long-Pulse Solid-State Dye Laser Operation,” *Proceedings of the Society of Photo-Optical Instrumentation Engineers (SPIE)*, SPIE Conference, Solid-State Lasers VI, 8 to 14 February, San Jose, CA.

Shroff, P., D. Watson, N. Flann, and R. Freund. 1996. “Scheduling Data-Dependent Tasks in Heterogeneous Environments: A Genetic Simulating Annealing Approach,” *Proceedings of the 5th Heterogeneous Computing Workshop*, 15 to 16 April, Honolulu, HI, pp. 98–104.

Shum, A. 1996. “Routing ATM Networks,” presented at the Office of Naval Research Communications and Networking Workshop, 12 September, Naval Command, Control and Ocean Surveillance Center RDT&E Division, San Diego, CA.

Siegel, H. J., J. K. Antonio, M. Tan, R. C. Metzger, R. F. Freund, and Y. A. Li. 1995. “Heterogeneous Computing: One Approach to Sustained Petaflops Performance,” The Petaflops Frontier (TPF) Workshop, 6 February, McLean, VA.

Tummala M., M. Donovan, B. E. Watkins, and R. North. 1997. “Volterra Series Based Modeling and Compensation of Nonlinearities in High Power Amplifiers,” 1997 International Conference on Acoustics, Speech, and Signal Processing (ICASSP–97), 20 to 24 April, Munich, Germany.

Watkins, B. E., R. North, and M. Tummala. 1996. “Model-Based Neural-Network Predistortion of Nonlinear Amplifiers,” *Proceedings of the 1996 World Congress on Neural Networks*, 15 to 20 September, San Diego, CA.

PATENT ACTIVITY

INDEPENDENT RESEARCH
Patents Issued

Aram K. Kevorkian — **"Method and Apparatus for Pre-Processing Inputs to Parallel Architecture Computers"**

This invention provides an advanced computer user an automated means to find hidden pralellism in a wide range of problems of interest to both government and industry. With hidden parallelism exposed, the computer is able to partition the original problem into a suite of independently solvable smaller tasks that are then executed in parallel on different processors.

Patent 5,446,908 Navy case 74,063 (Serial 07/964,594) filed 21 October 1992, issued 29 August 1995.

Monti E. Aklufi — **"Chemical Sputter Deposition of Dielectric Films with Microwave Induced Plasmas"**

Chemical vapor deposition is caused through "chemical" sputtering of an inner chamber. The inner chamber serves as a source material that reacts with a process plasma to form volatile compounds, which, in turn, form desired film composition. The inner chamber may be made of a variety of materials depending upon what "source" material one desires the chamber to provide.

Patent 5,510,088 Navy case 72,776 (Serial 07/897,173) filed 11 June 1992; issued 23 April 1996.

Richard Scheps
Joseph F. Myers — **"Laser With Multiple Gain Elements of Different Materials"**

Two or more separate "arms" of a laser resonator contain gain elements that are end-pumped. Each arm operates at a different wavelength. Each gain element can be made of a different material. The two or more wavelengths are combined in another part of the cavity into a single multiwavelength beam by using a prism. A second waist is established in the cavity for nonlinear processes.

Patent 5,528,612 Navy case 75,129 (Serial 08/155,034) filed 19 November 1993; issued 18 June 1996.

Richard Scheps — **"A Low-Threshold Diode-Pumped Tunable Dye Laser"**

A method and apparatus for producing stimulated emission from a laser gain element containing an organic dye are described in which optical pumping is produced by visible laser diodes. Dye lasers are important for Navy countermeasures, but the pump sources used in the past to operate dye lasers are highly inefficient. This invention leads to a lightweight, compact solid-state pumped dye laser. This device is fieldable and can operate on flashlight batteries.

Patent 5,530,711 Navy case 75,686 (Serial 08/299,865) filed 1 September 1994; issued 25 June 1996.

Richard Scheps
Joseph F. Myers

"Laser with Multiple Gain Elements Pumped by a Single Excitation Source"

A laser produces laser emission at two or more wavelengths simultaneously. The laser includes at least two gain elements, and each gain element generates a different wavelength. A single optical pumping source is used for optically exciting all laser gain elements contained within the laser resonant cavity. A wavelength dispersing element such as a prism is disposed in the laser resonator cavity for dispersing the wavelengths operating simultaneously within the laser resonator cavity and to create separate regions for each laser gain element. Laser gain elements may be tunable laser gain elements or discretely emitting laser gain elements. Arbitrarily large wavelength separations between the wavelengths operating simultaneously may be achieved in this manner to produce stable cw or pulsed output, which may be Q-switched or line-narrowed. Intracavity sum-frequency generation can be produced efficiently by using a nonlinear sum-frequency-generating crystal disposed at a laser resonator cavity waist. The multiple gain elements may be of different materials or the same material.

Patent 5,541,946 Navy case 76,226 (Serial 08/339,993) filed 31 October 1994; issued 30 July 1996.

David J. Edelblute

"Method and Apparatus for Spectrum Analysis by Complex Cumulants"

A method for spectrum analysis by complex cumulants comprises the steps of receiving a signal, Fourier transforming the signal to form a series of complex Fourier coefficients, forming complex cumulants from the series of complex Fourier coefficients, and displaying the cumulants in a form wherein the non-Gaussian components of the signal are emphasized.

Patent 5, 602,751 Navy case 76,508 (Serial 08/395,549) filed 28 February 1995; issued 11 February 1997.

INDEPENDENT RESEARCH
Patent Applications Filed

Stanislaw J. Szpak
Pamela A. Boss

"Electrode and Method for Preparation of Electrode for Electrochemical Compression of Deuterium into a Metal Lattice"

This invention provides an electrode and method for preparing the electrode that may be employed to electrochemically compress deuterium into a metal lattice of the electrode. An electrochemical cell is constructed that includes an electrolyte solution comprising a metallic salt and a supporting electrolyte. The metallic salt, when in a reduced state, absorbs deuterium. Both the electrolytic solution and supporting electrolyte are dissolved in heavy water. An anode and cathode are immersed and stable within the electrolytic solution. The anode is stable when polarized. A voltage is applied across the anode and cathode while a constant potential is maintained at the cathode. The constant potential is measured with respect to a reference electrode immersed within the electrolytic solution so that deposition of metallic ions occur in the presence of evolving deuterium during electrolysis of the electrolytic solution. By this method, the cathode is transformed into the electrode.

Navy case 73,311 (Serial 07/632,896) filed 24 December 1990; pending.

Wadad B. Dubbelday
Randy L. Shimabukuro
Stephen D. Russell

"Electroluminescent Devices in Porous Silicon on Sapphire"

This invention describes an electroluminescent shottky or pn diode device on silicon on sapphire and a method of manufacturing this device.

Navy case 75,291 (Serial 08/614,783) filed 8 March 1996; pending.

Michael R. Brininstool
David M. Bullat
Po-Yun Tang

"Fiber-Optic Self-Multiplexing Amplified Ring Transducer and Force Transfer Sensor with Pressure Compensation"

This invention provides a system of multiplexed array of fiber-optic sensors with force transfer transducers for detecting the presence of an environmental field condition, such as underwater acoustic pressure perturbations. The invention can be deployed in a single multiplexed array system with incoherent light and at various depths or altitudes with a hydrostatic-pressure equalizer enabling the isolation of dynamic external perturbations from other pressure variations.

Navy case 75,649 (Serial 08/434,366) filed 2 May 1995; pending.

Richard Scheps **"Er:YALO Upconversion Laser"**

A novel technique for upconversion pumping is described that uses intracavity absorption to get 100-percent conversion efficiency.

Navy case 76,005 (Serial 08/565,075) filed 30 November 1995; pending.

Paul G. Kennedy **"Fiber-Optic Cable Junction"**
Willard Stevenson

A fiber-optic cable junction for joining the ends of two fiber-optic cables comprises the steps of inserting a tube fastener over each cable end and inserting a protective sleeve and a splint fastener over either cable end. The cable ends are then spliced together. The protective sleeve is positioned over the splice and is supported by fastening an inner splint rod to the cable buffer with the tube fasteners. The cable buffer is supported by an outer split rod fastened to the tube fasteners by the splint fastener.

Navy case 76,880 (Serial 08/579,711) filed 28 December 1995; pending.

Stephen D. Russell **"Silicon Nanostructures in**
Robert C. Dynes **Silicon on Insulator"**
Paul R. de la Houssaye
Wadad B. Dubbelday
Andrew Katz
Randy L. Shimabukuro

This invention discloses a variety of electrical, optical, mechanical, and quantum-effect devices on an insulating substrate and their method of fabrication for advanced electronic, optoelectronic, optical computing, and flat-panel display applications.

Navy case 76,969 (Serial 08/528,386) filed 13 September 1995; pending.

Richard J. Orazi **"Method for Tuning Fiber-Optic Couplers and Multiplexers"**

This patent application describes a way of tuning the wavelength response of fused and tapered optical-fiber couplers by exposing the fused region to high-intensity ultraviolet light, which permanently changes the index of refraction in the fused region and so alters the wavelength response of the device.

Navy case 77,012 (Serial 08/538,432) filed 9 August 1995; pending.

Richard Scheps **"Laser Diode Wavelength and and Beam Homogenizer"**

A laser-diode power combiner comprises a dye laser operably coupled to an array of laser diodes for combining optical power from the laser diodes into a single, coherent laser beam.

Navy case 77,221 (Serial 08/572,828) filed 14 December 1995; pending.

Allen Shum **"Asynchronous Transfer Mode Cell Loss Estimation Algorithms"**

A software program for estimating traffic loss of an asynchronous transfer mode (ATM) statistical multiplexer comprises a communication channel having traffic sources and a buffer. Traffic is generated by the traffic sources and removed by the communication channel. When total traffic exceeds the capacity of the communication channel, excess traffic is stored in the buffer. When the buffer is full, excess traffic is lost. Estimating the amount of traffic that will be lost by an ATM statistical multiplexer therefore has application in the design of ATM networks.

Navy case 77,443 (Serial 08/707,284) filed 3 September 1996; pending.

David W. J. Stein **"A Method for Detecting Signals in Non-Gaussian Background Clutter"**

This device detects (using only amplitude data) signals in nonstationary, non-Gaussian noise that may be modeled by using exponential mixture distributions.

Navy case 77,579 (Serial 08/742,413) filed 24 October 1996; pending.

Howard L. Dyckman **"Spread Spectrum Modulation Using Time-Varying Linear Filtering"**

This method for transmitting information by radio over a wide bandwidth comprises the following steps: inputting a data signal into a time-varying filter modulator; spreading the data signal in time and in frequency to produce a wide-band signal; modulating the sideband signal onto an RF carrier to provide an RF output signal; and transmitting the RF output signal. This step of spreading includes performing a series of linear transformations to the data signal.

Navy case 77,685 (Serial 08/621,400) filed 25 March 1996; pending.

INDEPENDENT RESEARCH
Invention Disclosures Authorized

Eric J. Lind
Gary F. Mastny

"Microminiature High-Voltage Power-Pack Module"

A high-voltage array of p–n junctions is coupled to a high-voltage array of stacked rechargeable Li storage cells. Periodic illumination of the array via fiber-optic cable results in a microminiature low-noise source of high-voltage bias for sensing elements such as used in radiation-monitoring equipment.

Navy case 76,070; authorized for preparation of patent application 7 August 1995.

Steven D. Russell
Shannon Kasa
Howard W. Walker

"Chemical Sensor Using Ring Oscillator Thermometry"

This invention describes a novel structure using ring oscillator thermometry for use as a chemical or biological sensor. Combustible gas sensors based on thermal sensors have been demonstrated in the prior art. These sensors, called pellistors, depend on a rise in temperature at a catalytic surface due to catalytic oxidation of the combustible gas. The pellistor measures this rise in temperature with a thermistor. The novel gas sensor incorporates a catalytic platinum layer deposited on top of a ring oscillator. Combustible gases will be catalytically oxidized at the platinum surface. The heat released by the reaction will cause local heating of the RO, and thus affect its frequency.

Navy case 76,462; authorized for preparation of patent application 11 July 1995.

Stephen M. Hart

"Optoelectronically Controlled Frequency Selective Surface"

A photovoltaic field-effect transistor (PVFET) is used to control the impedance, scattering frequency, and scattering cross-section of the scattering elements on a Frequency Selective Surface. The PVFETs are implanted in the arms of either wire or slot scatterers in order to make their scattering properties adjustable. The resulting OCFSS becomes a programmable electromagnetic shield or pattern control device.

Navy case 76,915; authorized for preparation of patent application 26 March 1996.

Stephen M. Hart **"Optoelectronically Controlled Waveguide"**

An Optoelectronically Controlled Waveguide (OCW) is composed of a metallic waveguide, a finline, and a PVFET. The finline is inserted into the waveguide making electrical contact, and the PVFET is affixed to the finline in a shunt configuration. The resulting device is capable of attenuating the energy propagating in the waveguide to any desired degree. In this fashion, the OCW can function as an attenuator or a switch. A PVFET is a field-effect transistor with a gate controlled by a photovoltaic cell.

Navy case 76,916; authorized for preparation of patent application 26 March 1996.

Stephen D. Russell **"Energy-Converting Porous Silicon Optical Element"**

This invention describes an optical element made of porous silicon on a transparent substrate for converting light of an incident energy to that of a lower emitted energy. This invention may be used for the efficient detection of normally invisible and undetectable wavelengths.

Navy case 76,947; authorized for preparation of patent application 28 May 1996.

David Stein **"A Method for Detecting Signals in Non-Gaussian Background Clutter"**

A method for detecting weak targets in nonstationary non-Gaussian radar clutter by using the intensity of the radar returns.

Navy case 77,579; authorized for preparation of patent application 26 August 1996.

INDEPENDENT RESEARCH
Invention Disclosures Submitted

Willard M. Cronyn **"Compact, Phasable, Multioctave, Planar, High-Efficiency Spiral-Mode Antenna"**

The antenna consists of eight planar windings, each one of which is an exponential spiral. The windings are connected in groups of three to a balanced transmission line, with a "floating" winding between each of the two groups. For the purpose of phasing elements together for directional beam control, the particular grouping of windings can be changed. A sinuous variation is imposed on the spiral windings to increase the path length for each winding rotation so that the circumference through which the phase increases by 360 degrees is correspondingly decreased. This element integrates a planar structure, wide-band compact design, and phasability into a single physical structure.

Navy case 76,188; disclosure submitted 15 February 1994.

Richard Scheps — **"Underwater Imaging Technique for the Detection of Shallow Submerged Objects"**

This high-resolution underwater imaging and ranging device scans an area underwater with a pulsed laser and records the reflected signal from the illuminated area with a gated photomultipler.

Navy case 77,222; disclosure submitted 16 June 1995.

Michael J. Winton
Stephen D. Russell — **"Method of Making Improved Electrical Contact to Porous Silicon"**

This is an improved method of making electrical contact to porous silicon and porous silicon device structures by controlling the global or large-scale surface morphology. The inventive process uses the supply of holes, ions of other charged species to control the etching dynamics of the porous silicon formation. The intensity of the light emitted by porous silicon layers and devices can therefore be increased by the improved electrical interconnection between the mechanically, chemically, and thermally fragile porous silicon and the device electrodes.

Navy case 77,603; disclosure submitted 2 January 1996.

Thomas W. Schlosser — **"A Spherical Coordinate Algorithm for the Detection of Collisions between Three-Dimensional Objects in Computer Models"**

This invention describes an algorithm for collision detection between three-dimensional objects in computer models that is more efficient and simpler than current algorithms. Current collision-detection algorithms rely either on testing for polygon intersections or attempt to solve multiple simultaneous polynomial equations to test for collision between surface patches on a three-dimensional model. All algorithms rely on Cartesian representations of the objects. A method using spherical coordinates, based on the relatively simple test for collision between spheres, provides a more efficient means of testing for collisions and is simple to calculate and implement after multiple rotations of the model.

Navy case 77,771; disclosure submitted 18 April 1996.

Monti E. Aklufi
Stephen D. Russell — **"Thin-Film Improvement Method and Apparatus"**

This invention provides novel apparatus and improved method using a contoured laser beam to improve the electrical, optical, and materials properties of thin films.

Navy case 77,921; disclosure submitted 18 June 1996.

Adi R. Bulsara
Mario E. Inchiosa

"Detector of Weak Signals Based on Noise-Controlled Resonance Behavior in Nonlinear Dynamic Systems with Broken Symmetry"

This device exploits the dynamical symmetry-breaking property of a weak dc signal in an *a priori* symmetric nonlinear dynamic device, to detect and quantify the dc signal. Simultaneously, the technique offers a novel way to circumvent detector low-frequency noise constraints by shifting the detection to a more acceptable part of the frequency spectrum.

Navy case 78,154 disclosure submitted 1 July 1996.

Stephen D. Russell
Philip R. Kesten

"Interactive Display Device"

This invention is a monolithically integrated display and sensor array that provides for interactive real-time changes to the display image.

NCCOSC-255 (no Navy case number yet); disclosure submitted 24 October 1996.

INDEPENDENT EXPLORATORY DEVELOPMENT
Claims Allowed; Notice of Allowance/Allowability

Everett W. Jacobs
Roger D. Boss
Yuval Fisher

"Method of Encoding a Digital Image by Using Adaptive Partitioning in an Iterated Transformation System"

This invention is a new adaptive method for partitioning an image, resulting in efficient encoding by using the iterated transformation image-compression technique.

Navy case 74,198 (Serial 07/859,782) filed 30 March 1992; pending. Notice of Allowance 15 May 1996.

Stephen D. Russell
Wadad B. Dubbelday
Randy L. Shimabukuro
Paul de la Houssaye
Diane M. Szarflarski

"Photonic Silicon on a Transparent Substrate"

This invention describes light-emitting (photonic) silicon on a transparent substrate and its method of fabrication.

Navy case 75,292 (Serial 08/118,900) filed 9 September 1993; pending. Notice of Allowance 4 September 1996.

Michael R. Brininstool
David M. Bullat
Po-Yun Tang

"Force Transfer Column (Longitudinal to Radial) with High-Frequency Filter Isolator for Use in Fiber-Optic Sonar Transducers"

The purpose of this proposed concept is to facilitate the use of fiber-optic cables to measure in-water acoustic perturbations.

Navy case 75,649 (Serial 08/434,366) filed 2 May 1995; pending. Notice of Allowance 11 June 1996.

INDEPENDENT EXPLORATORY DEVELOPMENT
Patent Applications Filed

Wadad B. Dubbelday
Randy L. Shimabukuro
Stephen D. Russell

"Electroluminescent Devices in Porous Silicon on Sapphire"

An electroluminescent device is integrated on a sapphire substrate that is transparent to light generated by electroluminescence. Crystalline silicon is formed on the sapphire substrate and patterned into an island. A titanium-silicide electrode is formed in the silicon around the island by a titanium-silicide reaction and covered by an electrically insulating layer. The island is etched to expose the silicon, and a porous silicon layer is formed on the crystalline

silicon. An aluminum electrode is formed on the porous silicon layer. An outer insulating layer may be formed on the aluminum electrode and the titanium silicide electrode. Additional electrodes may be formed on and through the outer insulating layer to make electrical contact with the titanium silicide and aluminum electrodes, respectively. A voltage source may be connected to the electrodes to cause light to be emitted from the porous silicon through the sapphire substrate.

Navy case 75,291 (Serial 08/614,783) filed 8 March 1996; pending.

Neil P. Acantilado — **"Computer Program for a Three-Dimensional Bolumetric Display"**

This method for transforming world coordinates into device coordinates comprises the following steps: inputting a set of world coordinates to be displayed; scaling the world coordinates into view coordinates bounded by a display volume; finding a control memory location of a light-beam deflector corresponding to a Y-axis position for each of the view coordinates; calculating X-axis and Z-axis device coordinates from the view coordinates for deflecting a light beam to a selected point within the display volume, corresponding to each of the view coordinates; and loading the device coordinates into the control memory locations corresponding to the Y-axis position for each of the view coordinates, to cause the light beam to be deflected to each selected point.

Navy case 77,782 (Serial 08/726,305) filed 2 October 1996; pending.

INDEPENDENT EXPLORATORY DEVELOPMENT
Invention Disclosure Authorized

Pamela A. Boss
Roger D. Boss — **"Versatile, Thin Layer Cell for *In-Situ* Spectroelectrochemistry"**

The disclosure describes the design of a low volume, thin layer cell constructed of chemically resistant materials capable of performing spectroelectrochemistry. Such a cell can be used as a flow-through cell to continuously monitor manufacturing processes.

Navy case 77,803; authorized for preparation of patent application 15 January 1997.

INDEPENDENT EXPLORATORY DEVELOPMENT
Patent Application Abandoned

Terence R. Albert
Adi R. Bulsara
Gabor Schmera

"Nonlinear Dynamic Signal Processor, Based on Enhancement of Stochastic Resonance Effect in Coupled Oscillator Arrays"

Globally coupled nonlinear oscillators are subject to the weak deterministic signal of interest. The background noise enhances the signal-to-noise ratio at the output via the stochastic resonance effect. The enhancement is far greater than would be realized by a single oscillator.

Navy case 75,209 (Serial 08/249,111) filed 25 May 1994; abandoned 12 June 1996.


GLOSSARY

GLOSSARY

ADCP	acoustic Doppler current profiler
AG	algebraic-geometric (codes)
AMFT	active matched-field tracking
API	Application Programmer Interface
APS	Antennas and Propagation Society
ASA	Acoustical Society of America
ASC	American Society for Composites
ASCE	American Society of Civil Engineers
ASEE	American Society for Engineering Education
a-Si	amorphous silicon
ASLMS	American Society for Lasers in Medicine and Surgery
ASME	American Society of Mechanical Engineering
ASSP	Acoustics, Speech, and Signal Processing
ATD	Advanced Technology Demonstration
ATM	Asynchronous Transfer Mode
b–e	bending-extension
BER	bit-error-rate
BPSK	binary-phase-shift-keyed
BTEX	benzene-toluene-ethylbenzene-xylenes
C^3	command, control, and communications
C^4I	command, control, communications, computers, and intelligence
CEA	Conditional Event Algebra
CFAR	constant false alarm rate
CHIEF	Combined Helmholtz Integral Formulation
Chl–a	chlorophyll–a
CINCPACFLET	Commander in Chief, U.S. Pacific Fleet
CMOS	complementary metal-oxide semiconductor
CO_2	carbon dioxide
ColTstAPI	Collision Tester API
CRDA	Cooperative Research and Development Agreement
CT	critical technology (see DoD CT)
CTD	conductivity, temperature, and depth
cw	continuous wave
DARPA	Defense Advanced Research Projects Agency
dc	direct current
DF	deuterium fluoride
DGPS	differential-mode Global Positioning System
DigComT	Digital Communications Toolbox
DoD	Department of Defense

DoD CT Codes	Department of Defense Critical Technology
1	Aerospace Propulsion and Power
2	Air Vehicles
3	Space Vehicles
4	Chemical and Biological Defenses
5	Clothing, Textiles, and Food
6	Command, Control, and Communications
7	Computers
8	Conventional Weapons
9	Electronics
10	Electronic Warfare
11	Directed Energy Weapons
12	Environmental Quality
13	Civil Engineering
14	Battlespace Environments
15	Human–System Interfaces
16	Manpower, Personnel, and Training
17	Materials, Processes, and Structures
18	Biomedical
19	Sensors
20	Surface/Undersurface Vehicles
21	Ground Vehicles
22	Software
23	Manufacturing Science and Technology
24	Simulation and Modeling Technology

DoD MA	Department of Defense Mission Area
AAW	Anti-Air Warfare
AMW	Amphibious Warfare
ASU	Anti-Surface Ship Warfare
ASW	Anti-Submarine Warfare
CCC	Command, Control, and Communications
ELW	Electronic Warfare
FSO	Fleet Support Operations
INT	Intelligence
LOG	Logistics
MIW	Mine Warfare/Mine Countermeasures
MOB	Mobility
MWT	Multi-Warfare Technology
OSV	Ocean Surveillance
PMD	Personnel/Medical
SBS	Sea-Based Strategic Warfare
SPW	Special Warfare

STW	Strike Warfare
TNG	Training
DSP	digital signal processor
ECE	electrical and computer engineering
EM	electromagnetic
EM	expectation maximization
EOS	Earth Observing System
ERF	Estuarine Research Foundation
ESA	European Space Agency
EUTELSAT	European Telecommunications Satellite Organization
FET	field-effect transistor
FWM	focused wave mode
GaAs	gallium arsenide
GMPD	Gaussian mixture probability densities
GPS	Global Positioning System
HDR	high data rate
HLA	horizontal line array
HMM	hidden Markov models
HPA	high-power amplifiers
HPC	high-performance computing
ICAS	integrated circuits and systems
ICASSP	International Conference on Acoustics, Speech, and Signal Processing
ICCE	International Conference on Composite Engineering
IED	Independent Exploratory Development
IMA	Institute for Mathematics and Its Applications
IMAT	Interactive Multi-sensor Analysis Training
INTELSAT	International Telecommunications Satellite Organization
I/O	input/output
IR	independent research
IP3	intercept point, 3rd order
IRS&T	infrared search and track
ISPAN	International Symposium on Parallel Architectures, Algorithms, and Networks
JMA	Joint Mission Area
Codes	
1	Joint Strike
2	Joint Littoral Warfare
3	Joint Surveillance
4	Joint Space and Electronic Warfare/Intelligence
5	Strategic Deterrence

6	Strategic Sealift and Protection
7	Forward Presence
8	Readiness, Support, and Infrastructure
9	Manpower and Personnel

JSAC	Journal on Selected Areas in Communication
LIBS	laser-induced breakdown spectroscopy
LIF	laser-induced fluorometer
LMS	least-mean-square
LOBD	locally optimal Bayes detection
LOGAN	Low Grazing ANgle
LOS	line-of-sight
MA	Mission Area (see DoD MA)
MACE	Multistatic Active Capability Enhancement (Program)
MATES	Multispectral Anti-ship Cruise Missile Tactical Electronics Warfare System
MATURE	Matrix Approach To Understanding Relativistic Electrodynamics
MCT/InSb	mercury cadmium telluride/indium antimonide
MFT	matched-field tracking
MHHW	mean higher high water
MIT	Massachusetts Institute of Technology
MLLW	mean lower low water
MSE	mean-square-error
MshBilAPI	Mesh Builder API
NA-ASW	nonacoustic-antisubmarine
NAFIPS	North American Fuzzy Information Processing Society
NASA	National Aeronautics and Space Administration
NAVSEA	Naval Seas Systems Command
NCCOSC	Naval Command, Control and Ocean Surveillance Center
NDE	nondestructive evaluation
NEC	Numerical Electromagnetic Code
NetComAPI	Network Communication API
NIST	National Institute of Standards and Technology
NLMS	normalized LMS algorithm
NOSC	Naval Ocean Systems Center
NQE	Network Queing Environment
NQR	nuclear quadrapole resonance
NRaD	NCCOSC RDT&E Division
NRL	Naval Research Laboratory
NSF	National Science Foundation
NSWC	Naval Surface Warfare Center
NSWCDD	Naval Surface Warfare Center, Dahlgren Division
NUWC	Naval Undersea Warfare Center

OCW	optoelectronically controlled waveguide
ONR	Office of Naval Research
ONR SE	Office of Naval Research Subelement

Codes

11	General Physics
12	Radiation Sciences
13	Chemistry
14	Mathematics
15	Computer Science
21	Electronics
22	Materials
23	Mechanics
24	Energy Conversion
31	Ocean Sciences
32	Ocean Geophysics
33	Atmospheric Sciences
34	Astronomy and Astrophysics
35	Environmental Science
41	Biological and Medical Sciences
42	Cognitive and Neural Sciences
52	Multidisciplinary Support

OPNAV	Office of the Chief of Naval Operations
ORMOSILS	(glass-like substrates)
OSMD	order statistic mixture detector
PBC	polairzation beam combiner
PDPTA	parallel and distributed processing techniques and applications
PE	parabolic equation
PE	propagation environment
PFA	probability of false alarm
PINC	polarization-independent narrow-channel
PMMA	polymethyl methacrylate
ppb	parts per billion
ppm	parts per million
PSCEA	Probability Space Conditional Event Algebra
PSD	power spectral density
PV	photovoltaic
PVFET	photovoltaic field-effect transistor
PVM	Parallel Virtual Machine
PZT	lead zirconium titanate
QAM	Quadrature-Amplitude Modulation
QoS	quality of service
RDT&E	Research, Development, Test and Evaluation
REA	Relational Event Algebra

RF	radio frequency
RFMP	RF Mission Planner
ROC	receiver operating characteristics
RS	Reed–Solomon (codes)
SATCOM	satellite communications
SBIR	Small Business Innovation Research
SCADCo	Spherical Coordinate Algorithm for the Detection of Collisions
SDSU	San Diego State University
SE	subelement (see ONR SE)
SEI	Software Engineering Institute
SER	symbol error rate
SERS	surface enhanced Raman spectroscopy
SIAM	Society on Industrial and Applied Mathematics
SIMOX	Separation by Implantation of Oxygen
SIR	signal-to-interference ratio
SNR	signal-to-noise ratio
SOI	silicon on insulator
SOS	silicon on sapphire
SPIE	Society of Photo-Optical Instrumentation Engineers
SQUID	Superconducting Quantum Interference Device
SR	Stochastic Resonance
TEM	transverse electromagnetic
TDR	time domain reflectometry
TPAH	total polycyclic aromatic hydrocarbons
TPF	The Petaflops Frontier
T/R	transmit/receive
TTCP	The Technical Cooperation Panel
TWT	traveling wave tube
UCSD	University of California at San Diego
UME	ultramicroelectrode
URSI	Union Radio-Scientifique Internationale (International Union of Radio Science)
UV	ultraviolet
UVF	ultraviolet fluorescence
VLA	vertical line array
VOC	volatile organic compound
WDM	wavelength division multiplexer

	Form Approved OMB No. 0704-0188

1. AGENCY USE ONLY *(Leave blank)*	2. REPORT DATE	3. REPORT TYPE AND DATES COVERED
	October 1996	Final: October 1995 through September 1996

4. TITLE AND SUBTITLE	5. FUNDING NUMBERS
INDEPENDENT RESEARCH 1996 ANNUAL REPORT	In-house
6. AUTHOR(S)	

7. PERFORMING ORGANIZATION NAME(S) AND ADDRESS(ES)	8. PERFORMING ORGANIZATION REPORT NUMBER
Naval Command, Control and Ocean Surveillance Center (NCCOSC) RDT&E Division (NRaD) San Diego, CA 92152–5001	

9. SPONSORING/MONITORING AGENCY NAME(S) AND ADDRESS(ES)	10. SPONSORING/MONITORING AGENCY REPORT NUMBER
Office of Naval Research 800 North Quincy Street Arlington, VA 22217–5000	TD 2933

11. SUPPLEMENTARY NOTES

12a. DISTRIBUTION/AVAILABILITY STATEMENTR	12b. DISTRIBUTION CODE
Approved for public release; distribution is unlimited.	

13. ABSTRACT *(Maximum 200 words)*

This report presents brief summaries of the Independent Research (IR) projects. Three projects are described in detail: Optical Fiber Devices Based on Index of Refraction Changes in Highly Overcoupled Fused-Fiber Couplers; Tidal Exchange at the Bay–Ocean Boundary; and Detection Algorithms Derived from Gaussian Mixture and Hidden Markov Noise Models with Applications to Radar and Sonar.

14. SUBJECT TERMS AND MISSION AREAS			15. NUMBER OF PAGES
command and control surveillance	communications other leadership areas	independent research (IR)	206 16. PRICE CODE

17. SECURITY CLASSIFICATION OF REPORT	18. SECURITY CLASSIFICATION OF THIS PAGE	19. SECURITY CLASSIFICATION OF ABSTRACT	20. LIMITATION OF ABSTRACT
UNCLASSIFIED	UNCLASSIFIED	UNCLASSIFIED	SAME AS REPORT